WSI
Walter Schottky Institut

Technische Universität München

Ultrafast Nanowire Lasers as On-Chip Devices

Dissertation

Benedikt Florian Mayer

München, den 31.10.2016.

Lehrstuhl für experimentelle Halbleiterphysik E24
Walter Schottky Institut
Technische Universität München

Ultrafast Nanowire Lasers as On-Chip Devices

Benedikt Florian Mayer

Vollständiger Abdruck der von der Fakultät für Physik der Technischen Universität München zur Erlangung des akademischen Grades eines

Doktors der Naturwissenschaften

genehmigten Dissertation.

Vorsitzender: Prof. Dr. Frank Pollmann

Prüfer der Dissertation:
1. Prof. J. J. Finley, Ph.D.
2. Prof. Dr. Reinhard Kienberger
3. Prof. Dr. Peter Smowton (nur schriftliche Beurteilung)

Die Dissertation wurde am 14.11.2016 bei der Technischen Universität München eingereicht und durch die Fakultät für Physik am 22.05.2017 angenommen.

Abstract

Microchips that operate with light instead of electronics have become a vision that has been a key driver of semiconductor and nano research during the past years. The consequent drive to replace electronic components by photonic devices has reached a level where today's communication and computation speed limit, as well as their energy consumption appears antiqued. The data capacity of fiber technology has evolved even faster than the downscaling of microchips and provides huge potential especially for short haul and chip-level interconnects in the near future. In contrast, the increasingly problematic of heat dissipation in electronic microchips and rising costs per bit make it very difficult to enhance speed and computing power simply by following constant field scaling. However, the inefficiency of silicon light sources and the incompatibility of the majority of optically active gain materials for the far advanced silicon technology has hindered the integration of efficient light sources on microchips. Offering a solution to this challenge, semiconductor nanowires can be monolithically integrated directly on silicon whilst maintaining the exceptional optical properties of crystalline direct bandgap semiconductors. Furthermore, the optical cavity formed by the unique nanowire geometry, in combination with the nanowire gain material constitutes all the required components for a nano-scale laser. Integrated on silicon, such coherent on-chip light sources could represent a major step towards the realization of chip-level optical interconnects or even photonic computers that, in the next decade, might not only remain a vision.

However, the deleterious impact of non-radiative surface recombinations on the optical properties of III-V semiconductors has inhibited the demonstration of nanowire lasers that operate in the technologically important near infrared spectral range. Furthermore, in previous studies, nanowires typically had to be removed from their growth substrate to enable lasing, negating the huge technological advantage of monolithic integration and rendering their integration impractical. Besides their strong potential for future applications, nanowire lasers constitute a unique system that provide entirely new insights into fundamental gain dynamics at the ultimate downscaling limit of photonic lasers. Although, lasing operation of nanowires has been demonstrated from a broad range of material systems, coherent light-matter interactions within nanowire lasers have not received significant attraction.

This thesis demonstrates how GaAs based nanowires are carefully designed to achieve lasing operation in the near infrared spectral range. The presented results demonstrate the first observation of room temperature lasing from GaAs nanowire lasers subject to pulsed optical excitation. Experiments using continuous optical pumping demonstrate continuous wave operation and show spectral linewidths below 200μeV. Investigations of the gain and photon dynamics of the nanowire lasers reveal a novel mechanism that allows long-term mutual phase locking of picosecond pulse pairs and potential operation at modulation frequencies >200GHz. Finally, a novel nanowire laser geometry

that allows the monolithic integration of nanowire lasers onto silicon microchips is introduced, successfully demonstrated in experiments and has been submitted as patent application.
The exceptional properties of GaAs nanowire lasers combined with their unique ability for monolithic integration onto silicon provide nanowire lasers with the potential to impact a broad range of integrated optoelectronic technologies and could be a step along the road toward the vision of photonic microchips.

Abstract

Lichtbetriebe Microchips sind in den letzten Jahren zu eine Vision herangereift, die heute eine Schlüsselrolle für den Fortschritt der Halbleiter- und Nanoforschung darstellt. Der Antrieb elektronische Komponenten durch photonische Bauteile zu ersetzen hat bereits ein Niveau erreicht, bei dem heutige Geschwindigkeitsbeschränkungen für die Kommunikation und der Verarbeitung von Daten antiquiert erscheinen. Dabei hat sich die Leistungsfähigkeit der optischen Fasertechnologie noch schneller weiterentwickelt als die der Microchips und ist nun bereits in der Lage die Kommunikation zwischen Schnittstellen auf Microchipebene zu übernehmen. In elektronischen Mikrochips hingegen, bereiten die wachsende Problematik der Wärme Abführung und die zunehmenden Kosten pro Bit groe Schwierigkeiten, weiterhin einfach durch eine Verkleinerung der Bauteile die Geschwindigkeit von Mikrochips zu erhöhen. Die Ineffiezienz siliziumbasierter Lichtquellen zusammen mit der Inkompatibilität der meisten Lasermaterialien mit der etablierten Siliziumtechnologie hat jedoch den Fortschritt hinsichtlich der Integration von Lichtquellen auf Microchips stark behindert. Eine mögliche Lösung bieten dabei Nanodrähte, die direkt auf Silizium integriert werden und dabei die auergewöhnlichen optischen Eigenschaften von kristallinen Halbleitermaterialien mit direkter Bandlücke beibehalten können. Darüber hinaus stellen die Materialien zusammen mit der einzigartigen Geometrie der Nanodrähte bereits alle nötigen Komponenten eines Lasers dar. Integriert auf Silizium könnten derartige kohärente Microchip-Lichtquellen einen großen Schritt in Richtung optischer Schnittstellen auf Microchipebene oder sogar photonischer Computer bedeuten, die im nächsten Jahrzehnt nichtmehr nur eine Vision bleiben könnten.

Dabei hat jedoch die schädliche Wirkung nichtstrahlender Oberflächenrekombinationen auf die optischen Eigenschaften von III-V Halbleitern die Herstellung von Nanodraht Lasern die im Nahinfrarotbereich arbeiten stark behindert. In vorangegangenen Untersuchungen mussten Nanodrähte zudem oft von ihrem Wachstumssubstrat entfernt werden um das Lasern zu ermöglichen, was jedoch den großen technologischen Vorteil ihrer monolithischen Integration zu nichte und ihre Eingliederung in Schaltkreise unmöglich macht. Neben ihrem großen Potential für zukünftige Anwendungen, bieten Nanodrähte eine einzigartige Plattform die neue Einblicke in die fundamentalen Dynamiken des Laserprozesses an der ultimativen Skalierungsgrenze photonischer Laser gewährt. Obwohl das Lasern durch Nanodrähte bereits von vielen verschiedenen Materialsystemen gezeigt wurde, hat die Licht-Materie Wechselwirkung in Nanodrähten bisher keine signifikante Aufmerksamkeit erhalten.

Diese Arbeit zeigt wie Nanodrähte konstruiert werden können um das Aussenden von Laserlicht im Nahinfroten Spektralbereich zu ermöglichen. Die Resultate zeigen die erste Beobachtung von Lasern von GaAs Nanodrähten unter gepulster optischer Anregung bei Raumtemperatur. Experimente bei denen ein kontinuierlicher optischer Pumpmechanismus verwendet wurde zeigen den Dauerstrichbetrieb von Nanodraht Lasern und

demonstrieren Linienbreiten kleiner als 200μeV. Untersuchungen der Ladungsträger- und Photondynamik in Nanodraht Lasern zeigen einen neuen Mechanismus auf, der die Phasenkopplung von Picosekunden Pulspaaren auf langen Zeitskalen ermöglicht und den Betrieb mit Modulationsraten >200GHz erlaubt. Des weiteren wird eine neuartige Nanowire Laser Geometrie zur monolithischen Integration auf Microchips vorgestellt, die schließlich erfolgreich demonstriert und als Patentantrag eingereicht werden konnte. Die Außergewöhnlichen Eigenschaften von GaAs Nanodraht Lasern kombiniert mit ihrer einzigartigen Fähigkeit zur monolithischen Integration auf Silizium verleihen Nanodrahtlasern das Potential Einfluss auf ein breites Spektrum an integrierten, optoelektronischen Technologien zu nehmen und könnten gleichzeitig einen Schritt in Richtung der Vision photonischer Microchips bedeuten.

Contents

1 Introduction

1.1 Lasers for optical communication applications

The discovery of **L**ight **A**mplification by **S**timulated **E**mission of **R**adiation (LASER) has founded and driven a variety of research fields and technologies during the past century and has revolutionized digital communication during the past 40 years [1] [2]. Fueled by the semiconductor research in the 1970's, first small, robust and cost efficient laser devices were fabricated and have now became an indispensable part of the everyday life today [3]. The impact of laser devices on modern technology is also reflected by the large variety of applications that range from sensing and metrology and computer mice to high bandwidth fiber optic communication networks. Consequently, technological advantages in digital communication play a huge role for future human society and their political and economic success. Hence, extensive effort is invested to push laser based optical fiber communications towards comprehensive network coverage across many countries. According to the goals of the agenda of the European Union, each citizen in the EU is planned to have access to at least 30Mbit/s Internet data rate by 2020 [4]. We continue in this section, by presenting the fundamental principles of lasing operation and how they are applied in commercially available semiconductor lasers today.
Semiconductor lasers consist only of three fundamental constituents: an arrangement of mirrors, a gain material and an electrical or optical pump mechanism [5]. The gain material can be any direct bandgap semiconductor material. In a highly simplified picture, the band-structure can be described as an electronic few level quantum emitter with several distinct energy states. Depending on the charge occupation of the energy states, the gain material either predominantly absorbs or emits light during interaction with an optical field. Providing that charges occupy the higher energy (excited) state, an optical field can stimulate the emission of additional photons. This emission is consequently referred to as stimulated emission [5].
The stimulated emission is provided by the mirror system that recirculates initial spontaneously emitted light (seed) in the region of the gain material while the pump mechanism excites charges to the higher energy state. If the pumping is weak, the majority of charge carriers will remain in the energetically lower states and, thus, absorption dominates over stimulated emission. This situation is inverted (population inversion) if the pumping is strong enough such as to excite the majority of charge carriers to the excited state. In the case of population inversion, stimulated emission can become

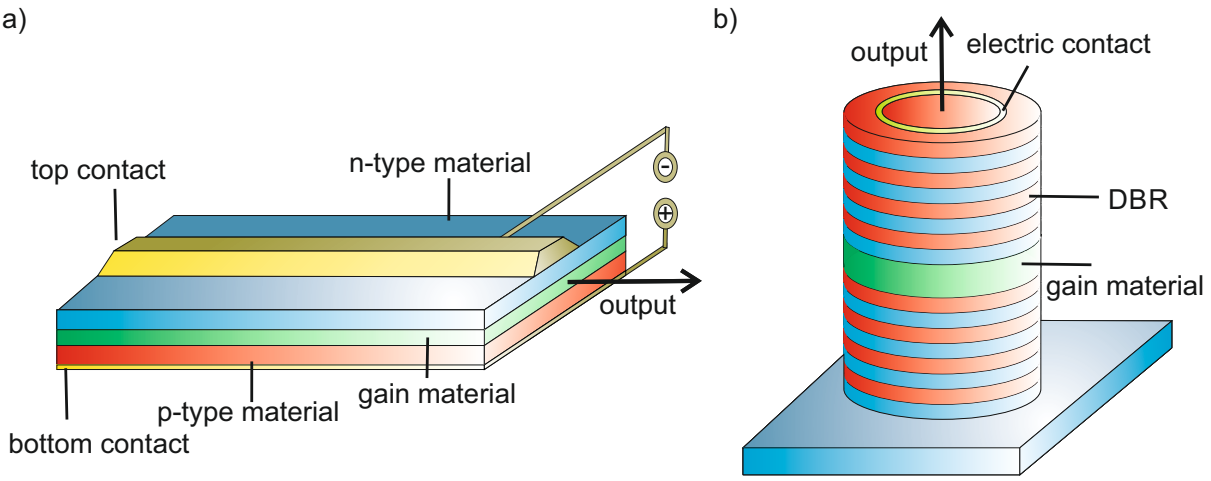

Figure 1.1. *Schematic illustration of an edge emitting laser device. The active gain region (green) is sandwiched between p-type (red) and n-type (blue) semiconductor material that are contacted by a positive top contact and a negative bottom contact, respectively. The optical cavity is formed by the cleaved edges of the wafer and determines the emission direction and modal structure of the laser light parallel to the wafer plane (arrow). b) Schematic illustration of a VCSEL device. The gain material is sandwiched between periodic layers with different refractive indices (red and blue) forming a DBR cavity perpendicular to the wafer plane leading to a vertical emission of the laser light (arrow).*

more probable than absorption and the recirculating light becomes amplified. This amplification is accompanied by a transfer of the direction, the frequency, the polarisation and the phase from the initial to the stimulated light field [5]. Providing that this amplification overcompensates losses due to e.g. imperfections of the mirror system (laser threshold), this process leads to a highly directional and coherent light beam that is partially transmitted from the optical cavity [5].
The challenge to build a laser is, therefore, to combine semiconductor gain material with a mirror system and a pump mechanism such that the laser threshold can be reached. However, the high refractive index contrast at the interfaces between semiconductor material and air is often already sufficient to provide the required reflection for lasing operation. In this most simple laser system, light undergoes total internal reflection at the top, bottom and cleaved lateral side facets of a wafer piece as depicted schematically in Fig. 1.1. Therefore, the wafer geometry determines the emission direction of the laser light that is partly reflected and transmitted at the end facets of the wafer piece. Typically, reflectivities of only $\sim$30% from the cleaved end-facets of the wafer are sufficient to achieve lasing operation [6]. This cost efficient and, therefore, commercially highly relevant type of lasers are referred to as **edge emitting lasers** [7] that were developed in the 1970's. The layer structure depicted in Fig. 1.1a) shows a gain material (green layer) sandwiched between a n-type (blue) and a p-type (red) semiconductor material

that together form a p-n junction. If now a voltage is applied between the top and bottom contacts (yellow) in forward direction, electrons and holes are injected into the gain material where they can occupy excited states. Electron-hole recombination to lower energy states is accompanied by the emission of photons that recirculate in the longitudinal direction inside the gain material and provide optical feedback. Although their simplicity and cost efficiency makes edge-emitting laser devices often favoured over more sophisticated device structures, multimode laser emission caused by the Fabry Pérot type cavity and high lasing threshold currents of typically $\sim$10mA [8] renders edge emitting devices often inferior to surface emitters in sensing and optical communication applications that require highly coherent, single frequency output.
However, distributed feedback (DFB) and distributed Bragg reflector (DBR) lasers constitute a technologically highly relevant development of this most simple semiconductor laser structure [9]. The implementation of periodic reflection layers inside the gain material (DFB) or at the facets of the laser structure (DBR) provides wavelength selective feedback that enables single mode operation and a strong reduction of the lasing threshold [9]. Consequently, DFB and DBR edge-emitting laser devices opened the markets for long-haul fiber optic communication links and optical amplifiers and strongly contributed to the development of the Internet.
The consequent drive to reduce the energy consumption per bit of information has fueled the development of nano-scaled transmitters starting with **V**ertical **C**avity **S**urface **E**mitting **L**asers (**VCSEL**s) [10] in the 1980's and 1990's. This concept uses optical cavities formed by pairs of DBRs that are grown on the substrate, separated by a $\lambda/2$ or $3\lambda/2$ thick layer of gain material. A typical device structure is schematically depicted in Fig. 1.1b) that shows the gain material (green layer) sandwiched between two wavelength selective DBR structures (red and blue layers). The circular top contact (yellow) surrounds an aperture that enables efficient light extraction from the device with excellent beam profiles and efficient coupling to optical fibers.
The reflectivities >99% provided by the DBRs very efficiently recirculate light propagation perpendicular to the wafer surface and enable vertical emission of single mode laser light [11]. The consequent miniaturisation of the lateral dimensions of the device enables the fabrication of tens of thousands VCSELs on a single 3" wafer. Furthermore, the high quality of the DBRs strongly reduces the laser threshold while the small dimensions provide high photon densities and ultrafast modulation rates of the VCSEL [11]. GaAs based VCSELs recently demonstrated impressive transmission rates >50Gbit/s with an energy consumption as low as $\sim$20pJ/bit for a board-to-board communication [12]. This outstanding performance makes VCSELs the most powerful commercial data transmitters today [13].

1.2 Photonic microchips and interconnects - the vision

The benefits of using light to transmit information arises from the fundamental properties of photons that neither carry a rest mass nor electric charge. As a result, optical

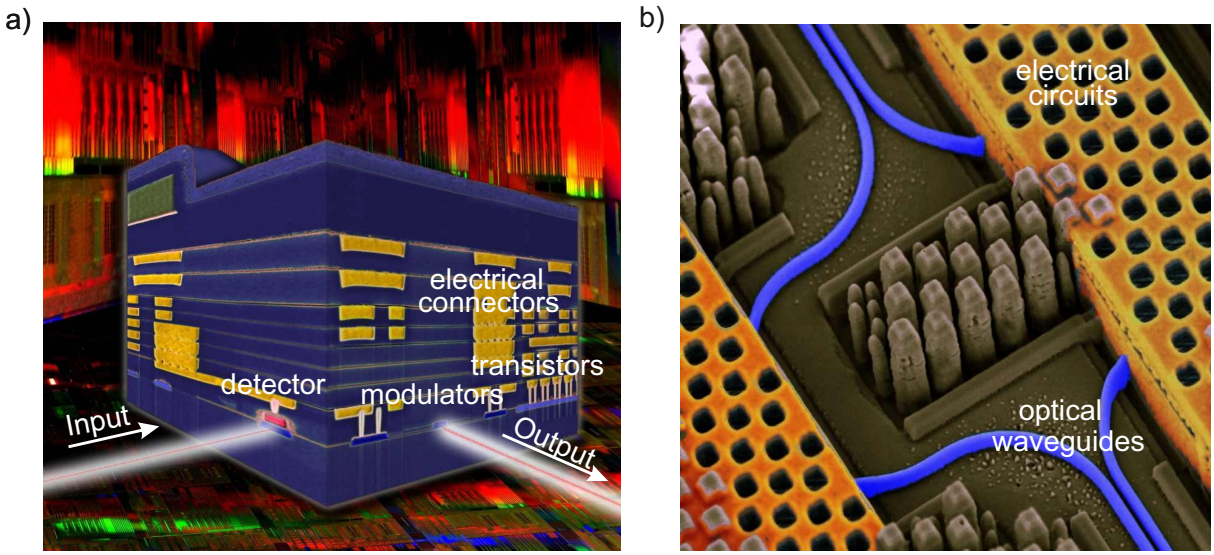

Figure 1.2. *Schematic illustration of an hybrid opto-electronic microchip developed by IBM. The chip integrates optical detectors (red rectangle) and modulators (blue rectangles) together with silicon transistors (red) and electric connectors (yellow) in a complex 3D architecture. The chip operates with light from an external source that is depicted by the red lines. b) SEM image of an optoelectronic circuit that combines optical waveguides (blue) and electrical circuits (yellow) on the same silicon microchip. Both images are taken from [16].*

information can be transmitted with the speed of light whilst remaining undisturbed by other electromagnetic signals transmitted over same channel. This properties make optical interconnects strongly superior over conventional electronic channels where propagating charges intrinsically suffer from ohmic losses and coulomb interactions, leading to heat generation and crosstalk between signals. In contrast, optical fiber networks have enabled high speed data communication and signal mutiplexing that further increases the data rates transmitted through an optical interconnect. The trend of the past thirty years shows that the fiber capacity of single optical fibers increased by a factor of 10 every four years, reaching a level $>10^{15}$ bytes/s (1 Petabyte/s) [14]. The consequent drive towards the miniaturisation of photonic interconnects using on-chip nanolasers could hold the promise to bring this world record data rates down to chip-level communication, boost the performance of super computers [15] and promote the "Internet of things" (IoT).

Figure 1.2a) schematically depicts a recently demonstrated optoelectronic microchip using an external light source [16]. The chip integrates optical modulators and germanium detectors together with copper wires (yellow) and silicon transistors (red) on the same chip [16]. The optical signal is modulated at a speed of 25Gbits/s, detected with germanium detectors and finally processed by electrical circuits. The optical waveguides (blue) are depicted together with the copper wires (yellow) on the SEM-image in

Fig. 1.2b). The chip can be packaged to a 5×5mm device with 50 transceivers that are capable to communicate to a second device with an extraordinary high bandwidth of 1.2 THz. This performance exceeds conventional chip-to-chip communication using electronics already by a factor of $\sim 1000\times$. The fact that the chip can be realised with CMOS compatible fabrication techniques further substantiates the practicability of photonic microchips for a new generation of digital devices.
Very recently, a novel electronic-photonic system that integrates over 70 million transistors and 850 photonic components on a single chip was presented [17], demonstrating logic, memory and interconnect functions [17]. The chip represents a first successful realization of a microprocessor combined with **on-chip photonic processing devices** and an **off-chip light source** to perform calculations at a speed of 2.5 Gbit/s directly using light.
Although information is increasingly transmitted with world record data rates via optical networks, data processing is still exclusively performed by electronics. The metallic interconnects used for electronic data processing, dissipate $\sim$50% of the dynamic power supplied to state of the art microchips [18]. Consequently, today's annual world data traffic of $\sim$1 Zetabyte (10^{21} bytes), is estimated to be responsible for 2% of the world's CO_2 emission. This contribution to the exhaust of climate gases is comparable to that of aviation and causes significant ecological damage regarding climate change [19].
In contrast, optical fiber technology provides vanishing loss rates down to 0.15 dB/km [11]. Therefore, the integration of optical interconnects on microchips could significantly reduce the energy consumption of digital devices and data centers [18].
Therefore, the miniaturisation and integration of optical chip to chip communication down to single microchips could enable a new generation of digital technology that operates close to the fundamental speed limit of light itself [2]. Besides dramatically enhanced performance and significantly improved environmental sustainability, optical microchips could also strongly impact society. Chip-to-chip and on-chip optical data processing could provide a platform for quantum encrypted protocols such as the BB84 [20] protocol and it's widespread implementation on private devices and large scale data centers. Therefore, the development of optical communication technology could pave the way for the implementation of encrypted quantum network protocols.
Although each of the fundamental components needed for optical computation already exist today, on-chip light sources to realize photonic microchips have remained a missing link [17]. Therefore, in order to realise:

- Optical data processing close to the speed of light
- A reduction of ecological damage caused by data transfer
- Novel platforms for quantum communication based on optics

, ultra scaled lasers that operate on the commercially vital silicon platform are urgently needed.

1.3 Lasers on silicon

Although strong progress has been achieved in on-chip optical signal processing during the past decade, the monolithic integration of laser sources on microchips still remain a missing link [21] [16] [17]. As modern microchip technology is almost exclusively based on the commercially important silicon platform, a full compatibility of integrated laser devices with silicon is inevitable for commercial applications [21]. This section provides a brief introduction to the challenges of integrating light sources on silicon and reviews the recent progress in the area.
Two fundamental material properties of silicon have inhibited the monolithic integration of lasers on microchips to date:

- The indirect nature of the silicon band-structure. [21].
- The dissimilar lattice constant of silicon compared to optically active III-V materials.

The indirect nature of the silicon band-structure has a deleterious impact on spontaneous and stimulated emission efficiencies and has hampered optical lasing from silicon to date. Furthermore, the planar growth of optically active III-V semiconductors on silicon introduces threading dislocations that have a deleterious impact on the optical properties of integrated gain materials [22].
However, besides the fundamental drawbacks of silicon regarding light generation, silicon is the material of choice to implement integrated optical circuits. The incredible purity of silicon wafers achieved in industry today and the intrinsic high performance dielectric provided by the natural oxide allow the fabrication of excellent waveguides with propagation losses typically $\sim 10\times$ smaller than that of similar compound semiconductor waveguides [21].
Furthermore, the high thermal conductivity of silicon provides excellent heat dissipation for devices. These features can be combined with state of the art CMOS technology that allows to fabricate all components required to build optical and hybrid-opto-electronic circuits for next generation data processing [21] [17].
Various approaches to realise monolithically integrated lasers on silicon have been investigated during the past decade [21]. For instance, continuous wave (cw) Raman lasing has successfully been implemented on silicon [26]. In this approach, the laser cavity constitutes a low loss silicon-on-insulator rib waveguide whose facets are coated with multilayer dielectric films and which is optically pumped by an external cw-laser source. The cw lasing was achieved by virtue of a reverse biased p-i-n diode embedded in the silicon waveguide which reduces two photon absorption induced free carrier absorption and, thus, reduces the lasing threshold to $\sim$180mW optical pump power. The performance achieved with this device exhibits linewidth < 100kHz and side mode suppression of 70dB, both being beyond the performance of most diode lasers. Other approaches aim at integrating bulk semiconductor gain material on silicon without threading dislocations [27] [28]. Large progress has been recently achieved using Ge/SiGe [27]

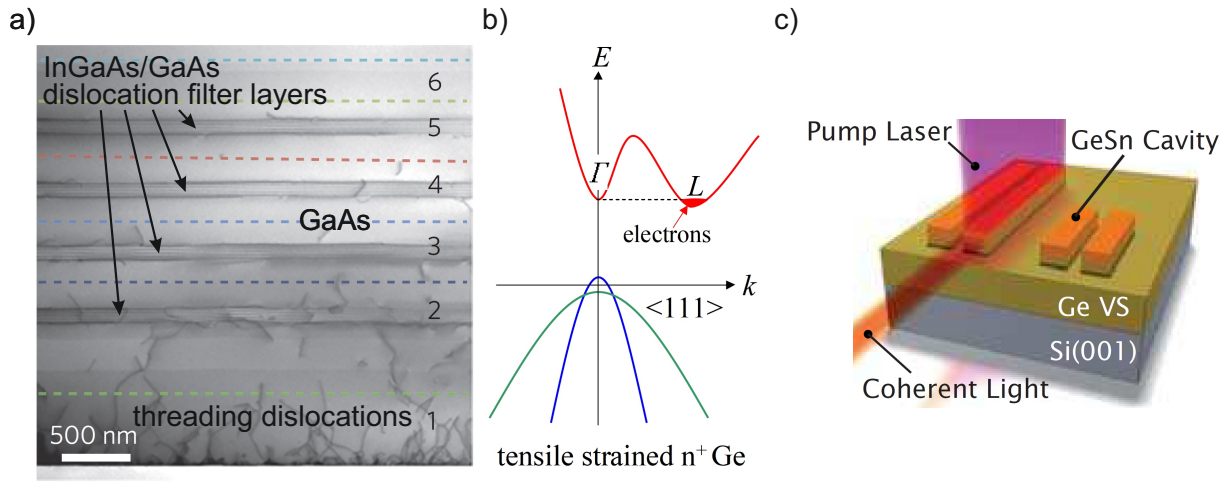

Figure 1.3. *a) SEM image of threading dislocations in a stack of GaAs and dislocation filter layers on silicon [23]. b) Schematic band-structure of tensile strained n^+ germanium [24]. c) Schematic image of an optically pumped GeSn laser on a virtual germanium substrate on silicon [25]. The images are taken from a)[23]b)[24] and c)[25].*

and GaSb [28] buffer layers for the planar growth of direct bandgap III-V material on silicon. This approach allows to strongly reduce strain and threading dislocations in the gain material and enable continuous wave lasing of a GaAs/AlGaAs laser and a GaInAsSb/AlGaAsSb on silicon at room temperature [27]. The threshold intensity of the GaAs/AlGaAs laser is approximately one order of magnitude lower (577A/cm^2) than that of the GaInAsSb/AlGaAsSb laser (5kA/cm^2). However, the GaInAsSb/AlGaAsSb laser emits at the technologically important telecom wavelength of 1.55μm which also allows a coupling to silicon waveguides. In comparison, the GaAs/AlGaAs laser emission at 858nm is energetically above the silicon bandgap. In a similar concept, a low density of threading dislocations on the order of 1×10^5cm^{-2} was achieved in III-V epilayers by combining a nucleation layer and dislocation filter layers with in situ thermal annealing [23]. Figure 1.3a) shows a SEM image of GaAs grown on silicon [23]. The threading dislocation density clearly decreases from bottom to top after each InGaAs/GaAs dislocation filter layer, enabling very recently the growth of an InAs/GaAs quantum dot laser on silicon. The device exhibits a low threshold current density of 62.5A/cm^2 and room temperature output power exceeding 105mW operation up to a temperature of 120 °C [23]. In contrast, the integration of germanium on silicon does not require buffer layers as the lattice mismatch is only 0.2-0.25% [21]. The consequent strain caused by the monolithic integration of germanium on silicon can lead to a reduction of the energy mismatch between the direct and the indirect bandgap of germanium down to 115meV [24]. The schematic band-structure diagram of tensile strained n^+ germanium presented in figure 1.3b) [24] shows the reduction of the energy separation between unpopulated states in the Γ- and the *L*-valley by extrinsic electron population of the the latter. In a

situation where the *L*-valley is populated to a energy level higher than the Γ-valley, direct transitions at the the *L*-point are strongly enhanced. An extrinsic electron density of $7.6\times10^{19}/\mathrm{cm}^3$ achieved by n-type doping was calculated to provide a net material gain of $\sim$400/cm from the direct gap transition of germanium [24]. Experimental evidence of lasing from tensile strained germanium on silicon [29] was demonstrated from an edge emitting waveguide device subject to pulsed optical excitation with a threshold of $\sim30\mathrm{kW}/\mathrm{cm}^2$. Another approach uses direct bandgap germanium-compound semiconductors such as GeSn to achieve lattice matched integration of gain material on silicon [25]. Figure 1.3c) shows the optical cavity and the gain material that is provided by a direct bandgap Ge/Sn alloy waveguide on top of a virtual germanium substrate grown on silicon [25]. With this approach, optically pumped lasing of direct bandgap GeSn on silicon was recently demonstrated under pulsed excitation at temperatures <90K with a lasing threshold of $\sim325\mathrm{kW}/\mathrm{cm}^2$ at 20K [25]. Although the innovative systems described above enabled coherent light emission on silicon, these concepts suffer from significant drawbacks that rendered their commercial application impossible to date. Silicon Raman lasers have very high lasing thresholds of $\sim$20mW and required external laser sources for the optical pumping [26]. Buffer layer concepts do not provide reliable laser fabrication methods which are vital for their mass production [21]. Although the strain of germanium on silicon could reduce the energy mismatch between the direct and the indirect bandgap, germanium remains an indirect bandgap semiconductor that requires very high optical pump energy of $\sim5\mu$J per pulse to populate the L-valley and promote lasing from the direct bandgap at the Γ-valley. Therefore, defect free, direct bandgap III-V gain materials remain clearly superior over existing laser on silicon technology described above. They provide bandwidths spanning from the visible to the infrared [30], room-temperature lasing [31] [32], hetero-structues with extremely low lasing thresholds, high temperature stability [33] and modulation rates of >50Gbit/s [12]. Furthermore, they can be easily doped, fabricated and electrically pumped [34]. Therefore, the direct integration of III-V gain material on silicon is often regarded as the "holy grail" of semiconductor laser technology. The demonstration of electrically driven coherent light sources on silicon would undoubtedly boost the realization of future optical microchips besides enabling a new generation of low power semiconductor lasers [35]. This vision can potentially be put into practice by nanowire lasers as studied in this thesis [32] [36] [37] [38] [39] [40] [41].

1.4 Nanowire lasers - state of the art

Semiconductor nanowires have recently emerged as highly attractive for photonic device applications [42] [43] [44] [45]. The unique one-dimensional nanowire geometry facilitates elastic strain relaxation making it possible to combine semiconductor materials with dissimilar lattice constants without introducing threading dislocations that have a deleterious impact on device operation [46] [47]. Here, a prominent example is the growth of III-V semiconductors with high optical efficiency directly on silicon substrates.

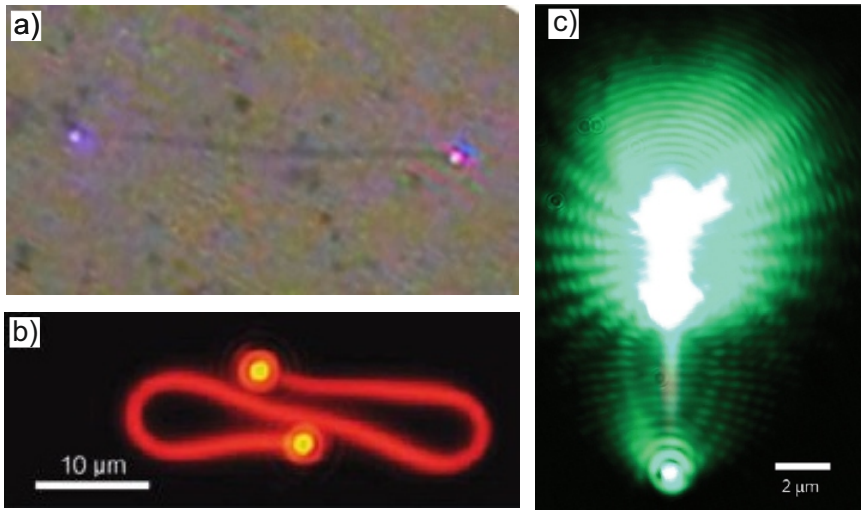

Figure 1.4. *a) GaN nanowire laser emitting at ∼380nm [53]. b) CdSe nanowire laser emitting at ∼738nm [54]. c) CdS nanowire laser emitting at ∼495nm optically coupled to a second CdS nanowire [57]. The images are taken from a)[53]b)[54] and c)[57]*

.

To date, a wide variety of high quality nanowire-based photonic and optoelectronic devices have been realized including solar cells [48], photodetectors [49], light emitting diodes (LEDs) [50] [51] and nanowire lasers [52]. This section reviews recent progress in the area of nanowire lasers and introduces the work on GaAs/AlGaAs core shell nanowire lasers presented in the subsequent chapters of this thesis.
Combining the potential for optical waveguiding, resonant recirculation and gain in a single nanostructure, nanowires are capable of lasing operation when excited optically or electrically [31] [32] [52]. In the past years, lasing operation from individual nanowires has been reported for a broad range of semiconductor materials [53] [54] [55] [56] [31] [32]. However, a significant bottleneck in many of these devices is the large optical absorption by the substrate. Therefore, the nanowire lasers presented in many previous works typically had to be removed from their growth substrate in order to expose both nanowire end facets to air and, thus, achieve sufficient optical feedback for lasing operation. The figures 1.4 a), b) and c) show three different transferred nanowire lasers operating at ∼380nm (GaN, blue) [53], ∼738nm (CdSe, red) [54], and ∼495nm (CdS, green) [57], respectively. The mechanically flexible CdSe nanowires presented 1.4 b) are bent to form loop mirrors from which each represents an optical cavity. The Vernier effect from two coupled loop cavities leads to the suppression of multiple longitudinal lasing modes and enables single mode operation of the nanowire laser [54]. Figure 1.4 c), shows two adjacent nanowires that are aligned along their axes and separated by a 160nm ion-milled gap [57]. The nanowire on the top of the image represents the optically pumped nanowire laser (input nanowire) that acts as input source for a second nanowire which represents the optical switch (output nanowire). The transmission through the

output nanowire can be controlled by an external light source (Ar+ laser) that is focused onto the switch, that operates via the formation of microcavity exciton polaritons and strong non-linearities. If the external light source is switched on, exciton-polaritons are generated by the light matter interactions in the output nanowire cavity and populate the lower polariton branch [57]. These occupied states can now scatter light from the input nanowire laser and suppress the transmission of the lasing frequency through the output nanowire [57]. Consequently, the stimulated polariton scattering process in the output nanowire enables all-optical switching of the device and the demonstration of optical NAND gates functionally with CdS nanowires [57]. However, the uncontrolled position and random geometry of the nanowire lasers after their mechanical transfer has rendered their use as large-scale integrated photonic devices impossible [58] [59].
Very recently, strongly tapered nanopillars supporting helical optical modes have been shown to exhibit lasing operation directly on silicon substrates [35] [60]. The helical waveguiding of light inside the nanopillars leads to very flat angles of incidents at the nanopillar-silicon interface and, thus, provides sufficient reflections for lasing operation. However, the large geometrical footprints of such nanolasers accompanied by multimode wave-guiding intrinsically leads to fairly low spontaneous emission coupling factors of $\beta \sim 0.01$ and, thereby, relatively high pump thresholds for lasing. Furthermore, such helical modes have complex radiation patterns that complicates their coupling to single mode optical fibers, a key pre-requisite for optical data communication.
Chapter 2 of this thesis presents lasing from individual GaAs/AlGaAs nanowire lasers subject to pulsed optical excitation [32]. The capability of the GaAs/AlGaAs nanowire lasers to operate up to room temperature substantiates their strong potential for their implementation into future photonic devices. Furthermore, as presented in chapter 3, the GaAs/AlGaAs nanowire lasers are capable of continuous wave lasing with enhanced temporal coherence and reduced linewidths [37]. However, the refractive index mismatch between the refractive index of the GaAs waveguide (n_{GaAs}) and the refractive index of the silicon substrate (n_{Si}) of $\Delta n = n_{GaAs} - n_{Si} < 0.1$ results in modal reflectivities below 1% [61] that are not sufficient to provide the required optical feedback for lasing operation of the monolithically integrated devices [62]. Therefore, monolithic integration of operational nanowire lasers on silicon substrates has remained a missing link [21] [44].
Chapter 4 of this thesis presents a novel nanowire laser geometry that enables low order mode lasing of monolithically integrated devices on silicon [36]. Another strong requirement for nanowire lasers to be used as optical signal processing devices are high pulse repetition rates $\geq$ 3GHz that would allow the nanowire transmitters to compete with the clock speeds of state of the art electronics [17]. Chapter 5 of this thesis presents studies of the ultrafast gain dynamics of GaAs/AlGaAs nanowire lasers. The nanowire lasers investigated exhibit repetition rates of 200GHz [38] and pulse durations $\sim$2ps. Spectral analysis of the interference of two subsequent nanowire laser pulses reveals that phase information is stored in the nanowires for 30ps, much longer than the $\sim$2ps duration of the individual pulses [38]. The findings demonstrate the large potential of

Features of nanowire lasers	Visible	NIR
Monolithic integration	–	[36]
Continuous wave	[63]	[36]
Room temperature	[64][65]	[31][32][31]
Ultrafast operation <10ps	[66]	[38]
Single mode	[54]	[31][36][37][32]
Phase locking	–	[38]
Electrically driven	[52]	–

Table 1.1. *Performance specifications of nanowire lasers and their state of the art. nanowire lasers that operate in the visible regime are depicted in the center column and NIR nanowire lasers are depicted in the right column. Citations that are listed in green brackets depict results that are demonstrated from other groups. Citations that are listed in blue brackets depict results that will be presented in this thesis.*

GaAs/AlGaAs nanowire lasers as high speed light sources and optical memories [38]. An overview of features that render nanowire lasers highly attractive for commercial applications is depicted in Table 1.1. As the deleterious impact of non-radiative surface recombination especially on the optical properties of III-V nanowires has strongly exacerbated the realization of nanowire lasers that operate in the commercially important near infrared (NIR), Table 1.1 lists the recent progress of nanowire lasers operating in the visible and NIR spectral range individually.

The recently developed technique to passivate non-radiative surface recombinations in GaAs nanowires by virtue of an AlGaAs shell around the GaAs nanowire core has strongly enhanced the emission properties of this III-V nanowires and enabled the research presented in this thesis [67]. Table 1.1 clearly shows that including the results presented in this thesis, all vital operation modes and implementations for the commercial use of nanowire lasers have now been demonstrated. By combining monolithic integration, room temperature operation and electrical pumping of nanowire lasers, photonic microchips and potentially a new generation of semiconductor lasers can now be generated.

2

Room temperature lasing from individual GaAs-AlGaAs core-shell nanowires

Semiconductor nanowires are widely considered to be the next frontier in the drive toward ultra-small, highly efficient coherent light sources [42][35]. They provide the potential to generate highly localised, intense monochromatic optical fields in a geometry that is very well suited to an efficient coupling to highly integrated nanophotonic elements and optical circuits [57][35][68]. Indeed, the high refractive index of typical semiconductor materials allows the physical size of lasers to be scaled down to only a few hundred nanometers, whilst the unique nanowire geometry naturally facilitates low loss optical waveguiding and optical recirculation in the active region.

To date, lasing from nanowires has been demonstrated using a range of different material systems that span the UV and visible regions of the spectrum. This includes ZnO [65], group III-nitrides [53], II/VI materials [69] and, most recently, III/V nanowires and nanopillars [62] [35] [70] [71] [72]. Very recently, infrared lasing has been observed at low temperature using InGaAs nano- needles grown epitaxially directly on silicon and silicon-MOSFETs by exploiting whispering gallery like optical modes [35]. Furthermore, first indications of amplified spontaneous emission and lasing have been reported from optically pumped GaSb [71] and GaAs-GaAsP [72] core-shell nanowires. For nanowire-lasers that use GaAs as a gain medium, theoretical analyses of the modal gain have indicated that continuous wave lasing should be possible in detached nanowires [62] [73] [74]. The end-facet reflectivity ($\sim$0.6) is sufficient to reach transparency in nanowires with a length of a few micrometers by engineering the confinement of the optical mode via their diameter [42] [62]. However, the deleterious impact of non-radiative surface and Auger recombination has limited progress in the technologically important near infrared spectral range although lasing is predicted to be within reach of GaAs nanowires with sufficiently high crystalline quality and lengths exceeding a few micrometers [62] [75].

In this chapter, we report infrared lasing up to room temperature from individual core shell GaAs-AlGaAs nanowires. When subject to pulsed optical excitation, nanowires exhibit lasing, characterized by single mode emission at 10K with a linewidth $<$60GHz. The major role of non-radiative surface recombination [76] [77] is obviated by the

presence of an AlGaAs shell around the GaAs active region. Remarkably low threshold pump power densities down to $\sim$760Wcm^{-2} are observed at 10K, with a characteristic temperature of T_0=109$\pm$12K and lasing operation up to room temperature. The results show that, by carefully designing the materials composition profile, high performance infrared nanowire-lasers can be realised using III/V semiconductors.

2.1 Sample preparation of GaAs-AlGaAs core shell nanowire-lasers

Besides efficient light confinement inside the nanowire cavity, gain materials with high spontaneous emission and low non-radiative recombination rates are vital to achieve lasing operation. However, the deleterious impact of non-radiative surface recombinations on the optical properties of GaAs nanowires has strongly exacerbated the fabrication of nanowire lasers of this technologically important material system [76] [77].
In order to overcome this challenge, we designed GaAs-AlGaAs core-shell nanowires that facilitate an optical microcavity whilst maintaining the excellent optical properties of the GaAs gain material [67].
The GaAs/AlGaAs core shell nanowires presented in this chapter were grown using solid source molecular beam epitaxy (MBE) on Si(111) substrates that were thermally oxidized to produce a 20$\pm$1nm thick SiO_2 mask layer [78]. Before growth, the oxide was thinned using an aqueous, dilute NH_4-HF solution to produce a $\sim$2 nm thick SiO_2 layer containing pinholes to the Si(111) substrate which act as nucleation sites for nanowire growth [78] [79] [80] [81] as depicted in Fig. 2.1a). The prepared substrates were then transferred into a Gen II MBE system and held at 700°C for 20 minutes to remove surface contaminants before being cooled to the nominal growth temperature of 610°C. Figure 2.1 shows a schematic illustration of the subsequent steps of the nanowire laser growth. The nanowire core is synthesized from a small aperture inside a SiO_2 mask on top of the Si substrate as depicted in Fig. 2.1a). The growth is performed by a self-catalysed (Ga-droplet mediated) vapour-liquid-solid growth mode [78] using Ga- and As- fluxes of 0.025nm/s and 0.103nm/s as depicted in Fig. 2.1b), respectively. After 210 minutes of the nanowire growth depicted in Fig. 2.1c), the nanowires have a lengths of 11-16μm and a core diameter of 80$\pm$5nm. The need for strong optical mode confinement requires nanowire diameters exceeding 300nm, which was achieved by overgrowing the nanowires with a thick GaAs shell as shown in Fig. 2.1d). For this growth step, the temperature was cooled down to 490°C while arsenic and gallium fluxes were increased to 0.19nm/s and 0.17nm/s respectively, resulting in a radial growth of GaAs until the desired core diameter of $\sim$330nm is reached.
The effective suppression of non-radiative surface recombinations can be achieved using an $Al_{0.25}Ga_{0.75}As$ shell around the GaAs core that constitutes the gain medium of the laser [78] [67] [32]. The $Al_{0.25}Ga_{0.75}As$ shell (lattice constant a_{AlGaAs}=$\sim$0.5655 nm) is lattice matched to the GaAs core (lattice constant a_{GaAs}=$\sim$0.5652 nm) and allows the growth

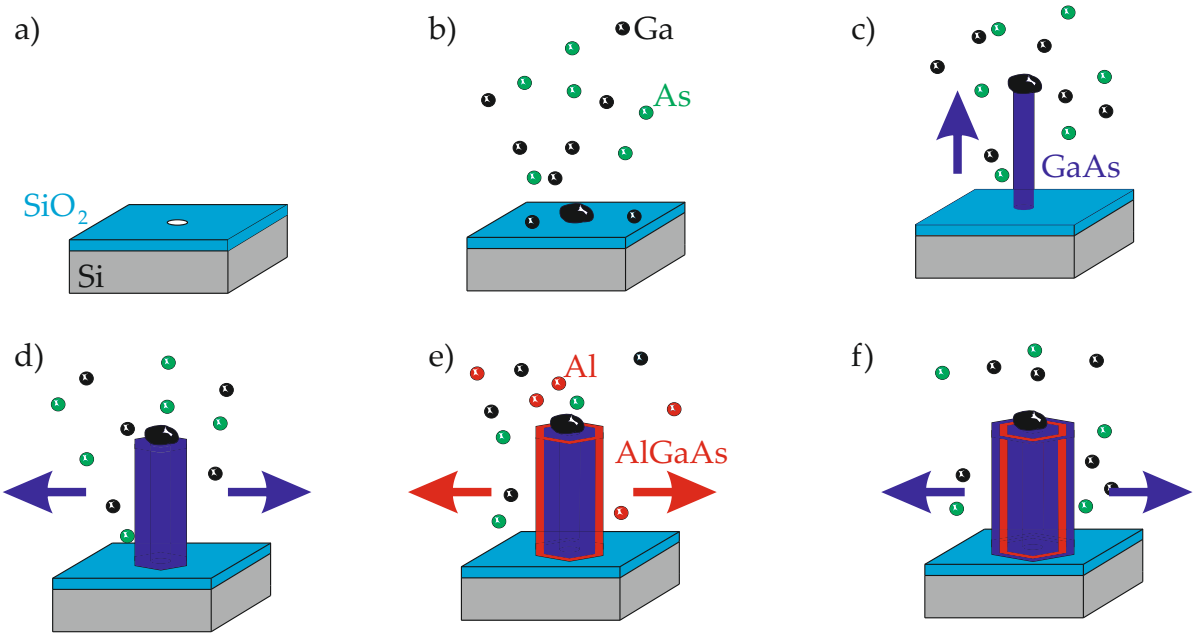

Figure 2.1. *Schematic illustration of the nanowire laser growth. (a) The silicon <111> substrate (grey) is covered with a prestructured SiO_2 layer (light blue). b) Ga atoms (black) diffuse on the substrate and form a droplet in predefined holes. c) The As atoms (green) dissolve in the Ga droplet and form crystalline monolayers of GaAs (blue) which leads to the growth of the thin GaAs nanowire core. d) The nanowire core is radially overgrown with a GaAs shell. e) The GaAs shell is overgrown with an AlGaAs passivation layer. f) The AlGaAs passivation layer is radially overgrown with a GaAs capping layer.*

of GaA/AlGaAs heterostructure without introducing threading dislocations. The Al concentration of $\sim$ 30% increases the bandgap of the $Al_{0.25}Ga_{0.75}As$ (E_{gap}=1.840eV) shell by $\sim$400meV compared to the GaAs (E_{gap}=1.424eV) core and introduces a $\sim$200meV potential barrier to prevent non-radiative recombination at the nanowire surface [82] [83]. As the AlGaAs potential barrier is much larger than the thermal energy of free charges in the GaAs gain material at room temperature $E_{therm}=k_BT$=26meV, the AlGaAs shell efficiently suppresses charge diffusion to the nanowire surface [76] [77]. The overgrowth of the GaAs nanowire-core with a thin AlGaAs passivation layer is depicted in Fig. 2.1e) [67]. Hereby, the Al-flux was set to 0.057nm/s, to grow a 5$\pm$1nm thick $Al_{0.25}Ga_{0.75}As$ radial shell around the GaAs core. Finally, the epitaxy of nanowire lasers is completed by the growth of a thin layer of GaAs around the AlGaAs shell to prevent oxidation as presented in Fig. 2.1f). Figure 2.2a) shows a scanning tunneling electron microscopy (STEM) image of similar nanowires grown by Daniel Rudolph [67], who also performed the growth of the GaAs/AlGaAs/GaAs nanowire lasers presented in this chapter. The

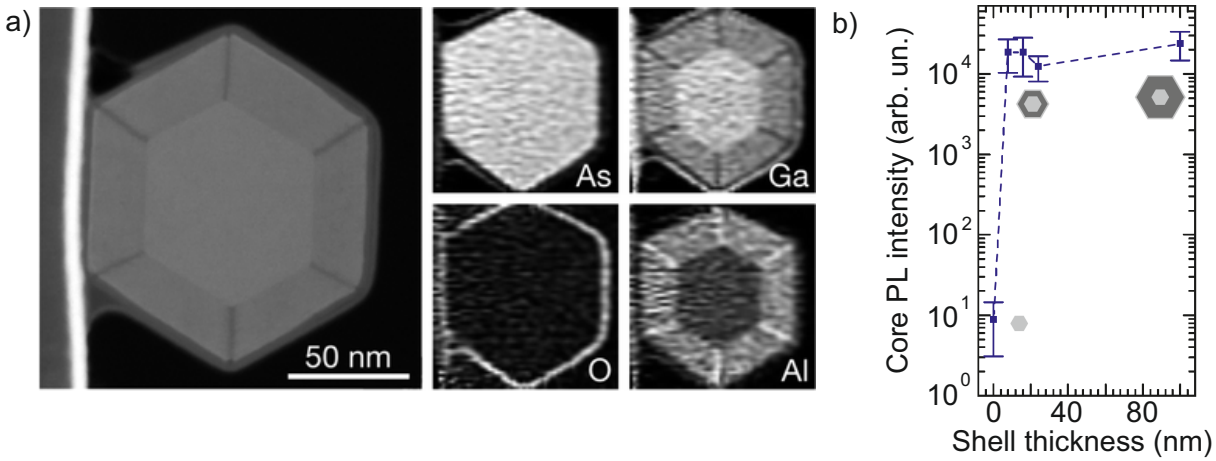

Figure 2.2. *a) Scanning tunneling electron microscopy (STEM) image of a GaAs/AlGaAs/GaAs core shell nanowire with total diameter of ∼ 120nm. The STEM image is taken from Rudolph, D. et al. [67]. b) Photoluminescence intensity of a 80nm thick GaAs core passivated by an AlGaAs shell with various shell thicknesses. The measurements presented in this figure were obtained as part of the work of Daniel Rudolph [78] [78] but not within the scope of this thesis. Daniel Rudolph also grew the Nanowire Lasers studied in this Chapter.*

direction cross-sectional STEM and associated chemical analysis reveal a 6-fold Al-rich substructure along the corners of the hexagonal AlGaAs shell where the Al-content is up to x∼0.6, a factor of ∼2× larger than the body of the AlGaAs shell [67]. Transmission electron microscopy and Raman spectroscopy measurements performed on reference samples grown under similar conditions showed that the nanowires produced have a predominant zincblende crystal structure with occasional twin plane defects in the middle region of the nanowire and heavier twin defect densities at the bottom and top ends of the nanowire [79]. Figure 2.2a) shows the photoluminescence intensity of GaAs nanowires as a function of the AlGaAs shell thicknesses. The findings of [67] reveal that an AlGaAs shell of ∼10nm thickness is sufficient to strongly prevent non-radiative surface recombination and extremely enhance the photoluminescence intensity of GaAs nanowires by ∼3 orders of magnitude [67]. Provided that light recirculation inside nanowire is supported by the nanowire cavity, lasing operation of the GaAs/AlGaAs core shell nanowire is predicted to be within reach [62]. Further details pertaining to the growth procedure of GaAs-AlGaAs core-shell nanowires and their structural and morphological properties can be found in Refs. [79], [67].

Figure 2.3a) shows a typical scanning electron microscope (SEM) image of the as-grown nanowire-laser structures, with lengths varying from 11-16μm. In this geometry however, the extremely low refractive index mismatch between the GaAs nanowires (n_{GaAs} ∼3.6 [84]) and the silicon substrate (n_{Si} ∼3.6 [85]) suppresses reflection from the

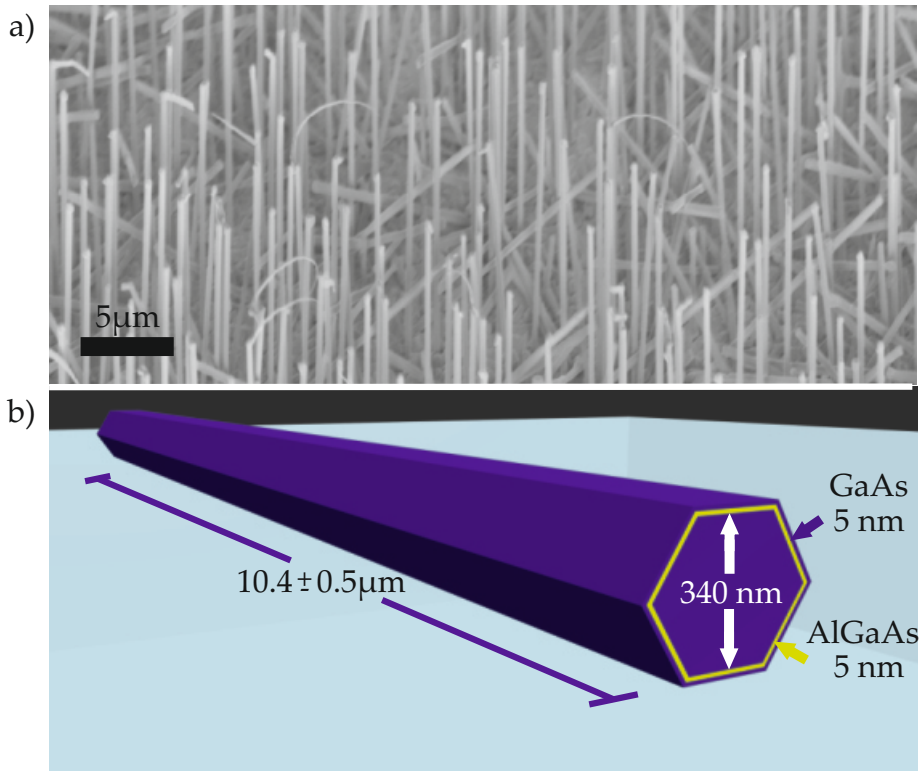

Figure 2.3. *As grown GaAs/AlGaAs nanowires and schematic illustration of the transferred nanowire laser structure. (a) Scanning electron microscope images of the as-grown core-shell GaAs-$Al_{0.25}Ga_{0.75}As$ nanowires showing typical lengths ranging from 11-16µm and an areal density of the order of $\sim 10^8 cm^{-2}$. The scale bar is 5µm.(b) Schematic representation of a nanowire transferred onto a glass microscope slide showing the active GaAs core with a nominal diameter of 340nm, the 5nm thick AlGaAs diffusion barrier and 5nm thick surface capping layer.*

bottom facet of the nanowire. Consequently, no optical feedback and, thus, no lasing operation can be obtained from the nanowires in the as-grown geometry presented in Fig. 2.3a). However, as shown in the next section, optical modes that propagate inside the nanowire can be efficiently be reflected (R$\sim$60%) at the nanowire air interface [62]. In order to expose both nanowire end-facets to air, the nanowire-lasers were mechanically removed from the growth substrate and spatially dispersed onto a SiO_2 substrate. As the refractive index of the SiO_2 substrate (n_{SiO_2} $\sim$1.5 [86]) is well below the refractive index of the GaAs (n_{GaAs} $\sim$3.6 [84]), light is efficiently confined and guided inside the nanowire by total internal reflection [31] [32]. Figure 2.3b) schematically shows the core-shell nanowire geometry of such a transferred nanowire-laser, in which the end-facets define a longitudinal Fabry-Perot (FP) laser cavity [75].

2.2 Optical properties of nanowire cavities

Lasing in semiconductors requires strong light matter interactions that demand optimized structural properties of the device [72]. In order to achieve lasing operation of nanowires, the optical nanowire cavity must provide:

- optical waveguiding
- sufficient overlap of the optical mode with the nanowire gain material
- sufficiant reflections from the nanowire end-facets.

Therefore, the losses caused by the finite reflection of the nanowire end-facets must be compensated by the gain of the nanowire material g and satisfy the threshold condition:

$$g_{th} = \frac{1}{2\Gamma L} ln\left(\frac{1}{R_1 \times R_2}\right), \tag{2.1}$$

where g_{th} denotes the threshold gain, Γ denotes the mode confinement factor, L denotes the nanowire length, R_1 and R_2 denote the reflectivities at the nanowire end-facets [5]. The capability of nanowires to satisfy the threshold condition is studied and optimized using theoretical calculations obtained from a commercial-grade finite difference time domain solver (Lumerical Solutions) that allows the analysis of optical modes and their propagation in a given material environment. We continue in this section to present the results of calculations performed to simulate the ability of nanowires to realize efficient laser cavities.

Optical waveguiding along the nanowire axis is achieved if the refractive index of the nanowire material is larger than the refractive index of the surrounding and if the nanowire dimensions exceed the cutoff [62]. The optical modes supported by a nanowire waveguide can be characterised by the polarization and the intensity distribution of the confined light [68]. Fig. 2.4 shows the optical mode profiles inside a GaAs/AlGaAs core-shell nanowire with hexagonal cross-section. The mode profiles show the energy density distribution calculated using the numerical Maxwell equation solver (Lumerical MODE). Helical modes (HE and EH modes) such as HE_{11}, HE_{21}, HE_{31} and the EH_{11} shown in Fig. 2.4 have electrical and magnetic field components along the direction of the waveguide axes. Therefore, the mode follows a helical propagation path along the nanowire axis. The HE_{11} mode is often referred to as the fundamental mode since it exhibits a Gaussian beam profile which can be easily coupled to optical fibers. In contrast, transverse magnetic (TM) modes (e.g. Fig. 2.4 TM_{01}) have electric field components along the nanowire axes and a magnetic field perpendicular to the waveguide and transverse electric (TE) modes (e.g. Fig. 2.4 TE_{01}) are characterized by magnetic field components along the propagation axes and an electric field perpendicular to the waveguide.

Light propagation at a wavelength λ inside a medium with refractive index n is strongly suppressed, if the waveguide diameter reduces below the fundamental cutoff diameter $d_{min} \sim \frac{\lambda}{2 \times n_{refr}}$. However, with increasing lateral waveguide dimensions above d_{min},

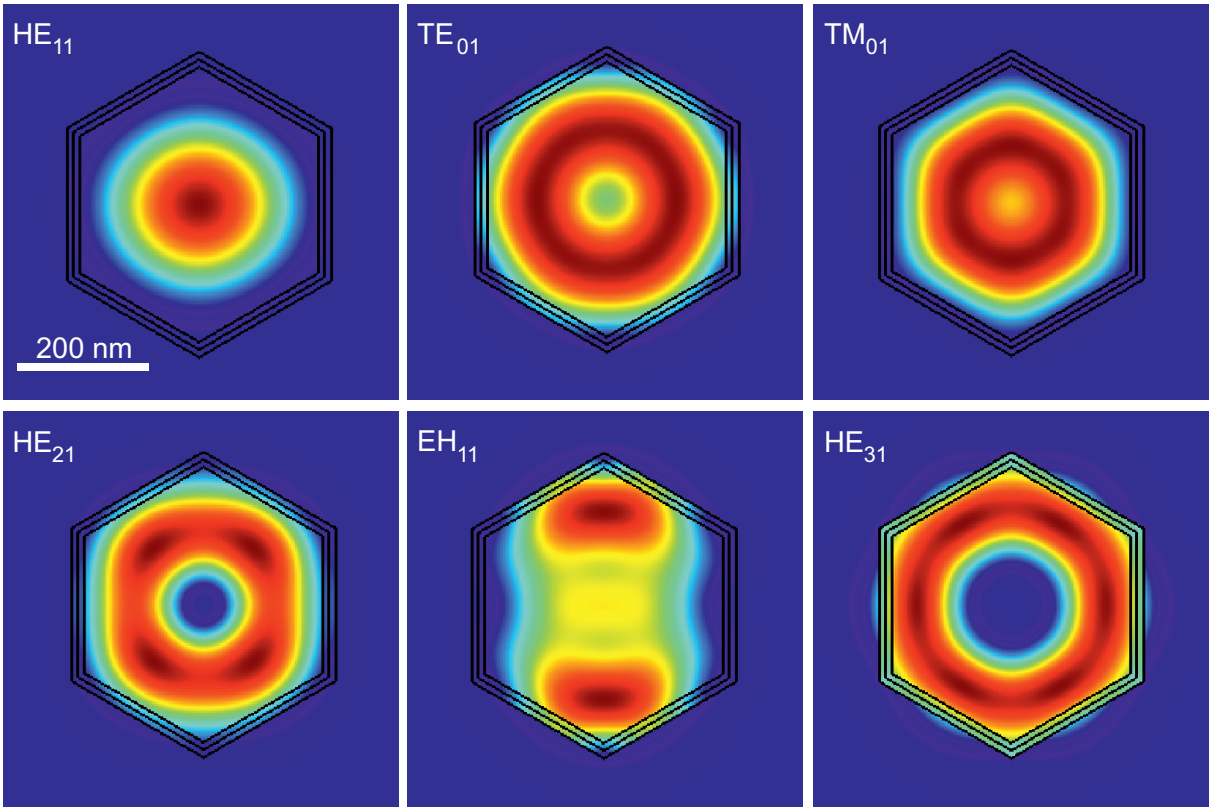

Figure 2.4. *Optical mode profile of the energy density distribution in a hexagonal GaAs/AlGaAs core-shell nanowire waveguide with a diameter of 400nm. The calcuations were performed using the numerical Maxwell equation solver (Lumerical MODE).*

integer multiples of λ/n can match the waveguide geometry and the total number of accessible optical states increases [62]. The optical cutoff of a particular mode can be determined by calculating the confinement factor Γ which provides a measure for the mode confinement inside the waveguide or active gain medium. The power confinement factor Γ_P traditionally used by the laser community is defined by the fraction of energy propagating inside a waveguide along the waveguide axes with respect to the total energy of the mode propagating along the waveguide axes:

$$\Gamma_P = \frac{\int_{A_a} d\rho Re(\frac{1}{2}\mathbf{E}(\rho) \times \mathbf{H}^*(\rho))\hat{z}}{\int_A d\rho Re(\frac{1}{2}\mathbf{E}(\rho) \times \mathbf{H}^*(\rho))\hat{z}} \tag{2.2}$$

[87]. A_a is the area of active medium and A describes the total area of the optical mode. $\mathbf{E}$ is the electric field and $\mathbf{H}$ represents the magnetic field of the optical mode at a postion ρ. The Γ_P value reaches 1 if the mode is completely confined in the gain medium and provides an intuitive measure for the overlap of light with the active material [87]. However, equation 2.3 is only valid for weakly confined optical modes and describes an

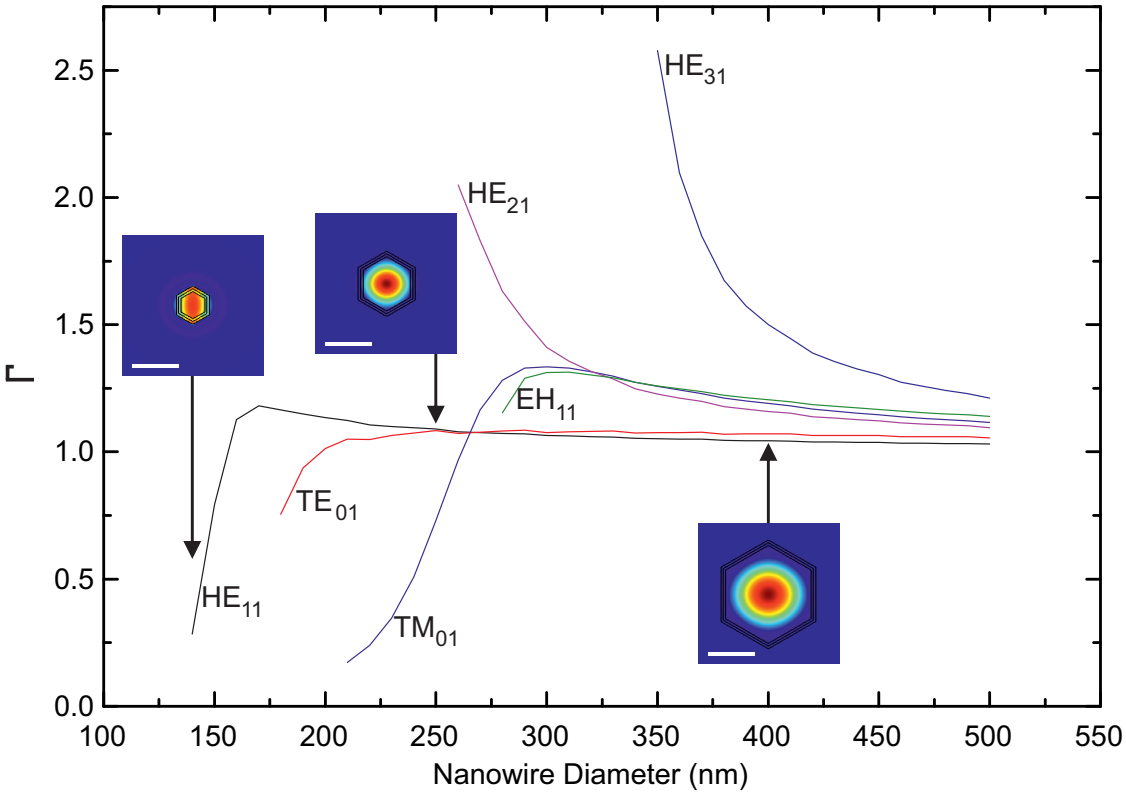

Figure 2.5. *Confinement factor of six optical modes propagating inside a hexagonal GaAs/AlGaAs core-shell nanowire as a function of the nanowire diameter. The insets show the mode profiles of a fundamental HE_{11} mode at nanowire diameters of 140nm, 250nm and 400nm. The mode profiles of the six calculated optical modes are presented in Fig. 2.4 for a nanowire diameter of 400nm.*

approximation of the actual waveguide confinement factor Γ_{WG} in the weakly guided limit [87]. In contrast, for strongly confined modes the waveguide confinement factor Γ can be > 1 and is used for e.g. rate equation analysis as presented in section 3.2. The waveguide confinement factor Γ is given by:

$$\Gamma_{WG} = \frac{\frac{n_a(\omega)}{2\eta_0} \int_{A_a} d\rho |\mathbf{E}(\rho)|^2)}{\int_A d\rho Re(\frac{1}{2}\mathbf{E}(\rho) \times \mathbf{H}^*(\rho))\hat{z}} \tag{2.3}$$

, with $n_a(\omega)$ being the refractive index of the gain medium at the frequency ω and η_0 being the intrinsic impedance [87]. Figure 2.5 presents the waveguide confinement factor Γ for the GaAs gain medium in a GaAs/AlGaAs nanowire as a function of the nanowire diameter, calculated for the six optical modes presented in Fig. 2.4. The three insets in Fig. 2.5 depict the mode profiles for a fundamental HE_{11} mode for diameters of 140nm, 250nm and 400nm. The insets of the fundamental optical mode clearly

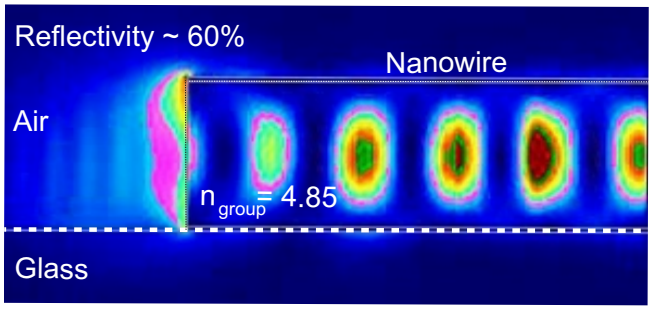

Figure 2.6. *Finite difference time domain simulation (FDTD) of the propagation of a fundamental HE_{11} mode in GaAs/AlGaAs nanowire with a diameter of 360nm transferred on a glass substrate. The calculations were performed using the commercial-grade FDTD simulation program "Lumerical FDTD".*

show that the overlap of the optical mode with the gain medium is strongly reduced with decreasing diameter d<d_{cutoff}, resulting in a gamma factor Γ ~0.3 at d=140nm. Single mode waveguiding of a fundamental HE_{11} mode can be achieved for nanowire diameters ~160nm which allows nanowire light sources to be easily coupled to optical fibers. However, for diameters $\gg d_{min}$, the number of coexisting optical modes increases. Interestingly, the high dispersion of low order modes at small waveguide diameters close to d_{cutoff} gives rise to mode confinement factors $\Gamma > 1$ for all the presented modes. The capability for single mode waveguiding together with $\Gamma > 1$ for low order modes provide the investigated GaAs/AlGaAs nanowires with excellent waveguiding properties lasing operation.
In addition to high confinement factors Γ, sufficient reflection from the nanowire end-facets is required to acheive optical feedback and finally lasing operation. This can be achieved by a large momentum mismatch between the light propagating inside the nanowire compared to the propagation in the surrounding medium. The photon momentum $\hbar k$ is given by $\hbar k = \hbar \frac{2\pi}{\lambda \times n_{group}}$ with n_{group} being the refractive group index defined by the optical mode, $\hbar$ being the Planck constant and λ being the wavelength in vacuum. Therefore, high values of n_{group} in the nanowire compared to the refractive index in vacuum n=1 are essential to achieve lasing operation. It must be noted that the nanowire waveguide provides two modes with different polarizations [68] that will here be referred to as HE_{11}^a and HE_{11}^b. The high dispersion in a 360nm diameter core-shell nanowire waveguide transferred to a glass substrate supports optical modes with low threshold gain and a calculated effective refractive group index of n_{group} = 4.85 for the HE_{11}^a and n_{group} = 4.86 for the HE_{11}^b mode, respectively. Both optical modes are indicative of a Fabry-Prot (FP) mode spacing

$$\Delta E = \frac{\hbar \pi c}{L \times n_{group}} \tag{2.4}$$

[74] of 10 meV for nanowires with L$\sim$11μm used in this work. The form of the guided optical fundamental mode in the in-plane (axial) direction is calculated by finite difference time domain (FDTD) simulations of a 360nm diameter core-shell nanowire waveguide transferred to a glass substrates as shown in Fig. 2.6. The calculations were performed using the commercial-grade FDTD simulation program "Lumerical FDTD". The simulations demonstrate the excellent overlap of the guided mode with the GaAs core, the formation of FP-modes in the axial nanowire resonator and the predominant losses from the end facets. The FDTD calculations indicate that the maximum reflectivity of the fundamental HE_{11}^{a} mode at the nanowire end-facets is $\sim$60%, translating to a maximum mode Q-factor of the Fabry-Prot resonator modes of Q_{max} $\sim$750, corresponding to a finesse of 5.7 for an 11μm long nanowire. This compares fairly well to the typical observed Q-factors of the Fabry-Prot modes observed in previous work in the spontaneous emission regime [75]. Using a confinement factor of Γ=1, an end-facet reflectivity of 60% and a nanowire length of 10μm in equation 2.1 results in a threshold gain of $\sim$500/cm and shows that lasing operation of GaAs/AlGaAs core shell nanowires should be within reach.

2.3 Rate equation model of nanowire lasers on Silicon

One of the most important aspects to optimize the energy efficiency of semiconductor laser devices, is to enhance the fraction of spontaneous emission that enters into the lasing mode. Therefore, optical modes that do not provide the lowest lasing threshold add additional loss channels to the laser and must be compensated by higher external pumping. Consequently, the energy consumption of a laser device to reach the lasing threshold is directly proportional to $1/\beta$, where β is the spontaneous emission factor representing the fraction of spontaneous emission that enters the lasing mode [88].
The small size and consequent ability of nanowire lasers to confine light in the nanowire gain medium at a scale close to the fundamental wavelength limit, could allow the structure presented in the previous sections to provide extremely energy efficient high-β low order mode lasing. In order to analyze the experimental data with respect to the effect of high-β low order mode lasing we employ a rate equation model that allows us to reproduce characteristic input-output curves of nanowire lasers and to extract the β factor of the device presented in chapter 4.
Furthermore, the rate equation model presented in this section provides valuable insights into the photon and carrier dynamics of the nanowire laser and allows interpretations of the spectral characteristics of the presented device.
However, a quantitative analysis of experimental data using a rate equation model requires detailed information about the optical properties of the device. The calculations presented in this section are performed using the parameters for nanowire lasers on Silicon, as presented in Chapter 4. In order to obtain important parameters such as the group velocity (n_{group}), the confinement factor (Γ) and the reflectivities of optical modes inside the nanowire (R), we simulate light propagation and confinement inside

the nanowire using Finite Difference Tim Domain (FDTD) methods.

2.3.1 Rate equation model of nanowire lasers on silicon

This section presents a rate equation model to calculate the dynamics of the carrier density $N(t)$ in the gain material and the number of photons $S(t)$ in a single optical mode of the core-shell nanowire [89][31]. The two corresponding coupled differential equations are given by

$$\frac{dN(t)}{dt} = \frac{P(t)}{h\nu} - \frac{N(t)}{\tau_{SRH}} - \frac{N(t)}{\tau_{spon}} - C \times N(t)^3 - \frac{c}{n_{group}} g(h\nu, N(t)) \times S(t) \tag{2.5}$$

$$\frac{dS(t)}{dt} = \Gamma \times \frac{c}{n_{group}} \times (g(h\nu, N(t)) - g_{th}) \times S(t) - \Gamma \times \beta \times \frac{N(t)}{\tau_{spon}} \tag{2.6}$$

, where $P(t)$ represents the carrier density generated by the pump source, $h\nu$ being the photon energy, τ_{SRH} being the decay time caused by Shockley-Reed-Hall recombinations, τ_{SRH} being the non-radiative lifetime caused by Shockley-Reed-Hall recombinations, τ_{spon} being the spontaneous emission lifetime, C being the Auger recombination constant, $g(h\nu, N(t))$ being the material gain, g_{th} being the threshold gain, $Gamma$ being the confinement factor and n_{group} being the group refractive index of the optical mode. Most parameters are taken either from the literature, from the separate FDTD calculations as presented in the previous section, or directly from the experiment. Corresponding parameters for a nanowire laser on silicon will be presented in chapter 4. The spontaneous emission coupling factor β is used as fit parameter to determine the fraction of the total spontaneous emission that is coupled into the laser mode, and the jump from below to above threshold in the input/output curve , as discussed in chapter 4. The excitation pulse that provides the initial carrier density is modeled as

$$P(t) = D \times \Big(\frac{1}{\tau_{exc}}\Big) \times sech\Big(1.76 \times \frac{t}{\tau_{exc}}\Big), \tag{2.7}$$

where τ_{exc} is the experimental pulse duration as determined from autocorrelation measurements of the excitation pulse. A constant factor D is used to match the theoretical to the experimental threshold in the resulting input-output curves. The dynamics described by the rate equations 2.6 is determined by the balance of gain and loss processes in the nanowire. We determine the gain for bulk GaAs at the waveguide mode energy $\hbar\mu$ in the quasi-equilibrium approximation by evaluating

$$\begin{aligned} g(h\nu, N(t)) = \frac{\pi e^2}{3\epsilon_0 n_{refr} m_0 c h^2} \times \Big(\frac{2}{\frac{1}{m_e} + \frac{1}{m_h}}\Big)^{\frac{3}{2}} \times \frac{E_k}{h\nu} \\ \times \int dE \sqrt{E - E_g} \times [f_c(E, N(t), T) - f_v(E, N(t), T)] \Phi(E - h\nu) \end{aligned} \tag{2.8}$$

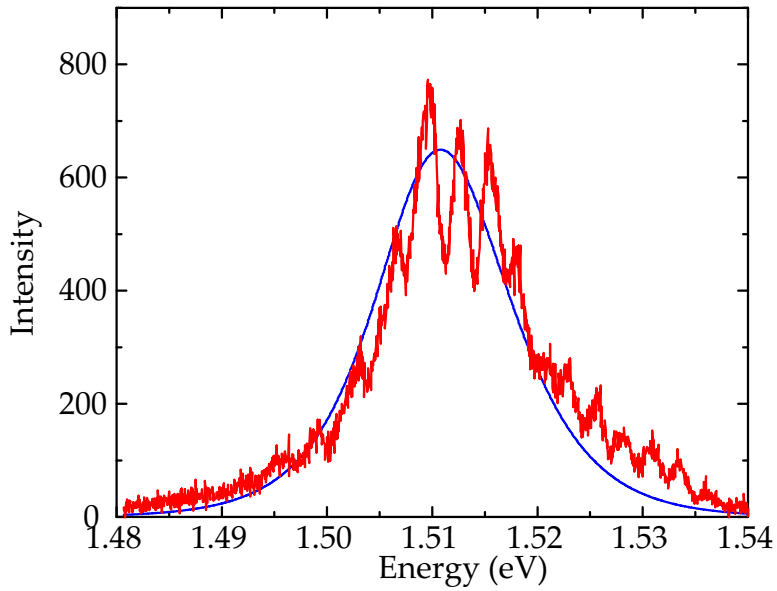

Figure 2.7. *Measured spontaneous emission a nanowire laser on silicon, as discussed in chapter 4. The spontaneous emission was measured at 0.5 P/P_{th} excitation power (red curve) and was fitted (blue curve) using equation 2.10 with the parameters given in chapter 4 table 4.3 and a carrier density of $1\times10^{16}/cm^3$.*

in each time step, assuming Fermi-distributions $f_{(c/v)}$ for electrons in the conduction and valence band at the current carrier density $N(t)$ [89]. For the line-shape function

$$\Phi(E-h\nu) = \frac{2\tau_{eh}}{h} sech\Big(\frac{2\pi(E-h\nu)\tau_{eh}}{h}\Big) \tag{2.9}$$

that appears in equation 2.8, we use the suggested sech-expression [89]. The time constant τ_{eh} is related to the dephasing time T_2 and is determined by fitting the theoretical spontaneous emission profile

$$r_{sp}(h\nu) = A\int dE\rho_r(E)f_c(E)(1-f_v(E))\Phi(E-h\nu) \tag{2.10}$$

to the measured one. A constant prefactor A accounts for the offset between the intensity in arbitrary units from our experiment to the numerical result. ρ_r(E) is the reduced density of states for bulk.

The best fit of equation 2.10 to the experimental data is shown by the blue curve in Fig. 2.7. The resulting parameters of the fit for the electron temperature T, the temperature dependent Bandgap (Varshni) function, and the dephasing time T_2 are given together with constants used to model the spontaneous emission curve in chapter 4 table 4.3. Using the parameters obtained from the fit to the spontaneous emission shown in Fig. 2.7, the optical gain can be calculated for different photon energies. The resulting gain as a function of photon energy is plotted for different carrier densities in Fig. 2.8.

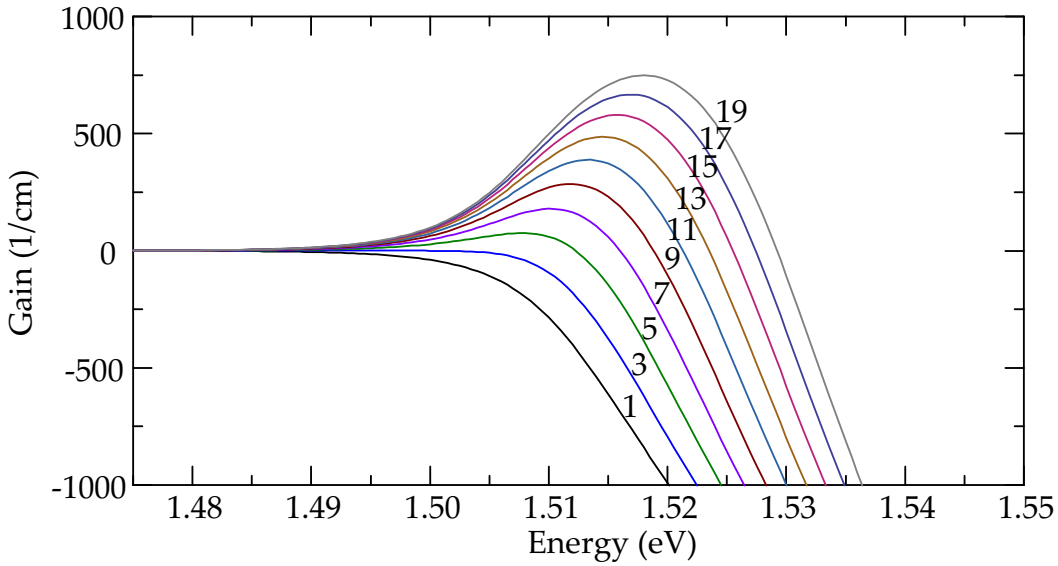

Figure 2.8. *Gain as a function of photon energy for carrier densities ranging from $1\times10^{16}/cm^3$ to $19\times10^{16}/cm^3$ calculated from 2.8.*

2.4 Spectroscopy of GaAs-AlGaAs nanowire-lasers

In order to characterize the optical response of individual nanowires we performed micro photoluminescence (PL) spectroscopy. Figure 2.9 shows a schematic illustration of the optical setup used for the characterisation of the GaAs/AlGaAs nanowire lasers. The optical excitation was performed using a Ti:Sapphire laser tuned to 780nm that provides $\sim$150fs duration pulses at a repetition frequency of 82MHz. The excitation path (blue line) is guided from the excitation laser through a cylindrical lens which allows to extend the optical beam along the nanowire axes, and therefore, enables optical pumping of the entire nanowire gain medium. After the cylindrical lens, the pump laser path is guided through a $\lambda/2$ plate and a polarizer that allows to align the polarization of the excitation along the nanowire axes which optimized the nanowire excitation. Afterwards, the excitation beam passes an optical beamsplitter (90:10) to separate the excitation path from the detection path shown in red. After the beamsplitter, the excitation laser passes a movable mirror and two lenses that are aligned in a 4-F geometry which enables individual positioning of the excitation spot on the sample. A detailed decription of the 4F geometry is presented in the next paragraph. The excitation laser is focused onto the sample using a $\times100$ microscope objective (NA$\sim$0.6) that provides diffraction limited performance and a minimum spot diameter of $\sim1\mu$m. The sample is placed inside a He-flow cryostat that allows measurement temperatures ranging from 4K to larger than room temperature. The coarse positioning of the sample is performed using a micro-screw stage which allows to move the cryostat with the sample in the x-y plane. The microscope objective can be moved by a piezo in x-y-z direction which enables to

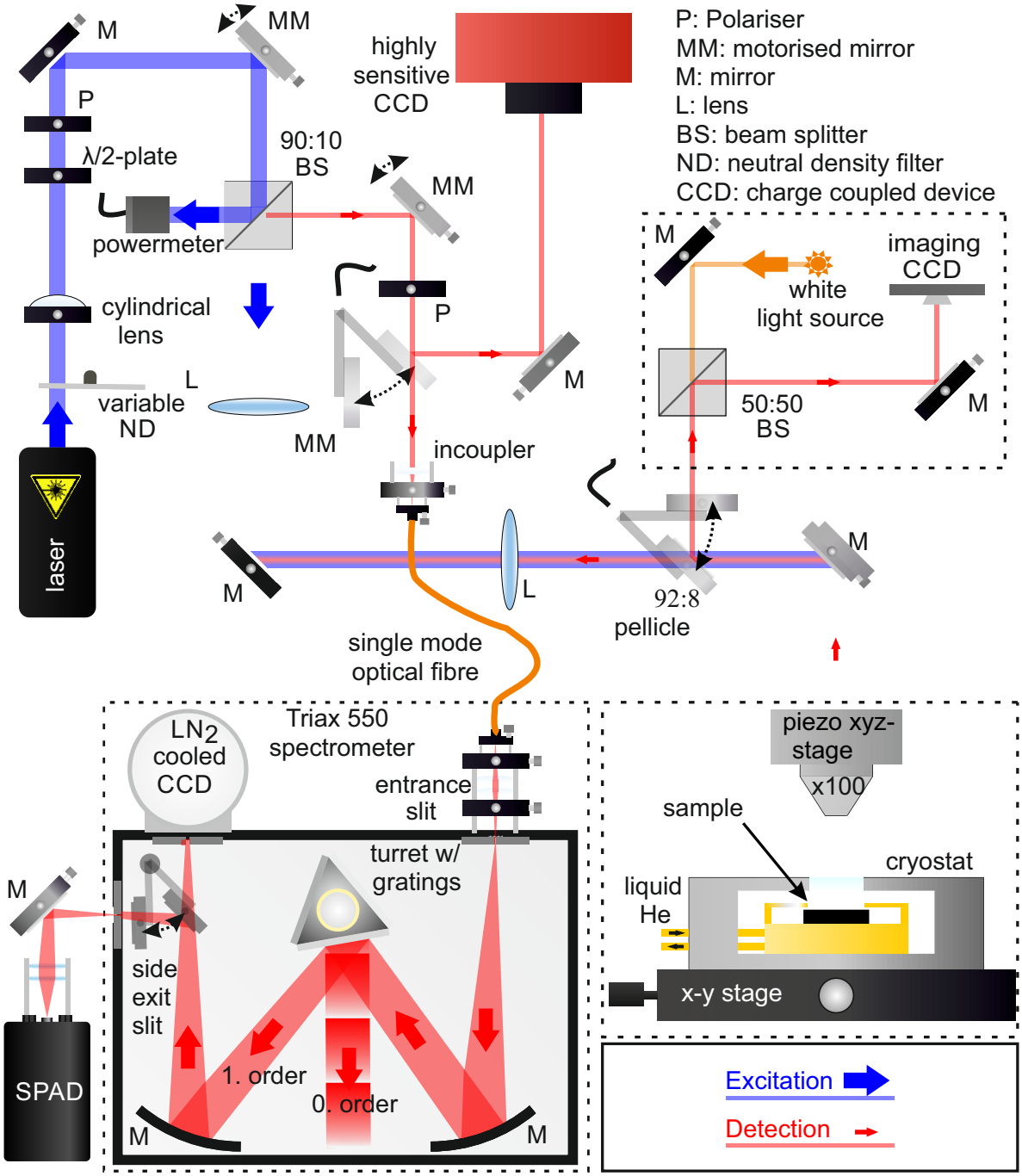

Figure 2.9. *Schematic representation of the optical setup used for the nanowire laser characterisation. The optical setup consists of an excitation path (blue), a detection path (red), an imaging system (top right), a path to record images of the nanowire luminescence with a highly sensitive CCD (top), a He flow cryostat where the sample is placed (bottom right) and an optical spectrometer for the spectral analysis of the nanowire emission.*

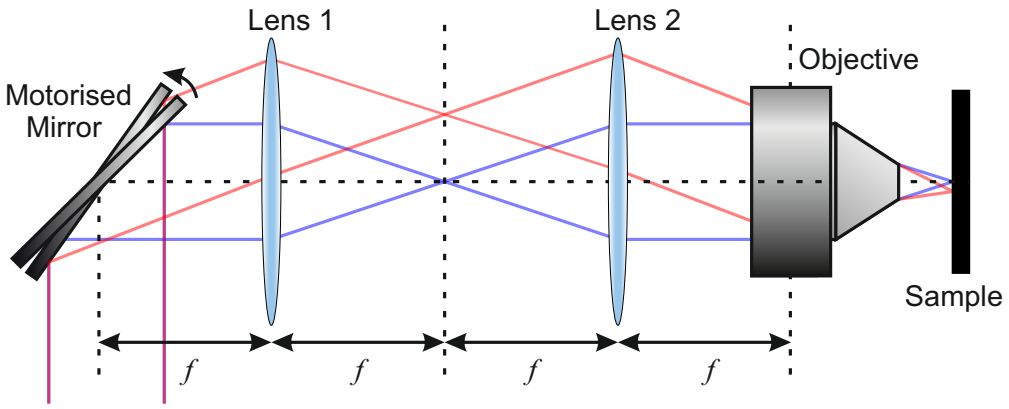

Figure 2.10. *Schematic representation of a 4F lens geometry. The first lens (left) is placed at a distance of 1×F away from a movable mirror. A second lens is placed 2×F away from the first lens and 1×F away from the objective. The two optical path (red and blue) enter the first lens in a different angle and enter the objective after the distance of 4×F. The two different optical path are focused on different positions in the focal plane of the objective.*

adjust the focus and provides additional control of the position of the excitation and the detection spot. The detection path can be again controlled individually using a movable mirror and the 4-F lenses. After the signal has passed the beamsplitter, the signal can either be coupled into a single mode optical fiber or focused onto a highly sensitive CCD camera chip. A movable mirror is used to guide the detection signal either to the CCD camera or pass it on to the optical fiber. After the signal is coupled to the optical fiber, the light is guided to the spectrometer where it is focused by two lenses onto the spectrometer entrance slit. Inside the spectrometer, the signal is diffracted by an optical grating and finally focused onto a CCD camera. Alternatively, a flipable mirror inside the spectrometer can be used to guide the diffracted signal beam onto a spectrometer exit slit which can be used for a spectral selection of the detected signal. Behind the exit slit, the signal can be detected using a single photon avalanche detector (SPAD) which was used for measurements of the carrier recombination rate of the GaAs/AlGaAs nanowire lasers. In order to image the sample, a white light source was focused onto the sample surface via another beamsplitter (50:50) which enables the reflected light to be detected using a CCD camera. The excitation (white light) and detection paths of the imaging pass a movable pellicle (92:8) that either enables to monitor the excitation spot together with the sample or can be flipped out of the signal-detection and laser-excitation path to maximize their intensity. Figure 2.10 shows a schematic illustration of the 4F lens geometry that is used to individually position the excitation and detection spot on the sample. A motorized mirror is used to change the angle of incidence with which light beams enter a first lens placed at a distance of 1×F away from the mirror. The red and blue lines illustrate two different optical beams that enter the first lens under two different angles. After both optical beams are focused in the focal plane

of the first lens, they enter a second len that is placed 2×F away from the first. An objective is place in the focal plane 1×F away from the second entrance and collects both, the red and the green optical light beam, although they follow different paths between the objective and the lens. This ensures that light beams enter the aperture of the objective independent of their angle of incidence. The angels of incidence on the objective define the position of the excitation spot in the focal plane of the objective. Therefore, the excitation spot can be positioned on the sample by turning the motorized mirror while the 4F lens geometry ensures that the light paths enter the aperture of the objective. This can also be used for light beams leaving the objective in different angles, and therefore, from different positions of the sample. Here, the position of the motorized mirror defines from which position on the sample light is collected. Using two motorized mirrors, one for the excitation path and one for the detection path, as shown in figure 2.9, the position of the excitation spot and the detection spot can be controled individually. Therefore, the 4F setup allows optimal excitation such that homogeneous gain is achieved and nanowire emission can be detected as well from the nanowire center as from their end-facets. As depicted schematically in Fig. 2.11, the substrate containing well-dispersed nanowires was placed in a He-flow variable temperature cryostat and optically excited with light, linearly polarized along the nanowire-axis. By inserting an F = 1m focal length cylindrical lens into the excitation beam, the excitation channel produces an elliptical focus with a full width at half maximum along the major and minor axes of 5.3$\pm$0.2μm and 1.6$\pm$0.2μm, respectively (Fig. 2.11). Emission was also collected along a direction normal to the nanowire axis and focused into a single mode optical fiber that provides a detection spot size $\sim$1μm^2, which can be precisely scanned along the length of the nanowire.

2.5 Input-Output characteristics of transferred GaAs/AlGaAs core-shell nanowire lasers at 10K

In order to observe the transition from spontaneous emission to lasing operation from GaAs/AlGaAs core-shell nanowires, we perform measurements of their output characteristics as a function of the pumping power. Figure 2.12 shows a typical series of PL spectra recorded at 10K from a region close to one end of the nanowire as the average excitation power density used to excite the entire wire is increased from $\sim$0.4-5kWcm^{-2}. For the lowest excitation power density the emission spectrum consists of a relatively broad emission band extending from $\sim$1.46-1.51eV, the dominant emission appearing at $\sim$1.49eV, below the expected low temperature zincblende bandgap of GaAs at $\sim$1.515eV [90] [91]. The comparatively large bandwidth of the emission spectrum and the observed redshift of the peak emission most likely reflect the presence of twin defects in the GaAs nanowire core. Such twin defects lead to the formation of indirect excitons with holes confined in the twin plane and electrons in the surrounding zincblende phase [91] [92]

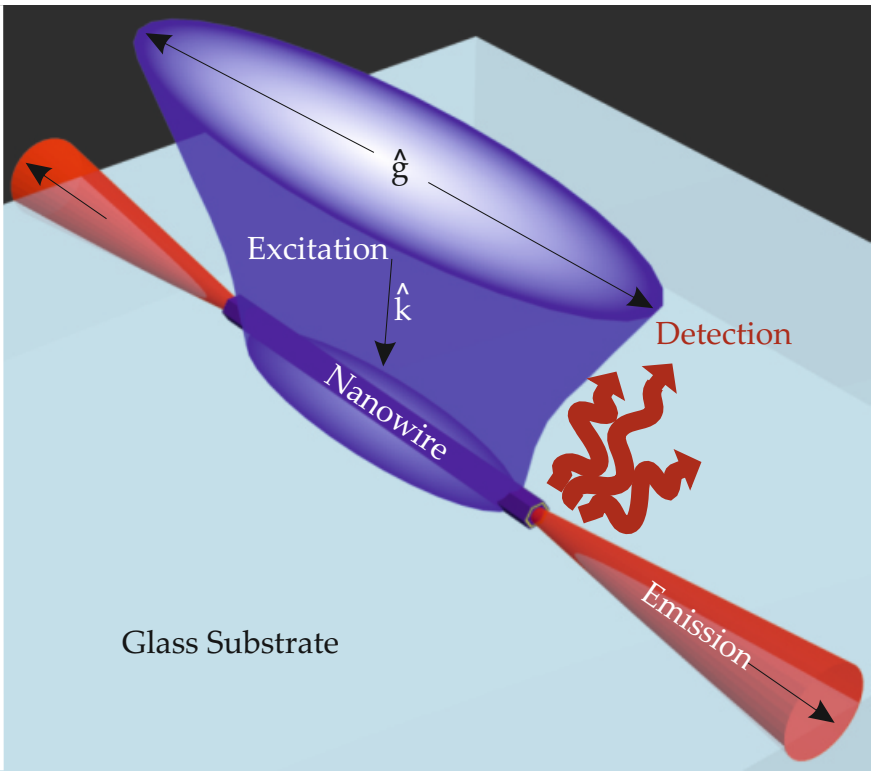

Figure 2.11. *Schematic representation of the measurement geometry on a single nanowire. The propagation direction of the incident excitation field ($\hat{\kappa}$) is perpendicular to the nanowire-axis and the linearly polarized excitation field is polarized in a direction ($\hat{\epsilon}$) parallel to the nanowire-axis to maximize the photoluminescence of the nanowire. Emission is detected with a ∼0.8µm spatial resolution along an axis parallel to -$\hat{\kappa}$.*

and give rise to an inhomogeneously broadened emission spectrum [93].
In addition, the periodic modulation of the spontaneous emission intensity is strongly apparent in Fig. 2.12 reflecting regularly spaced longitudinal FP-modes separated by 10±1meV. Calculating the cavity Q-factors of the nanowires from a typically measured linewidth of ∼3meV, the resulting Q-factors of Q∼300 correspond to a finesse of ∼2 and are in good agreement with the calculations presented in section 2.1 (Q∼750).
The spacing of these modes is expected to be $\delta E = (\hbar\pi c)/(n_{group} L)$, where $n_{group} = n_{eff} - \lambda (d_{neff} / d\lambda)$ is the group index of the axial guided mode [74] with an effective mode index n_{eff} and L is the nanowire length (see section 2.1). We measured L for all the nanowire lasers using optical microscopy and calculated the group indices n_{group} = 4.85 HE_{11}^{a} and HE_{11}^{b} guided modes respectively using numerical simulations as shown in section 2.1. Hence, the expected mode spacing between HE_{11}-like longitudinal FP modes of nanowire-A, measured to have a length of 10.2±0.8µm is 12.5±1meV, in close agreement with the measurements (Fig. 2.12).
As the excitation laser power density increases beyond ∼1.5kW/cm^2 a sudden and highly non-linear increase in the emission intensity is observed, with a pronounced

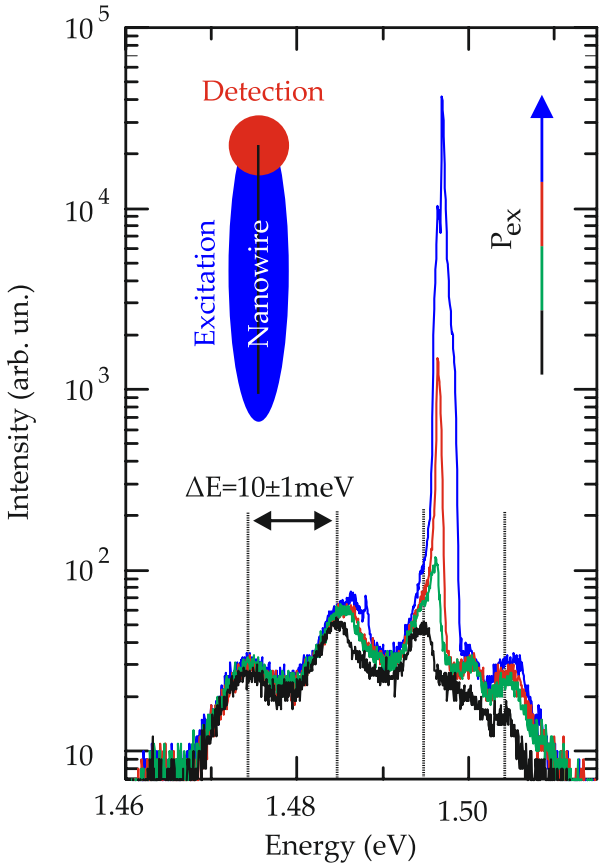

Figure 2.12. *Power dependent measurements at 10K (a) Power dependent spectra of the light recorded from the end of a single nanowire as a function of the mean excitation power density. The four curves plotted correspond to excitation power densities of ∼1.35, 1.9, 2.4 and 4.8. kWcm^{-2}. Note the logarithmic scaling of the intensity axis and the clear FP modulation of the spontaneous emission, with peaks separated by 10±1meV denoted by the vertical dashed lines. The inset shows a schematic depiction of the excitation and detection spots on the nanowire used to record the spectra.*

peak emerging close to ∼1.496eV that rapidly grows to become several orders of magnitude stronger than the spontaneous emission background. This is clear evidence of population inversion in the nanowire and amplified spontaneous emission from the end facets. The strongly super-linear increase of the peak emission with pump intensity is consistent with expectations when the laser threshold is approached [94] [95].

The peak intensity of the most intense PL feature is plotted in Fig. 2.13 as a function of the excitation power density, exhibiting a clear s-like dependence that is characteristic of the transition from spontaneous emission to amplified spontaneous emission, and finally to lasing [94]. Far above threshold, the output from the single mode at 1.496eV is several orders of magnitude stronger than the spontaneous emission background,

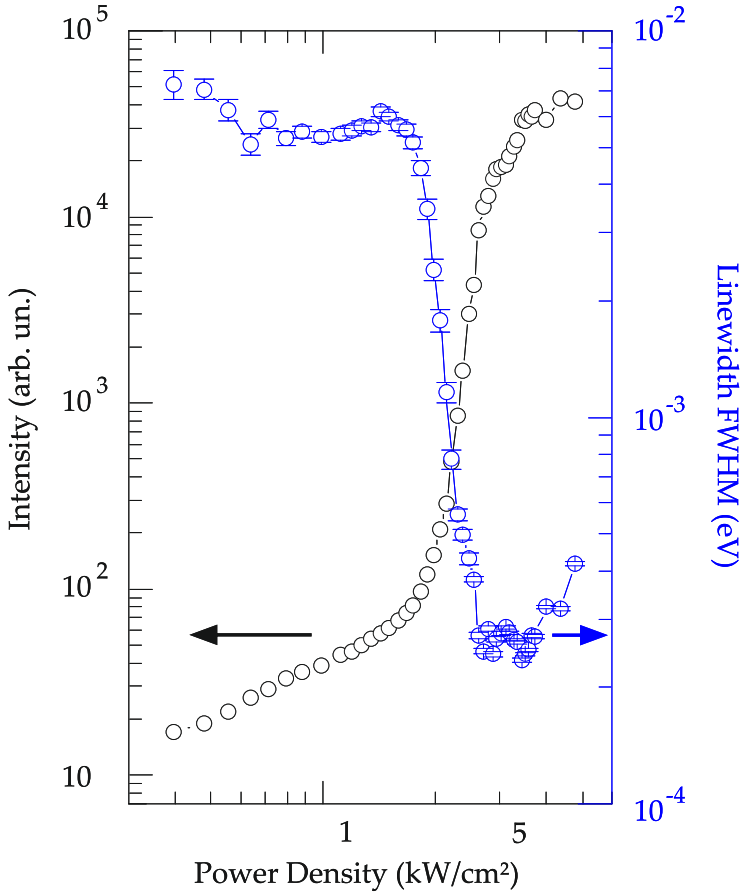

Figure 2.13. *Power dependence of the peak intensity within a ∼ 10meV wide spectral window centered around 1.495eV (black). The linewidth of the dominant emission feature is also plotted (blue).*

and evolves close to linearly with the pump power density as expected [②] . In contrast to previous studies of GaAs/GaAsP core-shell nanowires [72], strong gain pinning effects, indicative of local heating by the excitation laser are evident in the results of Ref. [72], where a transition to an output saturation was observed after only a modest (∼6 fold) enhancement of the emission intensity. In contrast, the results presented in Fig. 2.13 show that the laser output in our experiments increases by more than three orders of magnitude before a lasing regime is established. The results show that the high quality of the lattice matched GaAs/AlGaAs material system as demonstrated by the strong photoluminescence enhancement presented in Fig. 2.13 [67] efficiently suppresses non-radiative surface recombinations for lasing operation of the nanowire. In addition, the high confinement factor Γ>1 of low order waveguide modes enhances

[②] The absence of steady state conditions in the pulsed nanowire laser and Fourier limitations of the spectral linewidth of the emission can lead to deviations from a perfectly linear Input/Output characteristic of the laser peak intensity.

light matter interactions inside the GaAs gain medium as shown Fig. 2.5. This enables, together with the optical feedback provided by the nanowire cavity (Q∼300), stimulated emission to become the dominant radiation mechanism of optically pumped GaAs/AlGaAs nanowire lasers. As such, the results presented in Fig. 2.12 and Fig. 2.13 are characteristic of the intrinsic levels of performance that are attainable using GaAs/AlGaAs nanowire lasers.
The linewidth of the pre-dominant luminescence line is also shown by the blue data points in Fig. 2.13. It reduces from ∼6meV for P < 1kWcm^{-2} to close to the resolution limit of our spectrometer (∼0.1meV) for P > 1.5kWcm^{-2}. The observation of the threshold behavior, highly non-linear input-output characteristics and pronounced linewidth narrowing are strong evidence of lasing in the GaAs-AlGaAs core-shell nanowire, with a threshold power density of P_{th} = 2.40±0.45kWcm^{-2} for this particular nanowire.
Interestingly, the nanowire linewidth increases again for very high excitation powers. This is in strong contrast to the reduction of the linewidth with increasing power expected from the Schawlow-Townes Formula [96] for the laser linewidth $\Delta\omega_{osc}$:

$$\Delta\omega_{osc} = \frac{N_2}{N_2 - N_1} \times \frac{\pi\hbar \times \omega \times \Delta\omega_c^2}{P_{osc}} \tag{2.11}$$

, with ω_C being the cold cavity bandwidth, P_{osc} being the power level in the oscillator and ω being the laser frequency [96]. The excess noise factor $\frac{N_2}{N_2-N_1}$ [96] is determined by the population of the excited state (N_2) and the population of the ground state (N_1). Deviations from the Schawlow-Townes-Limit in semiconductor lasers can be typically attributed to variations of the real refractive index of the gain material with carrier density and spontaneous emission induced phase and intensity changes in the laser field [97]. However, the increase of the nanowire laser linewidth observed for high excitation powers can be attributed to the Fourier limitation of the ultrafast nanowire laser pulse emission. This will be discussed in detail in section 4.7, where experimental data are compared with calculations from a rate equation model. Other theoretical calculations performed by Kathy Lüdge and ultrafast pump-probe measurements of a GaAs/AlGaAs nanowire laser as presented in section 5.5 and 5.6., also reveal that the small features observed within the homogeneously broadened nanowire linewidth can be attributed to Rabi oscillations caused by coherent light matter interactions inside the nanowire.

2.6 Carrier recombination rate in optically pumped GaAs/AlGaAs nanowire lasers

Further evidence for the lasing operation of the GaAs/AlGaAs nanowire lasers can be obtainted by measurements of the carrier recombination rate γ_c=1/τ_c, with τ_c being the carrier lifetime. The total recombination rate is given by the sum of the radiative

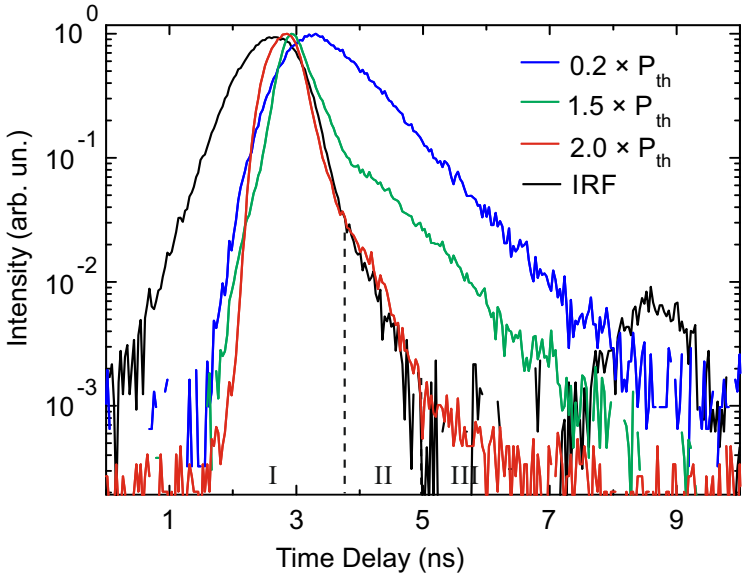

Figure 2.14. *Time dependent photoluminescence measurements of a nanowire laser subject to different excitation powers of 0.2×P/P$_{th}$(blue), 1.5×P/P$_{th}$(green) and 2×P/P$_{th}$(red). The black curve shows the instrument response function (IRF). The output photoluminescence intensity is recorded from a lasing peak at 1.496eV, normalized and plotted on a semi-logarithmic scale.*

recombination rate γ_R=1/τ_R and the non-radiative recombination rate $\gamma_N R$=1/$\tau_N R$:

$$1/\tau_c = 1/\tau_R + 1/\tau_N R \tag{2.12}$$

Radiative recombination in GaAs/AlGaAs nanowire lasers are either caused by stimulated or spontaneous emission processes, whereas non-radiative processes are attributed to Schockley-Reed-Hall (SRH) and Auger recombinations. The combined recombination lifetime τ_c can be measured using a setup for time resolved photoluminescence measurements as presented in section 2.4 in Fig. 2.9. In order to determine the time-dependent emission characteristics of a nanowire laser, we used the time delay between an electronic trigger signal from the mode-locked Ti:Sa laser indicating when an excitation pulse is emitted and a single photon avalanche detector indicating when the nanowire luminescence signal arrived at the detector. We measure the integrated intensity of a nanowire laser emission line at 1.496eV at 10K for different time delays between the SPAD and the excitation laser signal. The instrument response function (IRF, black curve) was recorded by measuring the time dependent response of the SPAD and the measurement electronics subject to pulses from the Ti:Sa excitation laser. Typical results of the carrier lifetime in a nanowire laser are presented for three different excitation powers of P/P_th=0.2 (blue), P/P_th=1.5 (green) and P/P_th=2 (red) in Fig. 2.14. After the peak intensity is reached, the blue curve clearly exhibits a mono-exponential decrease

of the photoluminescence intensity. The characteristic decay time of τ_c was obtained by deconvoluting the measured time-dependent spontaneous emission signal of the nanowire (green curve) with the IRF (black curve). The result of τ_c=680ps is in very good agreement with the findings of from Saxena et al. [98] that found a room-temperature carrier lifetime of 0.44ns for weakly pumped GaAs/AlGaAs nanowires. In contrast, for strong excitation powers of P=2$\times$P$_{th}$, we observe a strong reduction of the photoluminescence lifetime (red curve, region I). As the decay slope of the IRF is very similar to the measured radiative decay of the carrier lifetime in the nanowire we conclude that the measured signal is resolution limited, and, therefore, faster than $\sim 250ps$. The steep decay of the nanowire photoluminescence at high excitation powers is attributed to dominant stimulated emission and provides a clear evidence for the lasing operation of the nanowire with laser pulse durations <250ps. In order to overcome the temporal resolution limit, we perform ultrafast pump-probe spectroscopy of the nanowire lasers as presented in chapter 5, showing indeed ultrafast nanowire pulse emission with pulse durations <10ps. Interestingly, after the lasing regime (regime I), the nanowire decay exhibits a reduced decay time as other decay channels such as non-radiative (SRH) and spontaneous emission processes can contribute to the depopulation of the lasing state. We attribute this decay (regime II) to amplified spontaneous emission where stimulated emission, non-radiative processes and spontaneous emission contribute to the depopulation of excited states in the nanowire [31]. Furthermore, at short times after the peak intensity ($\sim$0.7ns), the green curve exhibits an intermediate decay (regime II) between the resolution limited lasing regime (regime I) and the regime where spontaneous emission and non-radiative recombinations can dominate (regime III, τ_c=0.68ns). We conclude that at intermediate carrier densities in the nanowire after the lasing regime and at excitation powers close above threshold (ASE regime), the radiative lifetime can be determined by stimulated emission but also spontaneous emission and SRH recombinations that increase τ_c to τ_c>250ps. In contrast, at times >$\sim$2ns after the peak intensity (region III), the population of excited states in the nanowire is reduced below transparency and, consequently, all curves exhibit a similar exponential decay as found for the weakly pumped system (blue curve on Fig. 2.14, τ_c=0.68ns).

2.7 Estimation of the carrier concentration close to threshold

The 4F setup presented in section 2.3 allows not only to detect the transition from spontaneous emission to lasing at the end facets of the nanowires, but also to observe the residual spontaneous emission of the nanowires in the lasing regime radiated from the nanowire center. The spectra recorded during lasing operation from the center of the nanowires provide informations about the carrier concentrations and carrier temperatures.
Figure 2.15a) shows a charged-coupled device (CCD) image of the emission of another

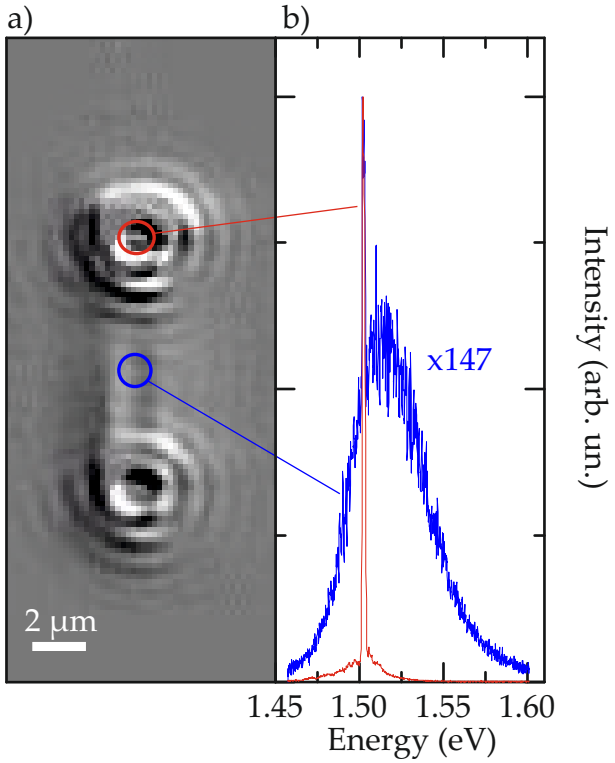

Figure 2.15. *Spatially resolved measurements at 10K (a) Image of the nanowire emission recorded at ∼1.5×$P_{threshold}$ showing clear interference fringes around the nanowire end facets and much weaker, spectrally broad spontaneous emission from the body of the nanowire, extending up to ∼1.60eV. The scale bar is 2μm. (b) Comparison of the stimulated and spontaneous emission spectra from the nanowire excited under the same conditions depicted in (a).*

nanowire from the same batch with a similar behaviour, pumped above threshold (∼ 1.5×P_{th}) at 10K. As shown in Fig. 2.15b), the PL spectra recorded from the middle (blue) and one end of the nanowire (red) are entirely different. Whilst very strong and spectrally narrow emission is observed at the nanowire end facet owing to scattering of laser emission into our detection system, much broader and weaker emission is recorded from the midpoint of the nanowire. This stems from the weak residual spontaneous emission from the excited nanowire and provides direct information about the excitation level of the gain material in the lasing regime. The high-energy tail of the spontaneous emission recorded from the nanowire mid-point as shown in Fig. 2.15b) extends up to ∼1.60eV and is indicative of significant band filling effects at high excitation levels. To estimate the carrier density close to threshold we fitted the spontaneous emission spectrum using a simple model which assumes that the electronic structure of the GaAs core can be described by 3D, isotropic parabolic bands with effective masses m_e^* = 0.063, m_{HH}^* = 0.5l and m_{LH}^* = 0.08 and that the interband matrix element for optical transitions is constant, independent of energy. Using these approximations the form

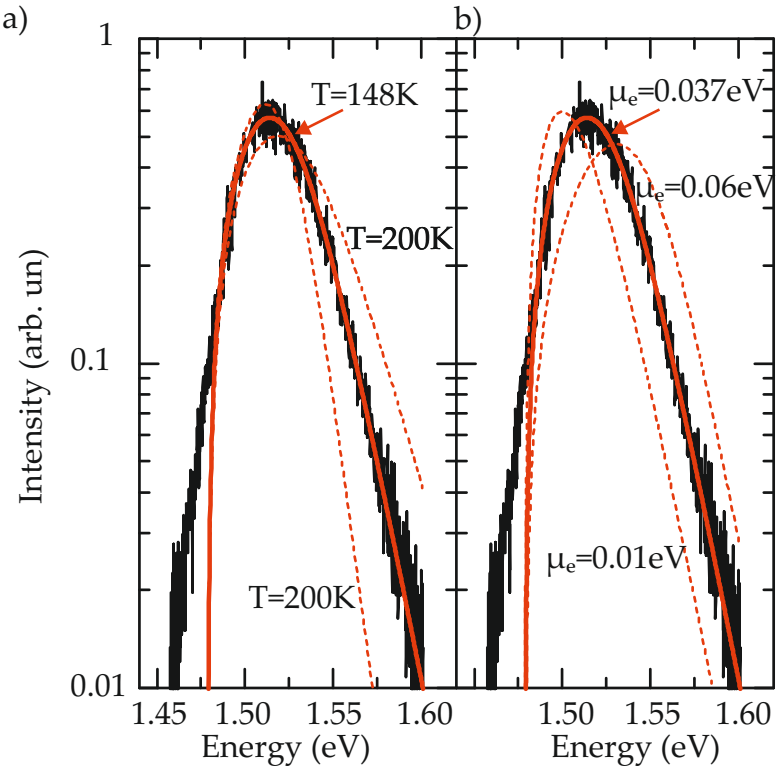

Figure 2.16. *Residual spontaneous emission from the nanowire center close to threshold and the fitting curves used for the estimation of the carrier density Example showing the fit of the high-energy tail of the spontaneous emission from Fig. 2.15 using equation 2.17. The red curve shows the best fit obtained by minimizing the sum of the squares of the residuals. (a) The dashed red lines show the influence of fixing the carrier density and varying the electron temperature. (b) The dashed lines show the impact of fixing the carrier temperature and varying the position of the electron quasi Fermi level.*

of the PL spectrum can be reconstructed by populating the conduction and valence bands, according to their density of states multiplied by the Fermi distribution functions. The excitation level and, thereby, the carrier density controls the relative position of the electron and hole quasi Fermi levels and, therefore, a fit to the spontaneous emission spectrum (blue) as depicted in Fig. 2.15b) provides information on the carrier density and carrier temperature.

The high-energy tail of the spontaneous emission spectrum shown on a log scale in Fig. 2.16 reflects the energetic distributions of electrons in the conduction band and holes in the valence band in the highly excited nanowire. This is determined by the level of excitation in the nanowire-core (i.e. the separation of the electron-μ_e and hole-μ_h quasi Fermi levels) and the band densities of states (i.e. $D_{e/h}$ ($E_{e/h}$)$\propto m_{e/h}^{3/2}\sqrt{E_{e/h}}$ assuming isotropic 3D parabolic bands). From the assumption that the photon emission stems

solely from vertical electrons transitions in k-space follows the relation

$$m_e^* \times E_e = m_h^* \times E_h \tag{2.13}$$

, with E_e being the energy separation between the electron in the conduction band and the conduction band-edge, E_h being the energy separation between the hole in the valence band and the valence band-edge, and m_e^* and m_e^* being the carrier effective masses. Therefore, the photon energy E_{ph} can be written as:

$$E_{ph} = E_g + E_e + E_h \tag{2.14}$$

where E_g is the bandgap of the semiconductor. Substituting E_e or E_h into equation 2.14 and using equation 2.13 we can express E_e and E_h as:

$$E_{e/h} = \frac{E_{ph} - E_g}{1 + \frac{m_{e/h}^*}{m_{h/e}^*}} \tag{2.15}$$

We model the photon intensity I(E_{ph}) to be

$$I(E_{ph}) \propto D_e(E_e) f_e(E_e) \times D_h(E_e) f_h(E_e) \tag{2.16}$$

with $f_e(E)$ and $f_h(E)$ being the Fermi function in the conduction and in the valence bands, respectively. This results in a spectral emission profile of the form

$$\begin{aligned} I(E_{ph}) = A \times \frac{(E_{ph} - E_g)(m_h m_e)^2}{m_h + m_e} \left(exp\left(\frac{1}{k_b T} \left(\frac{E_{ph} - E_g}{1 + \frac{m_e}{m_h}} - \mu_e \right) \right) + 1 \right)^{-1} \\ \times \left(exp\left(\frac{1}{k_b T} \left(\frac{E_{ph} - E_g}{1 + \frac{m_h}{m_e}} - \mu_h \right) \right) + 1 \right)^{-1}, \end{aligned} \tag{2.17}$$

, where A is an arbitrary constant. Due to the much lower effective mass of the conduction and heavy hole bands (m_e^* ∼0.068 and m_{hh}^* ∼0.51), the form of the high-energy tail of the PL spectrum is dominated by the form of the electron distribution in the conduction band. Subject to these approximations, we fit the model to the form of the PL spectrum which provides the position of the electron and hole quasi Fermi levels and the carrier temperature (T). Figure 2.16 shows typical results obtained using this procedure. Once the parameters μ_e, μ_h and T have been obtained, the carrier densities can be extracted using

$$n = \int_0^\infty D_e(E) \times \left(exp\left(\frac{E_{ph} - E_g - \mu_e}{k_b T} \right) + 1 \right)^{-1} dE, \tag{2.18}$$

for the electron density

$$p = \int_0^\infty D_h(E) \times \left(exp\left(\frac{E_{ph} - E_g - \mu_h}{k_b T} \right) + 1 \right)^{-1} dE, \tag{2.19}$$

for the holes [89].

The requirement that n = p (charge neutrality) provides an internal consistency check that is used to check the validity of our approach.

The dependence of the obtained fit curve on parameter variations (dashed lines) from the best fit curve (solid line) are presented in Fig. 2.16a) and b) for the best-fit quasi Fermi level and 3 different temperatures and for the best-fit temperature and 3 different quasi fermi levels, respectively. Typical results of the fitting procedure provide an electron temperature in the range ∼130-170K with a carrier density in the range ∼8-12$\times 10^{17}$cm^{-3}. This range of carrier densities is in good agreement with theoretical predictions of Ref. [62], where the transparency carrier density for similar nanostructures is calculated to be 4.62$\times 10^1$7/cm^3 at ∼100K. This observation further supports our conclusion that we indeed observe lasing from our nanowire structures.

2.8 Comparison of different nanowire lasers

The fabrication of the nanowire lasers as described in section 2.2 may cause imperfections in the quality of the devices. As a result of the random growth of the nanowire lasers presented in this chapter, large differences between the nanowire geometries and material qualities are expected. Furthermore, the mechanical removal of the nanowires from the growth substrate and transfer of the nanowires to a low refractive index (SiO_2) substrate causes variations in the quality of the nanowire end-facets, and therefore, their lasing thresholds. These imperfections lead to a variation of the nanowire laser performance that we investigate by comparing the optical characteristics of different GaAs nanowire lasers.

By comparing the emission properties of various transferred nanowires, we found that about 80% of all investigated nanowires exhibit the characteristic of a lasing threshold as described above. Figure 2.17 compares spectra recorded at 10K from three different nanowires, labelled nanowire-A, -B and -C having lengths of 10.2$\pm$0.8μm, 11.4$\pm$0.8μm, and 10.9$\pm$0.8μm, respectively. For each nanowire, data is presented in Fig. 2.17a) with excitation power densities below and above threshold, as denoted by the filled blue and red symbols on Fig. 2.17b). Below threshold, the emission of each nanowire exhibits the characteristic periodic modulation that evolves with pump power into single mode lasing for nanowire-A and -B and two-mode lasing for nanowire-C.
Interestingly, several longitudinal FP modes are observed in the emission spectrum below threshold. For some nanowires (e.g. nanowire-A) a single series of longitudinal

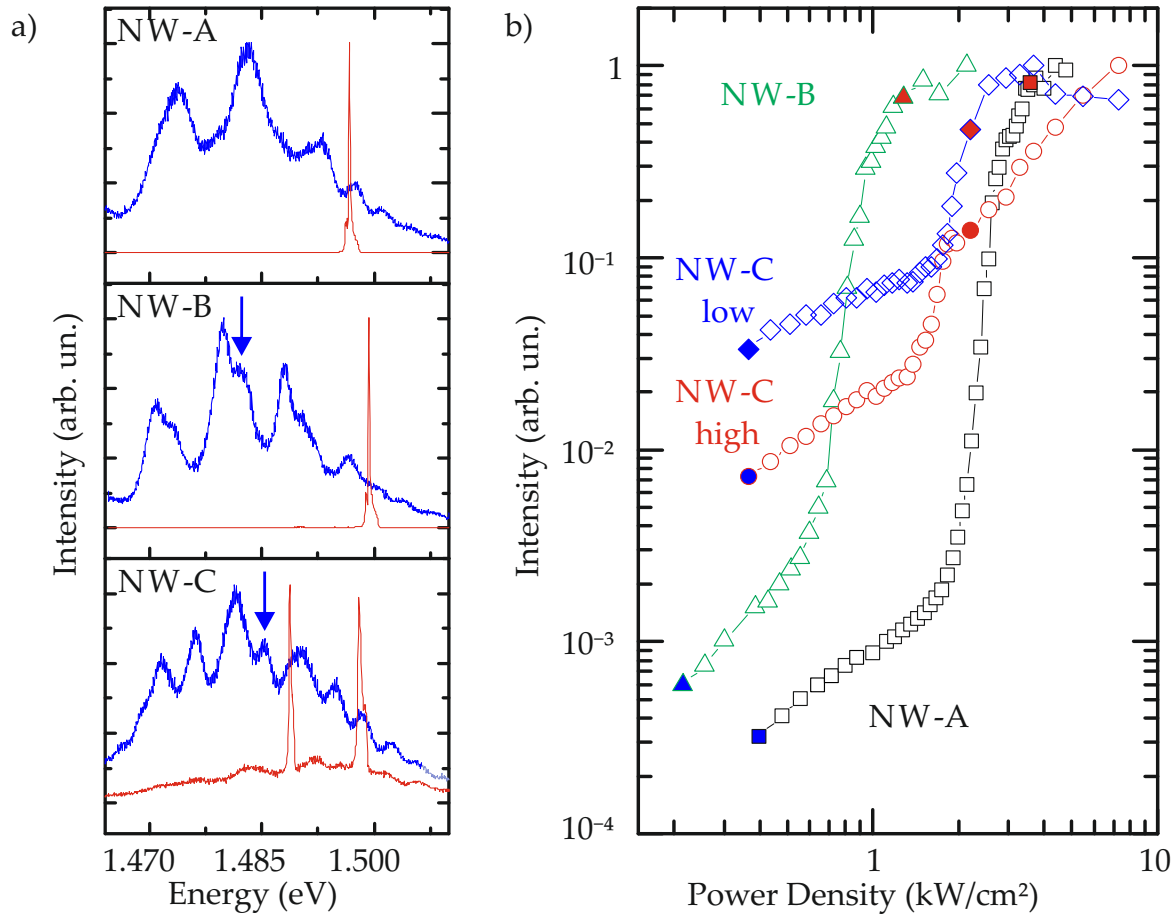

Figure 2.17. *Comparison of the lasing performance from different nanowires (a) Output spectra recorded from the end facets of three different nanowires with lengths of 10.2±0.8μm (nanowire-A), 11.4±0.8μm (nanowire-B) and 10.9±0.8μm (nanowire-C) with excitation powers below and above threshold, as marked on panel (b) by the filled symbols (intensities are normalized). Below threshold, the spontaneous emission is modulated by the FP-modes of the cavity. (b) Input-output characteristics of the three nanowires as a function of the excitation level, clearly showing the transition to lasing with thresholds at 2.40±0.45kWcm^{-2} (nanowire-A), 0.76±0.15kWcm^{-2} (nanowire-B) and 1.48±0.3kWcm^{-2} (nanowire-C) for the higher-energy lasing peak (nanowire-C), respectively.*

FP modes is observed whereas some nanowires (e.g. nanowire-B and nanowire-C) clearly exhibit two series of FP modes, as indicated by arrows in Fig. 2.17a). This reflects longitudinal modes of two principal transverse guided modes inside the nanowire waveguide that have a distinct group index. Any reduction of the hexagonal symmetry of the nanowire, e.g. arising from the fluctuating growth environment of specific nanowires, shadowing effects and growth competition or, also the shape of the nanowire end-facets determine the spectral resonances of guided modes which compete for gain. The strongest splitting of the FP-modes is observed in nanowire-C which finally results

in a bi-modal lasing. As shown in Fig. 2.17b, the slope of red data points (NW-C high) strongly decreases if the second lasing mode (NW-C low, blue data points) reaches the threshold. This represents a clear signature for modal competition: Stimulated emission into the second mode (NW-C low) depopulates excited states, and thus, reduces the number of excited carriers available for stimulated emission into the first mode (NW-C high). In contrast, nanowire-A and nanowire-B exhibit single mode operation over the entire range of pump levels investigated.
Figure 2.17b) shows the characteristic input-output characteristics of the three nanowires as a function of excitation level normalized to the intensities far above threshold. All three nanowires clearly show the transition from spontaneous emission to lasing with threshold power densities of $2.40\pm0.45\text{kWcm}^{-2}$ (nanowire-A), $0.76\pm0.15\text{kWcm}^{-2}$ (nanowire-B) and $1.48\pm0.3\text{kWcm}^{-2}$ (nanowire-C), respectively. The variations in threshold power densities are probably due to imperfections of the end facets, variations of crystal qualities or waveguide symmetries. Nanowire-B exhibits a remarkably low threshold power density of only $0.76\pm0.15\text{kWcm}^{-2}$, even lower than theoretical predictions [62], which demonstrates the high quality of the nanowire-laser structures fabricated.

2.9 Temperature dependence of nanowire laser input-output characteristics

We complete this chapter by presenting investigations of the influence of varying the lattice temperature on the nanowire laser emission. Typical results obtained are presented in Fig. 2.18 from nanowire-B, which exhibited the lowest threshold power. Figure 2.18a) shows normalised emission spectra recorded above threshold for various temperatures and Fig. 2.18b) presents the measured input-output characteristics at 10K and 285K.
Remarkably, clear lasing behaviour is observed up to room temperature. Figure 2.18a) compares normalised spectra recorded above threshold for lattice temperatures ranging from 10-285K. Laser operation is maintained up to room-temperature giving rise to the characteristic input-output curves as shown in Fig. 2.18b) that compares data obtained at 10K and 280K. We note that multimode lasing is observed for temperatures above 220K, indicative of a temperature-induced reduction of the peak gain [62] and broadening of the gain spectrum to a level comparable to the mode spacing.
As the lattice temperature varies, the dominant lasing energy depicted in Fig. 2.18a) red shifts from 1.50eV to 1.39eV, perfectly reflecting the expected bandgap reduction of the GaAs core presented in Fig. 2.19.

The peak positions of the lasing modes as a function of cryostat temperature depicted in Fig. 2.19 clearly adhere to expectations from an empirical Varshni fit for GaAs. The rigid red-shift observed between the peak positions of the lasing modes and the bulk GaAs data is due to the existence of twin defects [90] [91]. However, since the coefficients extracted from the Varshni fit are very close to expectations for GaAs (α=$5.1\pm0.8\times10^{-4}$

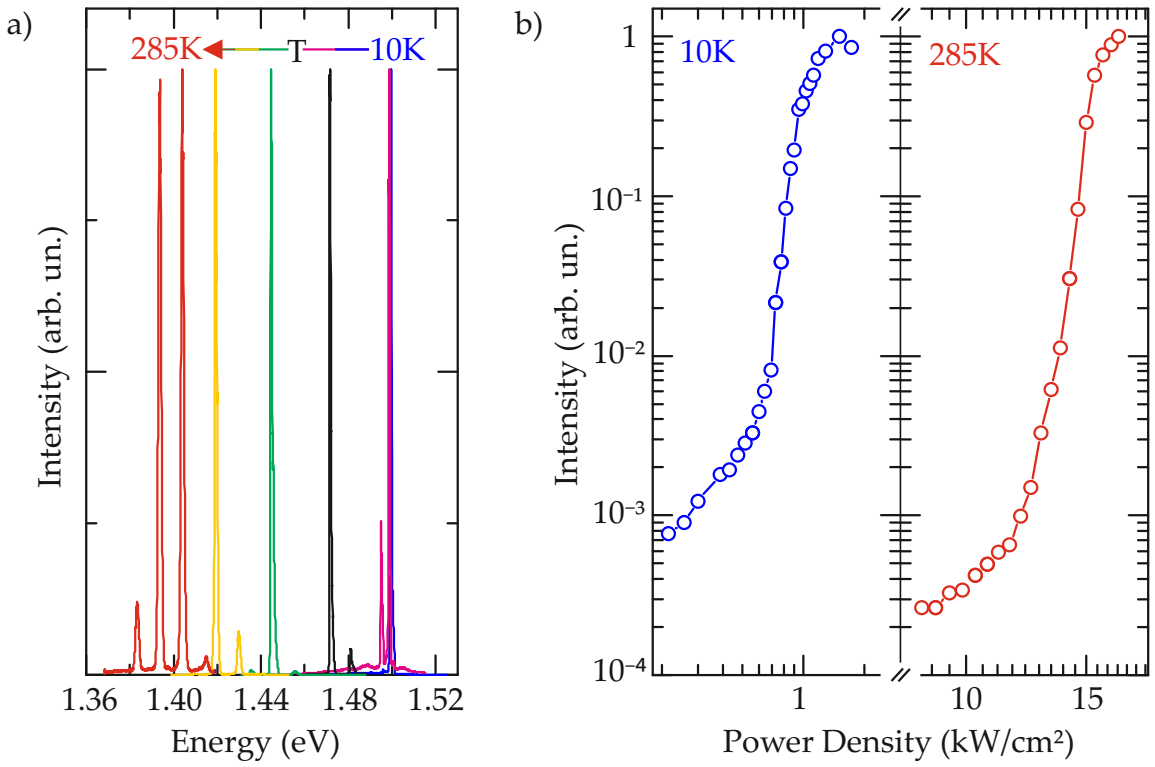

Figure 2.18. *Temperature dependent input-output characteristics (a) Temperature dependent emission spectra (normalized intensity) recorded from nanowire-B pumped above threshold for 10K, 50K, 110K, 170K, 220K and 285K. (b) Input-output characteristics measured at 10K (left panel, blue)and 285K (right panel, red) from the same nanowire.*

eV/K and β=84$\pm$56 K, c.f. 5.5 $\times 10^{-4}$ eV/K and 225 K for GaAs [99]). This observation indicates that the temperature dependence of the nanowire-laser emission energy is dominated by the bandgap reduction at higher lattice temperatures, and that the variation of the refractive index plays a comparatively minor role. Figure 2.20 shows that the laser threshold power density increases by a factor of $\sim$22$\times$ as the temperature is raised from 10K to 280K and how the pump power needed to exceed the threshold increases exponentially with temperature. This can be fitted by an exponential function describing the thermal broadening of the gain spectrum and we obtain a remarkably high characteristic temperature of T_0 = 109$\pm$12K for this nanowire-laser [100]. We conclude that laser heating has no crucial influence on the lattice temperature of the nanowire lasers and believe that these observations indicate that the cold-finger temperature corresponds very closely to the lattice temperature of the nanowires.
Interestingly, the high characteristic temperature of T_0 = 109$\pm$12K is comparable to conventional double heterostructure lasers of similar material systems [100] which further substantiates the strong potential of the nanowires for future devices such as integrated light sources on photonic microchips that operate at room-temperature. Vertical emission has been recently observed from InGaAs-GaAs nano-pillars grown on silicon

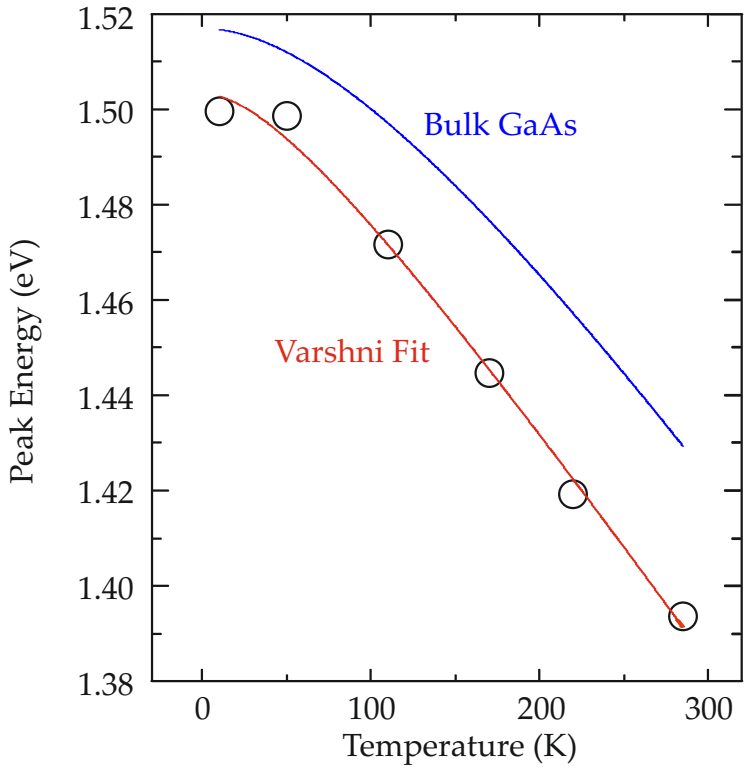

Figure 2.19. *Influence of the lattice temperature on the peak positions of the dominant lasing modes for different temperatures (black) fitted by a Varshni curve (red) and compared to the bandgap shrinkage shown by the Varshni dependence of GaAs (blue). Despite the constant offset which we attribute wurzite/zincblende segments in the nanowire [91], the similar temperature-dependence of both curves is a clear signature for a peak gain shift caused by the bandgap shrinkage of the nanowire material and the sufficient thermal anchoring of the nanowire lasers.*

[35] and silicon metal oxide semiconductor field-effect transistors [70] by exploiting low loss helically propagating modes for which the reflectivity of the nanowire-substrate is high, despite the low index contrast. Furthermore, AlGaAs-GaAs nanowire-lasers could be directly integrated into silicon and III-V photonic crystal nanostructures to facilitate highly directed vertical emission [101] or transferred onto photonic waveguides for use as integrated sources [102]. However, using III-V nanowires as an integrated source for applications such as silicon optical interconnects should take advantage of the ability to grow nanowires site selectively and, furthermore, the lasers should emit unidirectionally into the underlying silicon photonic hardware.
In this context, dielectric Bragg mirrors could be deposited on the as-grown nanowires to provide high mirror reflectivity at the upper nanowire facet and weaker reflectivity at the nanowire-substrate interface [103] by virtue of the weaker evanescent mode coupling. Such approaches would have significant promise since they may facilitate the realization of compact, nanowire-lasers epitaxially on silicon photonic nanostructures, without

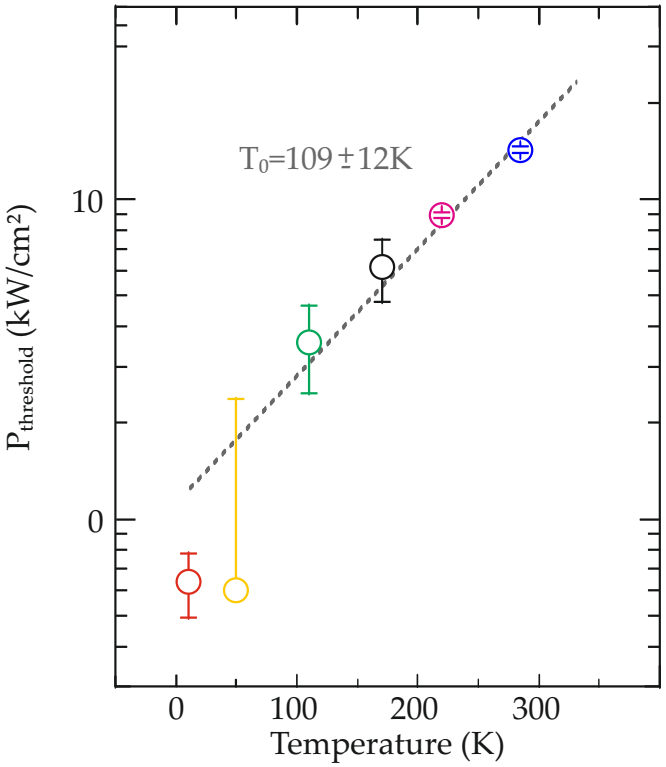

Figure 2.20. *Threshold pump power as a function of temperature revealing the characteristic temperature of T_0=109±12K. The threshold pump power was determined by a linear fit of the output intensity above threshold and extrapolating this curve to the x-axis. The intersection with the x-axis and the corresponding errors are used to determine the threshold pump power. The threshold pump power is plotted at 10K (blue), 50K (purple), 110K (black), 170K (green), 220K (yellow) and 285K (red).*

the need for complex wafer bonding techniques [104]. For such integrated photonics applications, we note that the emission wavelength must also be shifted further into the infrared, for example by replacing the GaAs core with InGaAs. Recently, promising first results have been obtained showing that InGaAs nanowires with very high uniformity can be grown site-selectively on Si and their composition can be tuned over large ranges [105]. This provides significant prospects to extend the emission wavelength into the telecommunications window and beyond for which nanowire lasing could be obtained providing that Auger losses, which are more significant at longer wavelengths, can be overcome.

Finally, electrical injection would be essential for nanowire-lasers operating in an integrated setting. To date, only a few works report lasing from electrically excited nanowires [52] [106]. However, radial p-n junctions in GaAs based nanowires are driven mostly by their potential for applications in nanowire-photovoltaics [107]. The availability of such materials provides much promise for the future development of electrically driven, compact III-V nanowire-laser sources grown site selectively on silicon photonic

hardware with the potential for nanowires to make a breakthrough in the development of optical interconnects.

2.10 Summary

In this chapter, we investigated detached GaAs-AlGaAs core-shell nanowire lasers in order to characterize and probe their intrinsic properties and performance. Our results showed that the AlGaAs shell inhibits non-radiative surface recombination such that clear near infrared lasing operation can be achieved up to room temperature. The highly non-linear input-output emission characteristics have strong potential for novel applications in which e.g. lasing is used to optically sense the local environment of the nanowire [75] or in the use of coupled cavity concepts for switching [108]. Although one can expect further improvements of the nanowire-laser performance by improving the end facet reflectivity via chemical polishing or by placing them onto patterned substrates for which distributed feedback concepts can be exploited [109]. However, the direct integration of III-V nanowire-lasers onto silicon substrates for integrated photonics and optical interconnects remains a significant challenge.

3

Continuous wave lasing from individual GaAs-AlGaAs core-shell nanowires

As presented in the previous chapter, pulsed lasing from individual III-V nanowires holds strong potential for on-chip data communication and processing applications [32][31]. Nanowire lasers provide intense localized light emission in a geometry suitable for monolithic integration onto silicon substrates [36], and furthermore, they facilitate coupling to proximal waveguides with much promise for integration into future III-V on silicon optical interconnects [57][110][56].
Subject to pulsed excitation, nanowire lasers are capable of ultrafast pulse emission [66] and even phase locking at picosecond timescales [38]. However, the high time averaged excitation power and consequent strong heat dissipation has complicated continuous wave lasing of nanowire lasers and which, despite the high commercial relevance of this operation mode, has received comparably little attention to date. Very recently continuous wave (CW) lasing of nanowire laser was demonstrated in the visible regime from CdS nanowire lasers[63].
The pulsed and the continuous wave operation mode suggest two potential approaches for optical information encoding on the light generated by nanowire lasers:

- Direct switching (on and off) using a nanowire laser operating in the **pulsed** mode,

- External (e.g. phase or amplitude) modulation of light from a **continuous wave** nanowire laser.

The low energy consumption and extremely high operational speeds of electro optical modulators that manipulate light from continuous wave sources have made the approach using external modulation the favored technology for high-speed data communication in optical networks during the past decade. Very recently, on-chip optical signal processing between a memory and a processor device has been realized using an external continuous wave source [17]. The electronic-photonic system integrates over 70 million transistors and 850 photonic components on a single chip, performing calculations at a speed of 2.5 Gbit/s directly using light from an external CW laser source[17]. From this perspective, continuous wave nanowire lasers are highly desired as they could be integrated directly on microchips and coupled to optical modulators to facilitate fully on-chip logic operations using light, as discussed

in chapter 1. This combination of coherent on-chip light sources with existing electro optical modulators and all-optical switches [57] could soon realize the vision of fully functional optical microchips. However, despite significant progress in demonstrating diverse functionalities as well as various different semiconductor nanowire materials capable of lasing operation, the majority of investigations reported to date have focused on lasing under pulsed optical excitation [42][35][56][36][53][111][74] [72][31][32][71][112]. Clearly, pulsed excitation benefits from the relatively uncritical thermal effects, since the optically induced heat is easily dissipated to the substrate or nanowire/air interface between two excitation pulse cycles. This prevents depopulation of the lasing levels by thermal activation and the associated degradation of the nanowire laser performance. For high-speed signal processing using the well established technology of optical modulators and switches however, continuous wave lasing operation is required. We emphasize that besides these visionary ideas, continuous wave nanowire lasers could provide a highly cost and energy efficient alternative too many todays continuous wave semiconductor lasers as used in various applications ranging from simple barcode scanners to modern gas sensors. Although there is still a gap between the performance of nanowire lasers in terms of e.g. linewidth and output power compared to commercially available devices, possible improvements of the nanowire laser cavity can be engineered [103] to compete with existing lasers devices and boost new technologies such as photonic microchips that require monolithically integrated light sources at the nano scale [36].
The main difficulty associated with continuous wave lasing from semiconductor nanowires is the high time integrated optical power required to exceed threshold that is anticipated to result in stronger heating effects thereby reducing lasing stability [66] [53][113]. As a consequence, only very few examples of continuous wave lasing operation in semiconductor nanowires have been reported to date, such as CdS nanowires or ZnO nanowires, which lase in the visible to ultraviolet spectral range [63][114].

For nanowire lasers emitting in the infrared (IR) spectral range, GaAs-, GaSb-, or InP-based materials are used [35][56][72][31][32][71][112]. Theoretical calculations of the modal gain suggest that continuous wave lasing should be within reach in individual detached nanowires [62][73]. This would be particularly appealing for the technologically relevant GaAs-based nanowires, since they represent one of the most advanced nanowire laser systems to date [36][72][31][32][62]. Here, lasing action under pulsed optical excitation was recently demonstrated in detached GaAs-AlGaAs core-shell nanowires up to room-temperature [31][32], as well as in free-standing, vertical geometry on silicon with very high spontaneous emission coupling (β) factors [36]. In addition, epitaxial gain control has recently been reported for GaAs-AlGaAs core-shell nanowire lasers with reduced threshold via implementation of strain-free radial GaAs multi-quantum wells as active gain media [115].

This chapter presents single-mode **continuous wave** lasing from individual GaAs-

AlGaAs core-shell nanowires subject to continuous optical excitation. By comparing the s-shaped input-output characteristics of continuously excited nanowire lasers with those obtained under pulsed excitation at 4 K, we observe a $\sim 4\times$ lower equivalent pump power for continuous wave excitation and a lower minimum lasing linewidth of $\sim 200\mu$eV, indicative of the steady-state excitation conditions that result in improved temporal coherence of the emission. Analysis of the nanowire cavity length dependence of the mode characteristics reveals a clear inverse scaling behavior, with the spacing of Fabry-Perot modes corresponding to a group refractive index of ~ 8. Remarkably, when subject to continuous excitation heating of the nanowire-lasers is found to be negligible, as verified by a constant lasing linewidth as well as the absence of redshifted lasing peak emission at high excitation levels.

3.1 Experimental Setup for continuous wave nanowire lasers

In order to study the potential of III-V nanowire lasers as continuous coherent light sources at the nano scale, we study GaAs-AlGaAs nanowire lasers under continuous optical excitation. The GaAs-AlGaAs core-shell nanowire lasers investigated under continuous wave excitation were grown by solid-source molecular beam epitaxy (MBE) on SiO_2-masked Si (111) substrates. All details about the growth procedure and selected growth parameters can be found in section 2.2 and Ref. [32]. The nanowire laser structures are grown to lengths exceeding $\sim 10\mu$m and have a total diameter of ~ 360 nm, consisting of a ~ 320-nm-thick GaAs core, which is radially passivated by a ~ 10-nm thin AlGaAs layer and ~ 10-nm-thin GaAs-cap layer, respectively. These dimensions are well suited to provide excellent transverse optical confinement and wave-guiding properties, which enable single mode lasing as previously identified under pulsed optical excitation [31][32]. To characterize the lasing behavior of individual nanowire lasers under continuous wave excitation, the as-grown nanowires were dispersed onto the substrate in order to expose both their end-facets to air and therefore, achieve sufficient reflection for lasing operation [68].
First, the nanowires are removed from their growth substrate and diluted in Isopropanol using an ultrasonic bath. Afterwards, the nanowires were drop casted onto a 200nm thick SiOx layer on top of a Si substrate in order to provide sufficient optical waveguiding inside the nanowire cavity. The nanowires were studied using the confocal micro-photoluminescence spectroscopy in a He-flow exchange gas cryostat at ~ 4 K. The sample was structured with lithographically defined metallic nano structures which serve as orientation markers to identify the individual nanowires. During the mechanical transfer process, the nanowires break at different positions and thereby yield a large variation in cavity length. The nanowires investigated have a typical length of ~ 7.5-12 μm, as measured by optical microscopy. This length variation provides a useful dataset for statistical analysis of length-dependent gain and lasing characteristics.

In contrast to the μ-photoluminescence measurements using a flow cryostat as presented in the previous chapter, the results studies of the nanowires under continuous wave excitation are performed in an exchange gas cryostat mounted inside a Helium can. The experimental setup allows efficient cooling of the nanowires and sufficient heat dissipation even under continuous wave excitation despite the poor thermal anchoring of the nanowires to their dielectric (SiO_2 on Si) substrate.

As presented in Fig. 3.1, the sample was placed on a stack of x-y piezo positioners with a travel range of 5mm and a precision of $\sim$1nm in the x-y plane. A piezo positioner for the z-direction was used to focus the excitation laser onto the nanowires and collect the nanowire laser signal using an aspherical objective lens. The measurements were performed using an optics head consisting of three levels mounted on top of the cryostat:

- An excitation level consisting of the pump laser, optical mirrors for the alignment of the excitation path and a short pass filter to block residual light from the excitation laser at the signal wavelength. A power meter mounted to the ecitation level allows to measure a reference of the excitation power of the pump laser.

- A detection level consisting of mirrors for the alignment of the detection path and a fiber coupler. The incoupler consists of an optical lens and alignment mechanics which focuses the nanowire laser signal to an optical fiber.

- An imaging level consisting of a fiber entrance for the whitelight source and an imaging CCD with a longpass filter to monitor the nanowire laser luminescence and the sample surface illuminated by the white light source. Optical mirrors are used to align the imaging paths that are split by a beamsplitter to separate the white light- from the camera path.

The excitation path (green) and the detection path (red) are separated by a 30:70 beamsplitter which allows to connect both optical path with the sample. A pellicle can be flipped in and out of the excitation path to either allow the imaging of the sample or excitation and detection with maximum intensity, respectively. After the detection fiber, the nanowire laser signal is focused onto the spectrometer entrance slit using two optical lenses. Inside the spectrometer, the signal is diffracted by a 1200-mm grating and a resolution of $\sim$30 GHz and is finally detected by a charge-coupled device (CCD). The pulsed and continuous wave excitation conditions were facilitated using a pulsed laser diode (780 nm, τ_P=68 ps minimum pulse duration, repetition frequency of 80 MHz) and a continuous wave laser diode (780 nm), respectively. Note that the duration of the excitation pulses in pulsed mode is much longer than the carrier and photon dynamics in the nanowire [36][66], such that they can be described as quasi-continuous wave conditions. The maximum excitation power was $\sim$1 mW in the case of the pulsed excitation (continuous wave equivalent) and $\sim$30 mW in the case of continuous wave excitation, respectively. The power of both laser sources was adjusted directly by changing the power at the laser controllers. A typical spot size of the excitation laser was measured to be $7\pm2\mu m^2$.

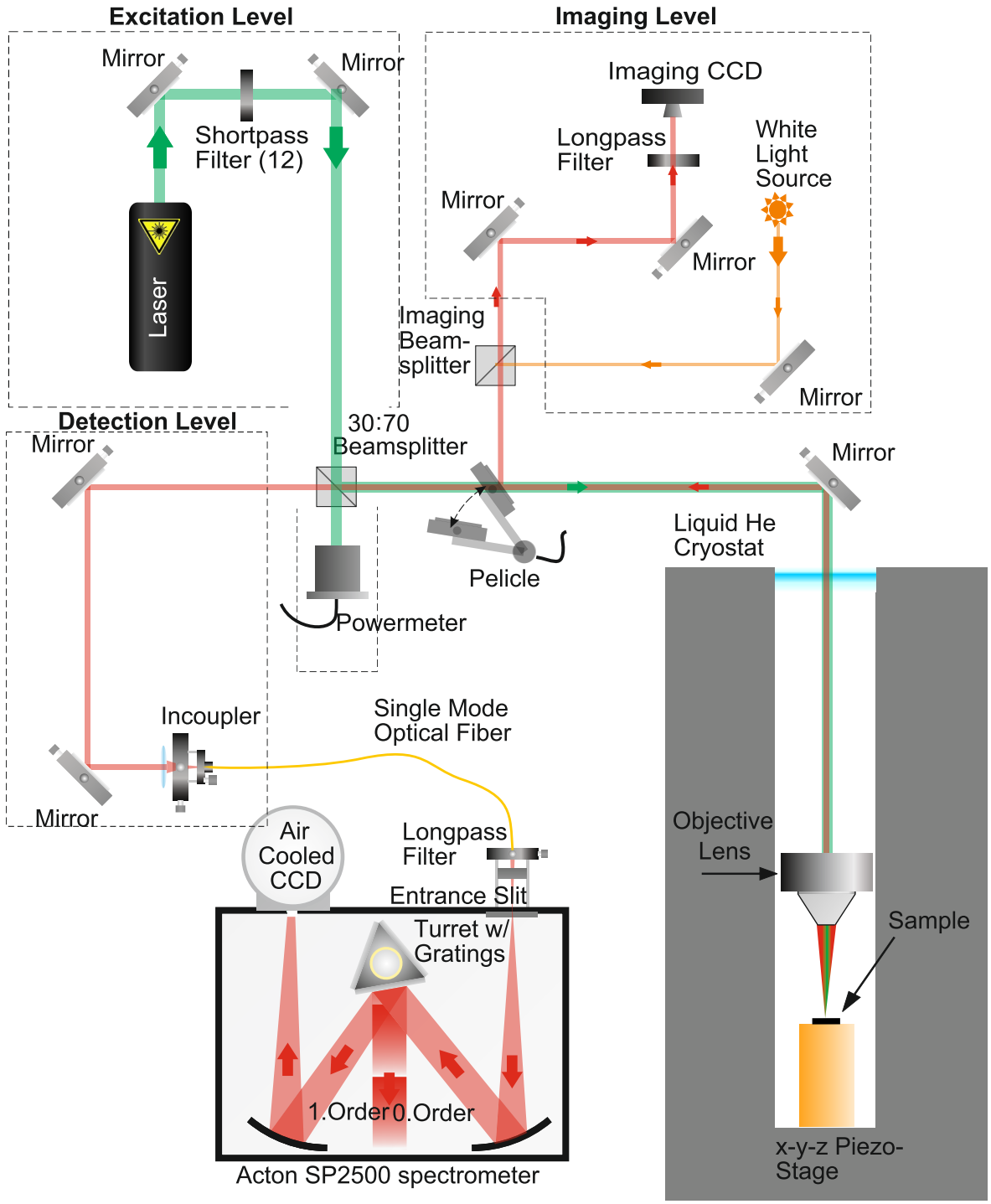

Figure 3.1. *Schematic illustration of the experimental Setup for the optical characterisation of nanowires under pulsed and CW optical excitation inside an exchange gas cryostat.*

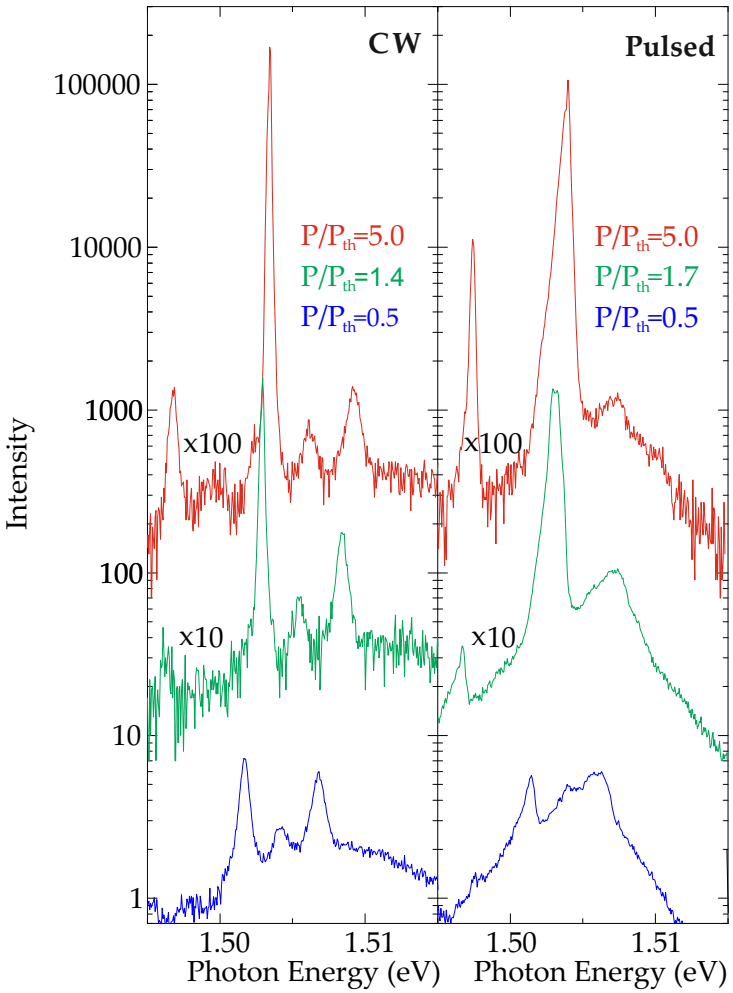

Figure 3.2. *Power dependent spectra of a single representative GaAs-AlGaAs nanowire laser under both continuous wave excitation (left) and pulsed excitation (right). The excitation power P is normalized to the threshold power (P_{th}) in order to qualitatively compare the lasing characteristics under both excitation schemes. The blue, green, and red spectra correspond to typical emission in the spontaneous emission, amplified spontaneous emission, and lasing regimes, respectively.*

3.2 Comparison of the spectral characteristics of nanowire lasers under pulsed and continuous wave operation

Exploiting the high peak power of pulsed optical excitation, lasing operation of a broad range of III-V nanowires has been demonstrated recently whereas continuous wave lasing of nanowires has hitherto received comparatively little attention. This section

presents nanowires subject to pulsed and continuous wave optical excitation and compares their lasing performance under both operation conditions.
Figure 3.2 shows a direct comparison of the low-temperature ($\sim$4 K) input-output characteristics under pulsed excitation (left panel) and continuous wave excitation (right panel) as obtained from a typical GaAs-AlGaAs core-shell nanowire (Nanowire-A) with a cavity length of 11μm. For comparative purposes, three individual spectra are illustrated for excitation power conditions of spontaneous emission (SE) below threshold (P=0.5P_{th}), amplified spontaneous emission (ASE) slightly above threshold (P$\sim$1.5P_{th}), and in the lasing regime (linear regime) far above threshold (P=5P_{th}). Here, the excitation power is normalized to the laser threshold power for (P_{th}). The CW equivalent threshold power for CW excitation and pulsed excitation was 4 mW and 0.1mW, respectively. As a result of this representation, we qualitatively find that the input-output characteristics of nanowire lasers excited under pulsed and continuous wave mode show very similar behavior. The spectra recorded under low excitation power (SE regime) are characterized by clear Fabry-Perot (FP) modulations, with a dominant mode emerging at $\sim$1.503 eV (see blue curves). From this mode, a sharp peak arises once the excitation power reaches the lasing threshold and the nanowire laser enters the ASE regime (green curves). Ultimately, this peak rises strongly non-linearly with increasing excitation power well into the lasing regime (P>2P_{th}), indicating single mode lasing for both the pulsed and continuous wave excitation cases.
Interestingly, the lasing persists as single mode characteristics up to an equivalent excitation power of P=5P_{th} until a second peak arises at 1.496 meV (red curves), from where the nanowire laser switches to bimodal lasing. Note that the increase in excitation power within the ASE and lasing regime is accompanied by a strong blueshift of the lasing peak, which can be attributed to band filling effects as the gain does not fully clamp during ASE [32].

3.3 Performance statistics of nanowire lasers subject to pulsed and continuous wave excitation

A total of fourteen nanowires were studied under both, continuous wave and pulsed excitation, allowing us to obtain statistics on the nanowire performance and their continuous wave and pulsed lasing performance. The spectra presented in Fig. 3.3 show that the variations of the optical properties of different nanowires can be very large. NW-C with a lengths of 10.6$\pm$0.3 μm exhibits only spontaneous emission up to extremely high excitation powers of 29$\pm$2mW, whereas NW-B with a length of 9.7$\pm$0.3 μm emits ASE and NW-A with a length of 11.1$\pm$0.3 μm is in the lasing regime. Although the length of the nanowires is similar, their response to strong optical pumping (29$\pm$2mW) is very different. The green curve (ASE) in Fig. 3.3 clearly shows that at least 3 Fabry-Perot modes are present simultaneously, which is a strong indication for mode competition as

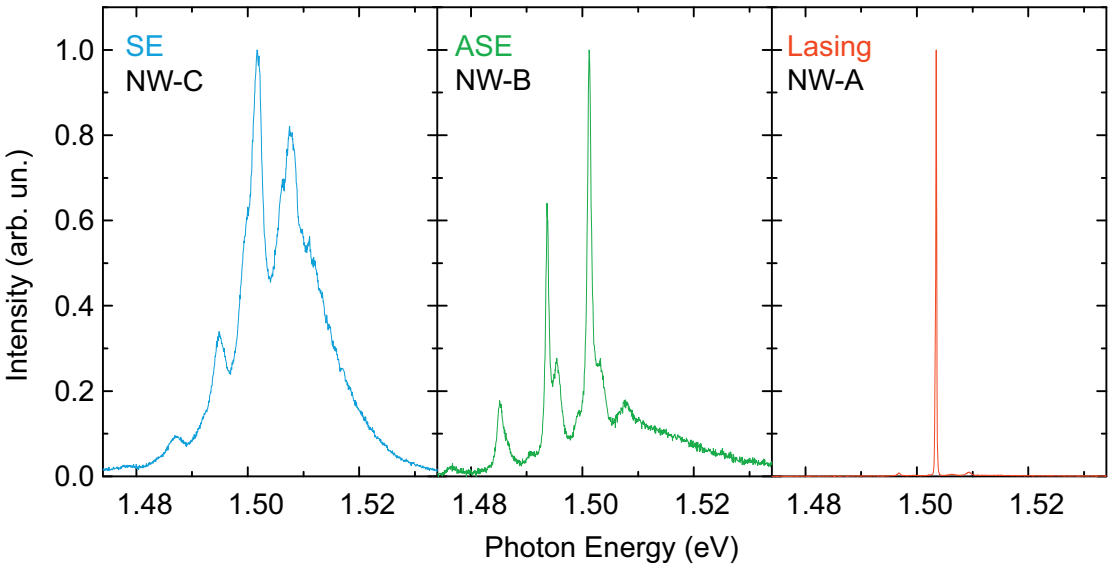

Figure 3.3. *Normalized emission spectra of three different nanowires (NW-C, NW-B and NW-A) subject to very high continuous wave excitation powers of 29±2mW. NW-A exhibits lasing operation, NW-B emits in the ASE regime and NW-C shows only spontaneous emission.*

described in the previous chapter. Furthermore, other factors resulting from the random growth and mechanical transfer of the nanowires such as the quality of the nanowire end facets, the symmetry of the nanowire waveguide and the crystals quality are expected to have an influence on the optical properties of the investigated nanowires. Figure 3.4a) shows a microscope overview image of the sample with GaAs/AlGaAs nanowires transferred to a Si/SiOx substrate with a metallic (Au) structure that facilitates the distinction of the nanowires. The random orientation and large length variation of the nanowires as shown in Fig. 3.4 results from the transfer process. The colored circles that mark the investigated nanowires in Fig. 3.4 indicates their performance limit under continuous wave excitation with a semiconductor laser source. The blue circles depict the nanowires that only exhibit spontaneous emission, the green circles depict nanowires that show a clear onset in the characteristic Input/Output curve and, finally, the red circles depicts the nanowires that unambiguously entered the lasing regime.
In general, all investigated nanowires (total of 14) exhibit clear signatures of FP modes at low excitation power and, hence, show emission in the SE regime, independent of excitation under pulsed or continuous wave conditions. A fraction of 8/14 of these nanowires reach the ASE regime under continuous wave excitation, whereas almost all nanowires (11/14) reach the ASE regime subject to pulsed excitation. Finally, nearly all nanowires (12/14) enter the lasing regime under pulsed excitation and a fraction of 6/14 of the nanowires lases under continuous wave excitation.
This reduction in the yield of nanowires reaching the lasing regime under continu-

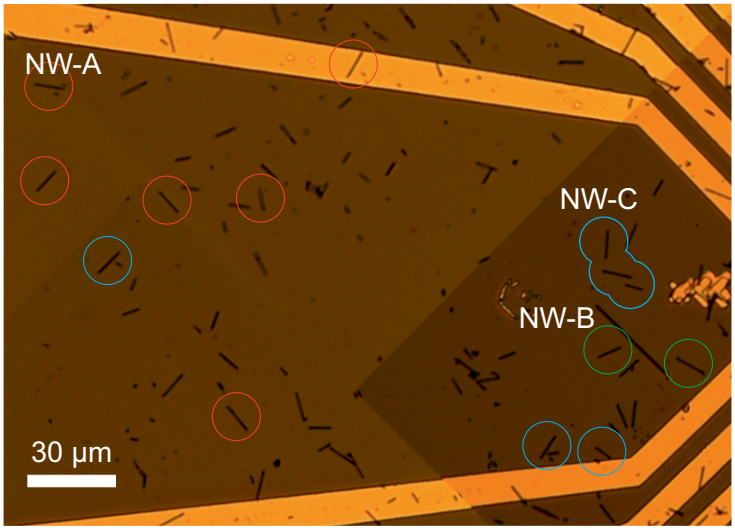

Figure 3.4. *Microscope image of the investigated nanowires. nanowires marked with blue circles only exhibited SE and no signature of ASE or lasing, while nanowires marked with green circles showed ASE and nanowires encircled in red reached lasing.*

ous wave excitation could be attributed to the limitation by the maximum continuous wave equivalent excitation power (∼30 mW) as well as excess heat generation in some nanowires under very high excitation. Consequently, the high thermal energy of charge carriers would lead to a depopulation of the lasing state and a strong reduction of the gain. However, in nanowires exhibiting clear lasing behavior, heating is not considered to be prominent. This is confirmed by the absence of a measurable redshift of the lasing peak emission in continuous wave mode compared to pulsed mode that would be expected for an increase of the lattice temperature within the gain medium.
Interestingly, while still 6/14 of the investigated nanowires exhibit continuous wave lasing, the lasing threshold does not exhibit a distinct 1/L-dependence as reflected by the large variations of the nanowire spectra presented for similar nanowires in figure 3.3. We attribute this independence to variations in the quality of the nanowire end facets, changes in symmetry of the hexagonal nanowire cross-section, different crystalline quality between different nanowires, and mode competition of different modes particularly when nanowires switch from single-mode to bimodal lasing.
We note that the diameter of the excitation spot was typically much smaller (typical spotsize: $7\pm2\mu m^2$) than the nanowire length (∼7-12.5 μm). Furthermore, we find that for some nanowires, excitation on the edge of the nanowires can lead to lower lasing thresholds than excitation in the nanowire center whereas for other nanowires excitation in the center is more efficient. An explanation could be that light focused onto the nanowire end-facets can directly couple to optical modes inside the nanowire and, other than in a situation with the excitation spot in the nanowire center, this efficiently provides absorption of the excitation laser along the nanowire axis. However, in this

scenario, only a fraction of the light focused onto a nanowire end-facet can be coupled into the nanowire and contribute to the generation of excited states in the gain material. Furthermore, as lasing operation requires population inversion throughout the entire nanowire, diffusion is expected to play a major role, since excitation in the nanowire center can be sufficient to reach the lasing threshold, although without diffusion effects a large fraction of the nanowire would absorb the generated light. Depending on the individual nanowire geometry and gain material quality, the excitation spot position can strongly impact the nanowire laser performance. Therefore, we optimized the excitation spot on each nanowire individually to obtain the highest output.
The high yield of continuous wave nanowire lasers ($\sim$50%) can be explained considering that the threshold energy under pulsed excitation must be provided to invert the nanowire gain medium and to reach the lasing threshold each time an excitation pulse hits the nanowire, whereas in contrast, continuous wave excitation of the nanowires induces a steady state between photon and gain dynamics and compensates losses continuously after the threshold is reached. Overall, the fact that continuous wave lasing is readily established here can be attributed to two factors: (a) The employment of an exchange gas cryostat during the measurement effectively cooling the nanowire laser. This is verified by the absence of redshifted lasing peak emission under strong optical pumping (Fig. 3.2) as well as by a constant lasing linewidth at high excitation levels as presented in the next section (Fig. 3.8)). (b) As the time between two subsequent excitation pulses of 12.5ns is much longer than the typical spontaneous emission lifetime of GaAs/AlGaAs core shell nanowires of $\sim$ 1ns [36] [31], the excited state is almost completely depopulated when a subsequent excitation pulse excites the nanowire. Therefore, most of the energy from the excitation pulse absorbed by the nanowire is consumed to invert the nanowire gain medium and to reach the lasing threshold, whereas continuous wave excitation induces a steady state between photon and gain dynamics, and compensates losses continuously after the threshold is reached [5]. Comparing the total energy consumption of the NW laser under pulsed and CW operation at time scales τ_P=68ps, the energy emitted by the CW pump is lower, as it only compensates the carrier losses during a time τ_P whereas the excitation pulse has to re-populate almost the entire excited state level.

3.4 Comparison of the Input-Output characteristics of nanowire lasers under continuous wave and pulsed excitation

This section compares the characteristic Input/Output curves of a nanowire laser under continuous wave and pulsed optical excitation to provide an analysis of nanowire lasing in both operation modes.
Figure 3.5 clearly depicts the input-output characteristics of the nanowire presented in Fig. 3.2(Nanowire-A) both on a linear scale (Fig. 3.5a)) and on a logarithmic scale

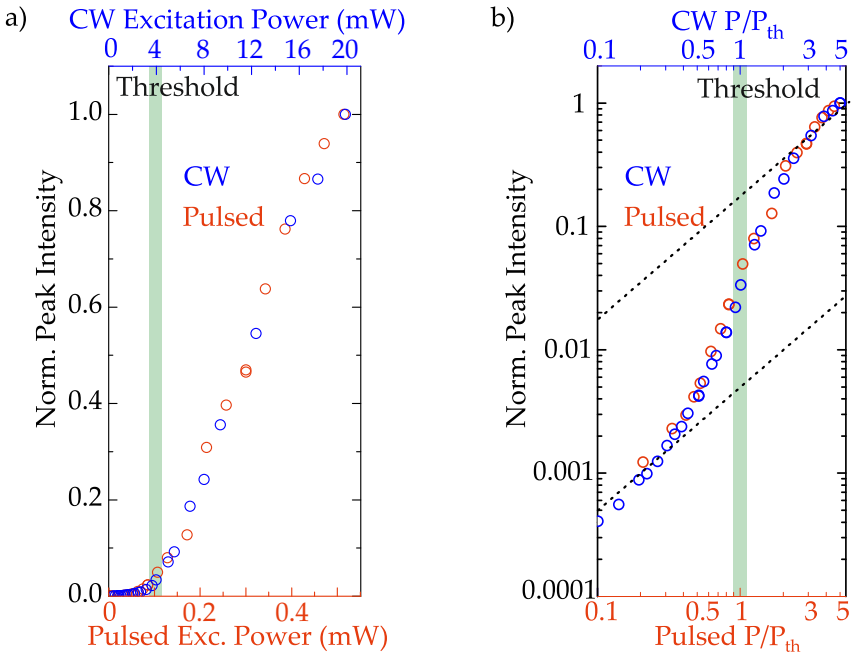

Figure 3.5. *Characteristic input-output curves presented in linear (a) and logarithmic (b) representation, as obtained from the nanowire laser in Fig. 3.2 under pulsed (red data points) and continuous wave (blue data points) excitation. The linear dependence of the peak intensity as a function of excitation power below and far above the lasing threshold (green bar) is depicted by dashed lines in (b).*

(Fig. 3.5b)). In addition to the normalized power values, we also give here the excitation power values in absolute numbers (units of mW, determined by using the reference value from the powermeter and a splitting ratio of 30(to sample):70(to powermeter) from the beamsplitter, as shown in Fig. 3.1). Calculating the threshold pump fluence under pulsed optical excitation using a typical spotsize of 7 μm^2 leads to low threshold values ranging from *sim*7 to $\sim$60 μJ/(pulse cm^2). The linear plot in Fig. 3.5a) allows to directly extract the lasing threshold via interpolation of the slope of the output curve to the intercept with the excitation power axis, whereas the logarithmic plot demonstrates the expected s-shape characteristics of the nanowire laser. Note that for the ease of comparison, the excitation power range on the bottom axis is chosen in such a way that the values of the lasing threshold measured under continuous wave and pulsed mode coincide.

This presentation shows that the input-output characteristics under both excitation schemes overlap perfectly, despite the fact that the time integrated pumping power under continuous wave excitation (blue data) exceeds the pulsed excitation (red data) by a factor of $\sim$40$\times$. This corroborates our statements above that heating effects do not play a significant role for excitation powers up to P/P$_{th}$=5.

The perfect coincidence of the input-output characteristics during continuous wave and pulsed excitation is further reproduced in the logarithmic representation in Fig. (3.5b)). The data clearly exhibit the typical s-shape dependence, including the linear SE regime ($P/P_{th}<1$), the highly non-linear ASE regime ($1<P/P_{th}<2$) and the linear lasing regime ($P/P_{th}>2$). From the direct overlap of the two input-output curves, we can directly assess the absolute threshold power for both excitation schemes.
We calculate the total energy of a single pulse at the lasing threshold by dividing the continuous wave equivalent threshold power with the repetition rate R (80 MHz) of the excitation laser: E_{th}^{pulse}=0.1mW/80MHz=1.3pJ. The total energy provided by the continuous wave laser under threshold conditions and during an exposure time comparable to pulsed excitation can be calculated by multiplying the continuous wave threshold power with the pulse duration: E_{th}^{CW}=4mW $\times$ 68ps = 0.27 pJ. As the power of the excitation laser was adjusted directly at the laser controller, the temporal width of the excitation laser pulses from the Picoquant LDH-P-780 diode increases with increasing intensity. However, as the excitation power at the laser threshold (P_{th}) of the nanowire laser (NW-A) is significantly lower than the maximum excitation power (P_{max}): $P_{max}/P_{th}>4$, we use the minimum pulse width of τ_P=68ps for the estimation.
The estimation shows that the total energy provided during τ_P=68 ps of exposure is $\sim 4.9\times$ lower for continuous wave lasing than under pulsed conditions. This can be explained by the fact that under pulsed excitation, the excited state is almost completely depopulated when the subsequent excitation pulse excites the nanowire, as the time between two subsequent excitation pulses of 12.5ns is much longer than the typical spontaneous emission lifetime of GaAs/AlGaAs core shell nanowires of $\sim$ 1ns [36] [31]. Therefore, most of the energy from the excitation pulse absorbed by the nanowire is consumed to invert the nanowire gain medium and to reach the lasing threshold each time an excitation pulse acts on the nanowire. In contrast, continuous wave excitation induces a steady state between photon and gain dynamics, and compensates losses continuously after the threshold is reached [5]. Comparing the total emitted energy within τ_{CW}=68ps of CW excitation compared with a pulse with a duration of τ_P=68ps, the CW pump has to only compensate the carrier losses during 68ps whereas the excitation pulse has to re-populate almost the entire excited state level. This finally reduces the energy consumption of a CW nanowire laser regarding exposure times $\leq \tau_P$=68ps compared to pulsed operation.

3.5 Gain pinning in GaAs/AlGaAs nanowire lasers

Finally, we present evidence for gain pinning in GaAs/AlGaAs nanowire lasers subject to pulsed and continuous wave excitation. This evidence can be obtained from the occurence of spontaneous emission clamping after the lasing threshold is reached. Figure 3.6 shows the spontaneous emission of NW-A subject to continuous wave (blue,

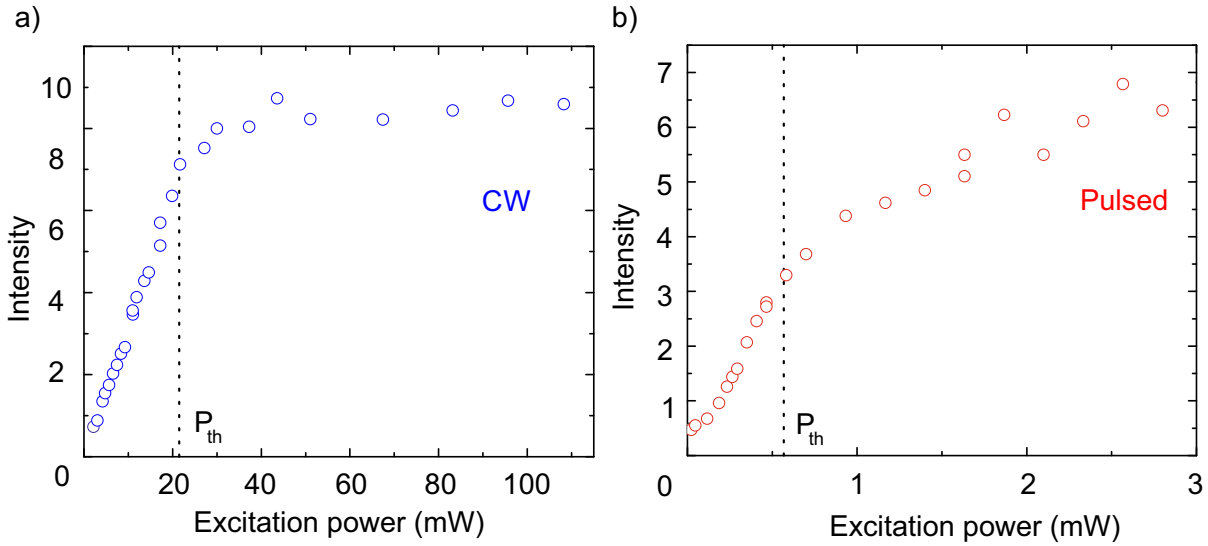

Figure 3.6. *Integrated spontaneous emission intensity as a function of excitation power: a) Spontaneous emission from NW-A subject to continuous wave (blue) excitation integrated over the interval between 1.505eV-1.515eV. b) Spontaneous emission from NW-A subject to pulsed (red) excitation integrated over the interval between 1.507eV-1.517eV. The lasing threshold is indicated by the dashed lines.*

Fig. 3.6a) and pulsed excitation (red, Fig. 3.6b) as a function of the excitation power. The spontaneous emission intensity shown in Fig. 3.6 is obtained by integrating the photoluminescence of the nanowire in an interval at photon energies higher that the lasing peak (Fig. 3.6a) 1.505eV-1.515eV and Fig. 3.6b): 1.507eV-1.517eV), in order to analyze the spontaneous emission without the lasing emission. The spontaneous emission intensity presented in Fig. 3.6a) clearly saturates and finally stays constant after the lasing threshold (dashed line) is reached. After the lasing threshold (P_{th}=4mW) is reached, stimulated emission becomes the dominant radiative process and carriers continuously fill and depopulate the lasing state by phonon scattering and stimulated emission, respectively. Consequently, excited carriers in excess of the critical carrier concentration for lasing operation (n_c) do not contribute to spontaneous emission. Carrier population in excess of n_c is depopulated by stimulated emission, leading to a pinning of the carrier concentration in the nanowire, and therefore, gain pinning at high excitation powers. Therefore, the clamping of the spontaneous emission intensity presented in Fig. 3.6a) clearly provides evidence for gain pinning and continuous wave lasing of the nanowire.

As shown in Fig. 3.6b), the saturation of the spontaneous emission of the nanowire is also observed if the nanowire is optically pumped with a τ_P=68ps pulsed excitation laser. However, the spontaneous emission intensity presented in Fig. 3.6b) does not fully saturate above the lasing threshold (P_{th}=0.1mW). This can be attributed to the

strong variation of the excitation power during the excitation of the pump pulse which continuously changes the carrier concentration in the nanowire. Therefore, at a certain time interval during optical pumping, the threshold carrier concentration n_c and gain pinning is reached, whereas at other time intervals, carrier concentrations below n_c are provided. The time intervals with carrier concentrations $<n_c$ contribute predominantly to spontaneous emission. According to the specifications of the pulsed excitation laser (Picoquant LDH-P-780), the temporal lineshape of the excitation pulse becomes increasingly asymetric and the pulseduration τ_P increases at high excitation powers. Therefore, the contribution of time intervals of spontaneous emission to time integrated spectra can increase, leading to an absence of full gain pinning and slightly increasing spontaneous emission with increasing excitation powers.

3.6 Fabry-Perot mode spacing and experimental group refractive index

In general, it is intriguing that despite fundamentally different charge and photon dynamics under pulsed and continuous wave excitation, the investigated nanowire exhibits similar lasing characteristics under the two excitation schemes. To better understand the nature of the nanowire cavity required to achieve continuous wave lasing and to identify which mode dominates the lasing operation in comparison to conditions of pulsed excitation, we investigated a large set of nanowires with different nanowire cavity lengths.

Figure 3.7 plots the FP mode spacing as a function of 1/L (L, cavity (NW) length) for a variety of different nanowire lasers as presented in the optical microscope image of Fig. 3.4a). The mode spacing and the inverse of the cavity length 1/L follow nicely the expected linear dependence of a Fabry-Perot type cavity where the cavity length L is a multiple integer (k) of the half wavelength of light in a nanowire waveguide mode $\lambda_{WGmode}/2$: L=k$\times\lambda_{WGmode}/2$. For the Fabry-Perot mode spacing ΔE between two neighboring modes with energies E_{k+1} and E_k, this results

$$\Delta E = \frac{hc}{2n_g} \times \frac{1}{L}, \tag{3.1}$$

[74] where h denotes the Planck constant, c denotes the speed of light and n_g denotes the group refractive index of the nanowire waveguide mode[116].

Interestingly, we find that the absolute values of the mode spacing differ strongly between the nanowires. For example, at $L = 11\mu$m, the mode spacing can exhibit a spread as high as $\pm$4.5 meV. This may arise from slight asymmetries in the geometry of different nanowires that influences the dispersion of the lasing mode in the nanowires and thus, leads to variations of the group refractive index. Furthermore, the different nanowires can provide lowest threshold gain for various fundamental modes (e.g., HE_11, HE_31 and TE_01) with deviating group refractive indices [68]. This is confirmed by the

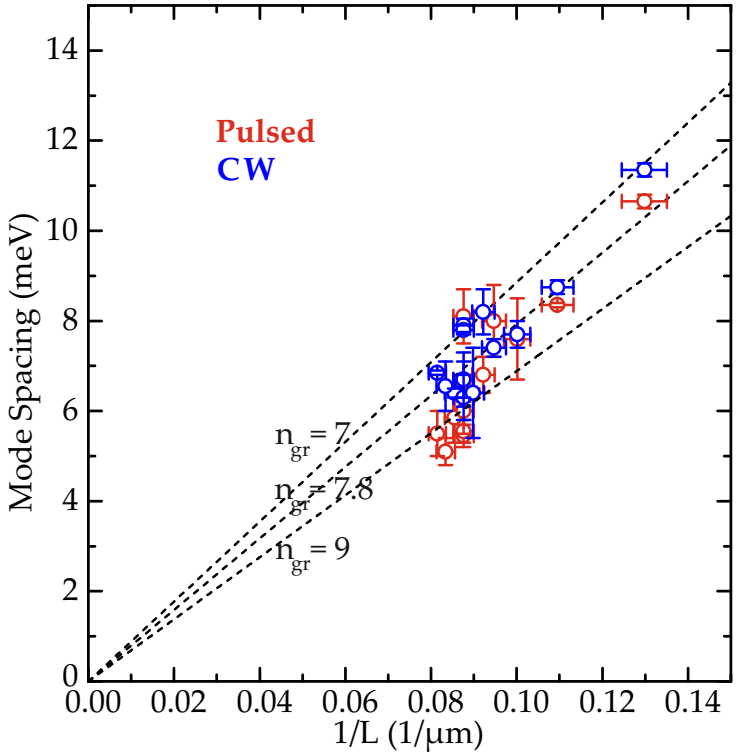

Figure 3.7. *Fabry-Perot mode spacing of different nanowires as a function of the inverse nanowire cavity length (1/L) for excitation conditions under continuous wave mode (blue) as well as pulsed mode (red). Error bars in mode spacing (∼ ±1 meV) are due to deviations from the perfect periodicity within a given nanowire, while error bars in 1/L arise from the inaccuracy of determining nanowire length in optical microscopy; best fit to the 1/L-dependence of the mode spacing yields a slope of 79±2 meV µm corresponding to n_g=7.8. Additional fits corresponding to n_g=7 and n_g=9 are shown.*

overall $1/L$ dependence of the mode spacing as shown in Fig. 3.7. Figure 3.7 depicts the experimental data together with the theoretical curves for three different group refractive indices (n_g=7, n_g=7.8, n_g=9). A best fit to the $1/L$-dependence of the mode spacing using the fit function given by equation 3.1a) exhibits a slope of h×c / $2n_g$ = 79±2 meV μm, which translates into a group refractive index of n_g=7.8±0.2. This value is in excellent agreement with previous observations that report a group refractive index of n_g ∼8 in GaAs nanowires as well as in ZnSe nanowires [75][117].
The strong reduction of the photon propagation velocity inside the nanowire down to c/8 supports high end-facet reflectivities and, consequently, enables the low lasing threshold required for continuous wave operation.

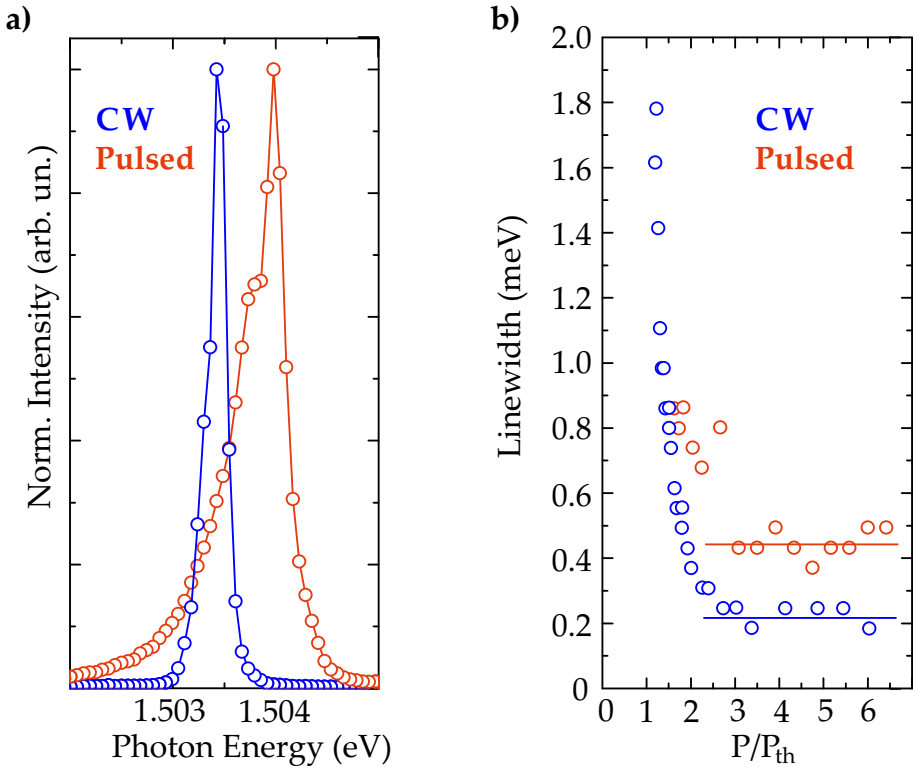

Figure 3.8. *a)Normalized nanowire laser spectra under pulsed (red) and continuous wave (blue) pumping at a fixed excitation power of P/P_{th}=6. b) Linewidth of the lasing emission as obtained from the spectra given in Fig. 3.2 as a function of the excitation power under pulsed (red) and continuous wave (blue) excitation. The red and blue lines serve as guides to the eye for the saturation of the nanowire laser linewidth.*

3.7 Comparison of the spectral linewidth of nanowire lasers under continuous wave and pulsed excitation

Besides the low equivalent threshold pump power of continuous wave compared to pulsed excitation of the nanowire lasers, the characteristic steady state dynamics of the continuous operation are also reflected in the laser linewidth as shown in Fig. 3.8a). Figure 3.8b) shows the laser linewidth as a function of the excitation power for both excitation conditions. Once the nanowire laser reaches threshold, the linewidth of the dominant FP mode decreases substantially in the ASE regime as observed for both pulsed (red data) as well as for continuous wave conditions (blue data). For excitation powers in the lasing regime (P/P_{th}>2), the laser linewidth remains fixed at a minimum in both cases. The absence of a further reduction of the linewidth with increasing excitation power, and therefore, the deviation from the Schawlow-Townes-Limit as given in equation 2.11 could be attributed to variations of the real refractive index of the gain material with carrier density [97], especially as the nanowire gain medium is

not pumped homogeneously, and spontaneous emission induced phase and intensity changes in the laser field [97], limit the temporal and spatial coherence.
Interestingly, the minimum laser linewidth of 0.2 meV under continuous wave excitation is a factor of 2× sharper than the corresponding linewidth observed under pulsed excitation (0.4 meV). The stability of the laser linewidth under continuous wave conditions also supports the conclusion that excess heat generation is negligible under the employed excitation conditions. Furthermore, the sharp linewidth is a strong indication for the enhanced temporal coherence.
In previous experiments that used pulsed excitation using 200 fs duration pulses, a strong linewidth broadening >1 meV was observed towards high pumping powers (P/P_{th}>2) consistent with the short laser pulse emission [36][31][32][66], and in complete contrast to the lower and saturated linewidths identified here under continuous wave excitation. This can be understood by the fact that under ultrafast (fs) excitation, an increase of the excitation power leads to a decrease of the temporal emission properties, indicating that the linewidth becomes Fourier-limited. Furthermore, ultrafast-dynamics such as Rabi oscillations in the 100GHz range [38] as presented in chapter 5, can have an impact on the spectral line profile of the nanowire laser subject to ultrafast (fs) excitation pulses.
In contrast, under excitation using 68 ps pulses, the emission is not limited by the gain dynamics as excitation prevails for several tens of ps after the nanowire laser emission is initiated [36][66]. Consequently, the duration of the nanowire laser emission is not limited by the gain dynamics but by the duration of the excitation. This leads to sharp laser peaks as low as 0.4 meV even for the pulsed excitation power of up to P/P_{th}=5.
Finally, we emphasize that continuous wave excitation establishes a steady state between losses, gain, and photon dynamics that strongly suppresses parasitic ASE and SE. In contrast, pulsed excitation with pulse durations of 68 ps provides a strong gradient of excitation powers during the excitation and, thus, supports SE, ASE, and lasing at different times. Evidence for gain dynamics at timescales $\ll$68ps is provided in chapter 4 and chapter 5 [36] [38], showing fourier limited pulse emission and Rabi oscillations at timescales <10ps, respectively. Ultrafast pulse emission of nanowire lasers is also presented in [66]. As a result, the time integrated spectra exhibit a broad low energy tail as shown by the red curve in Fig. 3.8a) that stems from various levels of band filling during the excitation. However, the steep high energy tail of the lasing peak under pulsed excitation is comparable to the high energy tail of the lasing peak under continuous wave excitation (blue curve in Fig. 3.8a)).
In summary we can identify three linewidth regimes corresponding to the different excitation pulse durations ($\Delta\tau$):

- $\Delta\tau$<1ps: Fourier Limited linewidth broadening up to >1meV (see results presented in chapter 4 and 5) [36] [38].
- $\Delta\tau$<70ps: Excitation power variation induced linewidth broadening to $\sim$0.4meV.
- $\Delta\tau \rightarrow \infty$: Steady state operation with linewidths down to 0.2meV.

Therefore, the absence of the broad low energy tail and the consequent extremely low linewidth of 0.2 meV under continuous wave excitation as shown in Fig. 3.8a) is a direct result of the steady state conditions established during continuous wave excitation. On the other hand, the linewidth under pulsed excitation using either 68 ps or fs-short pulses [36][31][32] suffers from parasitic SE and ASE or Fourier-limited linewidth, respectively. Moreover, the time integrated spectra further show that the lasing peak positions between continuous wave and pulsed excitation are nearly identical, confirming that heating is negligible (see the temperature dependence of the spectral emission of GaAs/AlGaAs nanowire lasers presented in chapter 2 Fig. 2.19). The fact that the lasing peak position under continuous wave excitation is slightly red-shifted (0.5 meV) results from a saturated peak position at increased excitation power, which is expected due to the steady-state operation that continuously provides seed photons at the fixed laser frequency.

3.8 Summary

In this chapter, we explored continuous wave lasing from individual GaAs-AlGaAs core-shell nanowires exhibiting several improved characteristics compared to nanowires subject to pulsed excitation. Interestingly, despite $\sim$40$\times$ higher time averaged excitation powers, $\sim$50% of the investigated nanowires exhibit continuous wave lasing operation. In particular, we emphasize that the continuous wave-mode nanowire lasers as measured on SiO_2/Si substrate do not suffer from anticipated excess heat generation at least up to excitation power levels of $\sim$5$\times$ the equivalent threshold power. Moreover, the threshold peak energy for continuous wave lasing is $\sim$4$\times$ lower than the corresponding threshold peak energy under pulsed excitation, as directly measured on an identical nanowire laser. Ultimately, the continuous wave lasing benefits from the extremely low lasing linewidth as low as 200 μeV as a consequence of the steady state conditions.

4

Monolithically integrated high-beta nanowire lasers on silicon

As discussed in chapter 1, ultra-compact all-optical interconnects on silicon are required for enhanced data processing speeds whilst minimizing the energy cost per bit [118]. However, integrating materials providing significant gain onto silicon chips and realizing lasers remains a major challenge. Therefore, solutions for the monolithic integration of lasers onto silicon are widely considered as the holy-grail for chip-level optical interconnects [35].

In this respect, III-V semiconductor nanowires are of particular interest [42] [43][44][45] since their small footprint facilitates direct growth on silicon [119] [47]. Furthermore, their unique one-dimensional structure and high refractive index naturally facilitate low loss optical waveguiding and potentially provides light recirculation in the active nanowire-core region. However, the low refractive index contrast between the nanowire and the silicon substrate provides poor modal reflectivity (< 1%) and, therefore, nanowires are typically removed from the growth substrate to achieve lasing [61][31][32][52]. Several groups have reported lasing from nanowires over the past few years for a large range of semiconductor materials spanning the ultra-violet, visible and near infra-red spectral ranges [32][53][54] [55][56][62], but lasing from nanowires on silicon has not been achieved to date.

Recently, tapered InGaAs nanopillars supporting higher order helical optical modes have been shown to lase on silicon [35][60]. However, their comparatively large footprint and multimode resonator structure typically lead to a complex far-field radiation pattern, low spontaneous emission coupling factors ($\beta \sim 0.01$) and, consequently, high pump thresholds for lasing.

In this chapter, we demonstrate how by inserting a tailored dielectric inter-layer at the nanowire-Si interface, low-threshold single mode lasing can be achieved in vertical-cavity GaAs-AlGaAs core-shell nanowire lasers on silicon. By exploring the output from the nanowire, we measure very high spontaneous emission factors comparable to state of the art nanocavity lasers (β=0.2), and achieve ultra-low threshold pump energies $\leq$11pJ.

Analysis of the power dependence of the lasing emission linewidth demonstrates the po-

tential for high pulsation rates ≥250GHz. Such ultrafast and highly efficient nanolasers grown monolithically on silicon are very promising light sources for the realization of chip-level optical interconnects.

4.1 Monolithically integrated nanowire lasers

This section presents a novel nanowire laser structure that enables light recirculation in vertically grown nanowires despite low refractive index mismatch between nanowire and substrate. The presented technique constitutes a vital technological step towards the monolithic integrated of III-V nanolaser on silicon. In this approach, the combination of a thick nanowire waveguide on top of a thin nanowire socket could simultaneously match both fundamental requirements for the realizations of nano lasers on microchips: light recirculation and direct integration on silicon [36][39][40].

Figure 4.1 shows a schematic representation of a monolithically integrated nanowire laser on silicon. The socket of the nanowire laser consists of an 80nm thick GaAs inner-core that is directly connected to the silicon substrate and surrounded by a ∼200nm thick dielectric reflection layer. Since this inner-core diameter is much too small to support low loss optical waveguiding, light propagation through the nanowire socket is prohibited. Above the dielectric interlayer, the top part of the nanowire is selectively widened to a diameter >300nm to constitute the nanowire waveguide and support the propagation of low order optical modes inside the nanowire gain medium. Consequently, light that propagates towards the nanowire socket inside the nanowire waveguide is reflected at the dielectric interface instead of being guided to the substrate. As the dielectric interface may have a much lower refractive index than the nanowire material, reflectivity enhancements of several orders of magnitude compared to conventional nanowire substrate interfaces can be achieved.

The nanowire laser structure investigated in this chapter is schematically depicted in Fig. 4.1 which shows a GaAs/AlGaAs core-shell nanowire monolithically integrated on silicon using a SiO_2 reflection layer. The comparison of the literature values of the refractive index of GaAs (n_{GaAs}=3.666) with the refractive index of SiO_2 (n_{SiO_2} ∼1.5) and Si (n_{Si}=3.673) clearly demonstrates how the presented structure dramatically increases the refractive index mismatch, and, therefore, the reflection of optical modes at the nanowire bottom. Further improvements of the presented structure can be easily implemented e.g. by removing the dielectric layer to obtain a high contrast grating or by replacing the single dielectric layer with a distributed Bragg reflector (DBR) around the nanowire socket.

In the present structure, the thick SiO_2 inter layer is designed to achieve high modal reflectivity at the base of the nanowire and, thereby, provide resonant recirculation of the lowest order optical modes for lasing. Figure 4.2 shows the result of FDTD simulations of the modal reflectivity at the nanowire-SiO_2-substrate interface for the HE_{11} and HE_{31} guided modes as a function of the thickness (t) of the SiO_2 inter-layer. The modal reflectivity of the HE_{11} mode oscillates with increasing t due to interference of

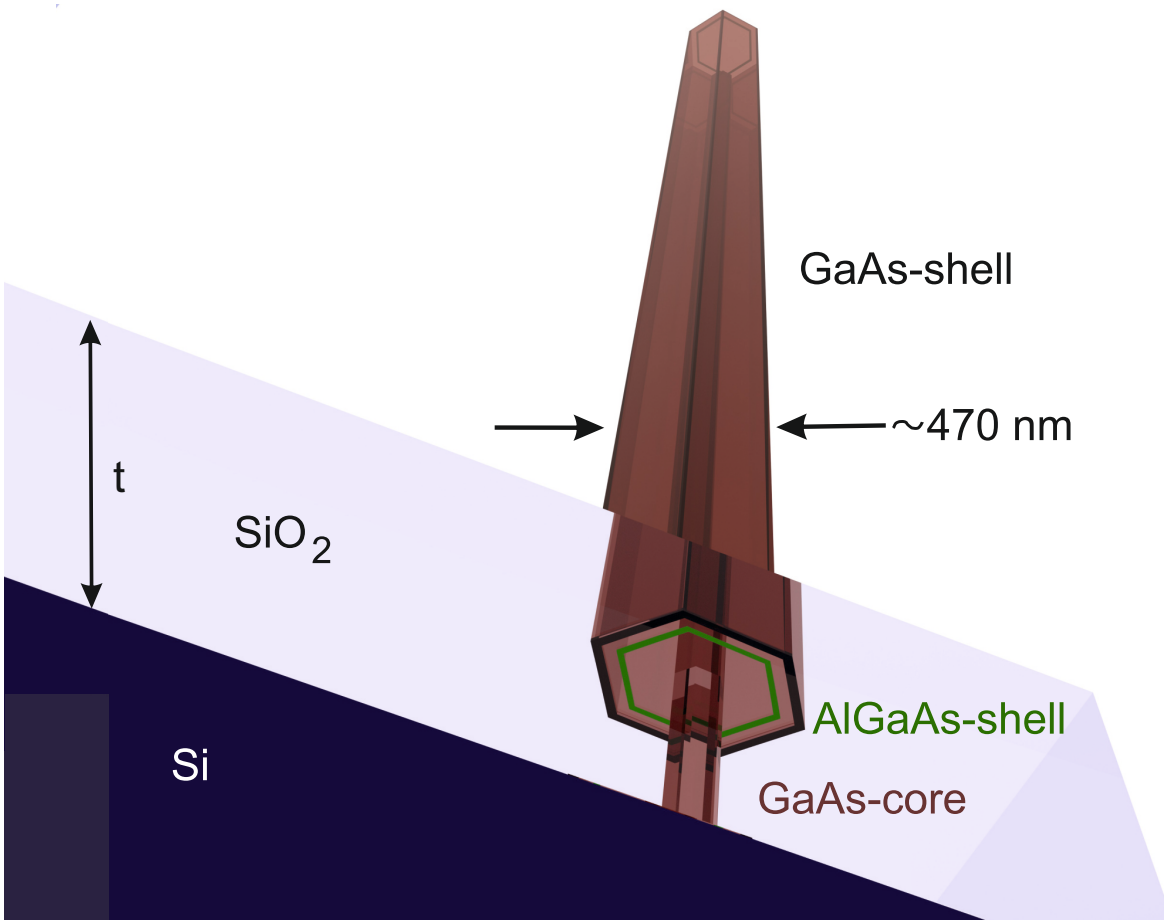

Figure 4.1. *High-β GaAs-AlGaAs nanowire laser on silicon realized using a thick dielectric SiO_2 inter-layer (light blue) to enhance the modal reflectivity of low order waveguide modes. The nanowire core is epitaxially grown into the 250nm thick SiO_2 mask opening on the silicon (111) substrate and overgrown by a GaAs-AlGaAs-GaAs shell on top of the dielectric reflection layer.*

reflected waves from the nanowire-SiO_2 and nanowire-silicon interfaces. For the HE_{11} mode, constructive interference occurs for t=160nm resulting in a modal reflectivity of up to 40%, much larger than the <1% reflectivity between the same nanowire directly attached to the silicon substrate, without the SiO_2 inter-layer. The results presented in Fig. 4.2 demonstrate that large modal reflectivities, >40% can be achieved by carefully engineering the diameter of the nano-apertures and the total nanowire diameter above the SiO_2 inter-layer.

As shown by the blue data points in Fig. 4.2, higher order modes such as HE_{31} (Fig. 4.2 - inset) exhibit even higher reflectivities $\geq$80%. Interestingly, no oscillations of the reflectivity are observed for the HE_{31} mode. This can be explained by the strong in-plane wavevector component of such higher order modes which strongly enhances the

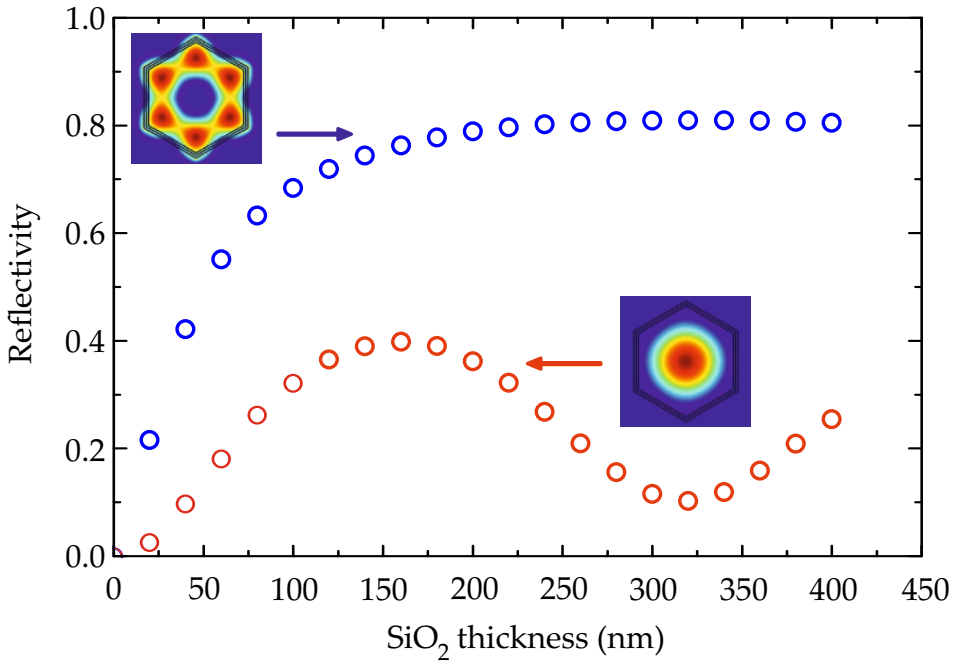

Figure 4.2. *Calculated modal reflectivity for the HE_{11} (right inset, red points) and HE_{31} (left inset, blue points) modes for a 470-nm thick nanowire at the nanowire-SiO_2-Si interface as a function of thickness of the SiO_2 interlayer.*

reflectivity at the interfaces and propagation parallel to the substrate [35]. Consequently, the optical mode is strongly reflected at the nanowire/SiO_2 interface whereas residual light that penetrates the SiO_2 propagates parallel to the substrate and does not interfere with the reflections from the upper interface that reenter the nanowire.
Depending on the desired application of the monolithically integrated nanowire lasers, the nanowire diameter can either be chosen to be small (<300nm) to support single mode waveguiding or be increased to provide lasing from higher order modes. On the one hand, fundamental mode lasing allows efficient coupling to optical fibers, whereas on the other hand higher order modes strongly support propagation parallel to the substrate and, therefore, coupling to on-chip waveguides.
As discussed in chapters 2 and 3 GaAs-AlGaAs nanowire lasers that are detached from the silicon substrate exhibit room temperature lasing for end-facet modal reflectivities of ∼60 % [32][62]. Therefore, the simulations presented in Fig. 4.2 strongly suggest that the nanowires attached to the SiO_2-silicon substrate should also exhibit lasing and that their far-field emission pattern is likely much less complex [68] as in e.g. multimode nanopillar lasers on Si [35] [60]. Indeed, the far field emission pattern from non-tapered single-mode nanowire lasers has previously been studied by Saxena et al. [68], indicating that the radiation from the nanowire facet could be well collected using a high aperture objective. The authors of [68] show that by comparing the farfield pattern of InP nanowire lasers obtained from Fourier Plane imaging of the nanowire

emission with numerical FDTD data, the optical lasing modes in can be identified. The results of [68] show that InP nanowires with a diameter of 250nm, 330nm and 460nm diameter exhibit lasing from the HE_{11} modes, the TE_{01} and the TM_{01} mode, respectively.

4.2 Site selective growth of monolithically integrated nanowire lasers

Since the precise positioning of nanowire lasers constitutes a major requirement for their potential integration into future photonic circuits, we have developed a method for the site-selective growth of nanowire lasers on silicon. To achieve sufficient reflection from the nanowire end-facets for lasing operation, 80nm holes must be fabricated inside the $\sim$200nm thick SiO_2 inter-layer, as discussed in the previous section.

A schematic illustration of the specific fabrication technique to realize 200nm deep and <100nm diameter holes in thermal SiO_2 on Si is shown in Fig. 4.3. A Si(111) wafer, covered with a thermally evaporated SiO_2 layer of 200nm thickness as shown in Fig. 4.3a) is spin-coated with the electron-beam (e-beam) resist ZEP 520A with a rotational speed of 4000rpm for 180 seconds (Fig. 4.3b)). Afterwards, the sample is placed on a hotplate at a temperature of 150°C for another 180s. The resulting ZEP layer on top of the SiO_2 has an average thickness of (400$\pm$15) nm. Due to the large differential resistance of ZEP as compared to PMMA this type of resist is highly suitable for the etching process required to produce deep holes in SiO_2.

After spin coating, 80nm holes are exposed in the ZEP layer using electron beam lithography with a dose of 190μC/cm^2 (Fig. 4.3c)). In the next step this structure can be developed in a ZED-N50 solution which removes the resist at the exposed structures and thereby introduces the hole-profile into the ZEP layer. By using an anisotropic reactive ion etching (RIE) process as shown in Fig. 4.3d) with the fluoric gas C_4F_8 this profile can be transferred to the SiO_2 layer remaining 10nm SiO_2 at the bottom of the holes. The RIE process is performed at a temperature of 15°C, a pressure of $\sim 2\times10^{-5}$ mbar, an Inductive Coupled Plasma (ICP) forward power of $\sim$400 W, a RF generator forward power of $\sim$100 W, a helium backing of $\sim$10 sccm and a DC bias voltage of $\sim$344 V.

This is the most crucial step in the fabrication process as a tradeoff between high SiO_2 etching rates and low ZEP etching must be found to achieve a sufficient hole depth of $\sim$200nm in the SiO_2. The resistivity of the ZEP layer has a remarkable dependence on the duration of the etching step which increases with decreasing etching time per etching step. Therefore, we divided the total hole etching in 6 steps with the following sequence: 4$\times$15s, 1$\times$10s and 1$\times$7sec. Afterwards, the resist is removed by a liftoff process in a ZDMAC solution for 5 minutes during a supersonic treatment (Fig. 4.3e). The result is shown in the SEM image presented in Fig. 4.3 k). Here, we cross sectioned the structure with a focused ion beam (FIB) to reveal the quality and geometry of the holes fabricated during the etching process. The SEM image reveals 80nm thick holes that deviate only

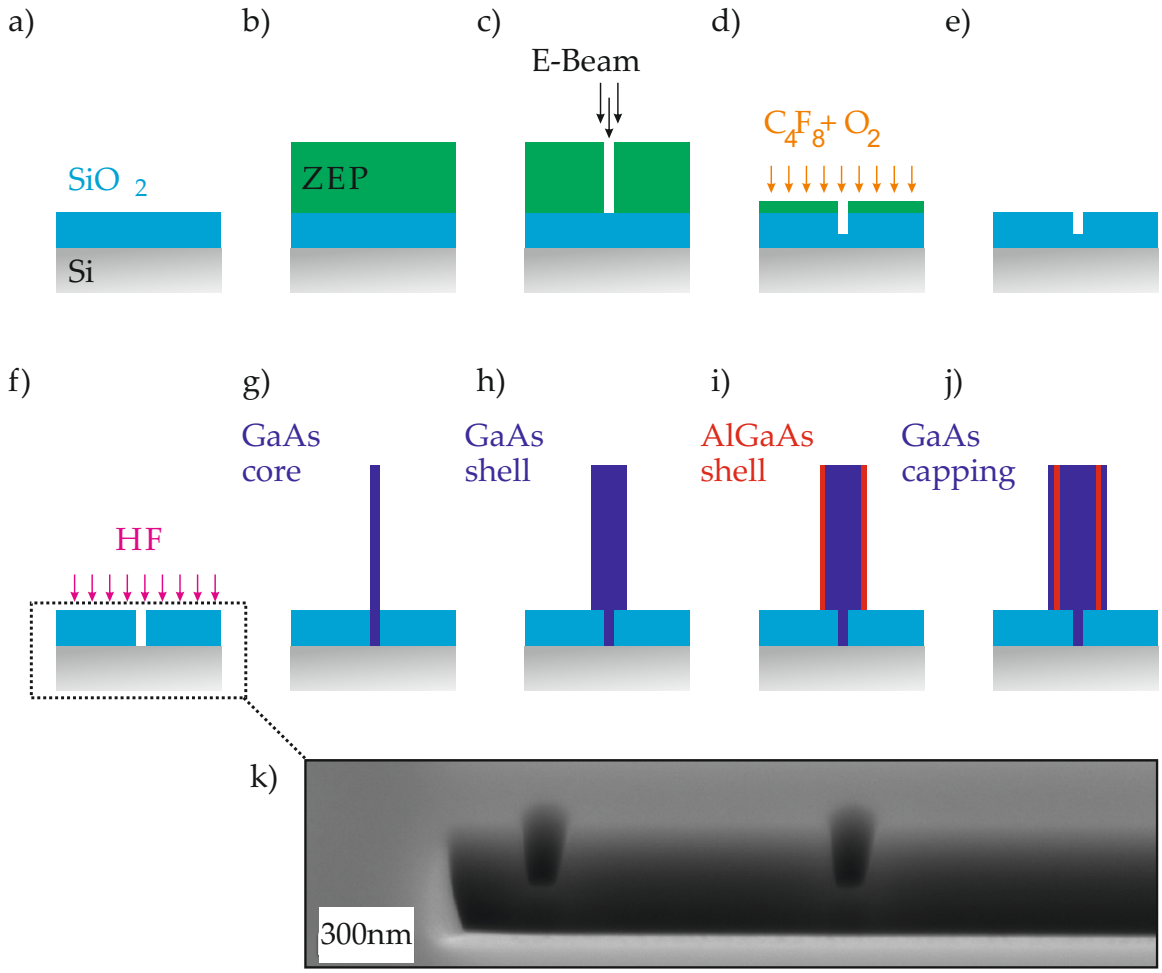

Figure 4.3. *Site selective growth of nanowire lasers on silicon: (a) The Si (grey) substrate is covered with a ∼200nm thick SiO_2 layer (blue) (b) that is spincoated with a ZEP electron beam resist (green). (c) The nano apertures are defined by electron beam exposure of the ZEP (d) and etched by RIE using C_4F_8 and O_2 (orange) into the SiO_2 layer underneath. f) A subsequent HF (purple) etching step finalizes the aperture fabrication whilst prevailing the crystalline surface of the Si substrate. g) Afterwards, a thin GaAs core is grown inside the nano apertures and h) radially overgrown with a GaAs shell on top of the SiO_2. The nanowire Lasers are finalized by i) the growth of an AlGaAs passivation layer and j) a another GaAs shell to prevent oxidation. k) Scanning electron microscope image of the holes in SiO_2 after cross sectioning by focused ion beam milling (FIB).*

$\sim$15% from their nominal values and have depths down to 206 nm.
The remaining $\sim$10 nm SiO_2 at the bottom of the holes are removed by a hydrofluoric acid (HF) etching process with an etching rate of 3.1nm/s, in order to achieve a smooth crystalline surface on the silicon required for subsequent MBE growth (Fig. 4.3f)). After cleaning the sample from all residual organic substances using Acetone, the sample can be loaded into the MBE chamber and direct growth of GaAs-AlGaAs core-shell nanowires can be induced. Afterwards, a 80 nm thick GaAs inner core can be grown from the predefined holes in the SiO_2 using solid source molecular beam epitaxy (Fig. 4.3g)). Since this inner-core diameter is much too small to support low loss optical waveguiding, the diameter of the GaAs nanowire can then be selectively widened only in the region above the SiO_2 interlayer by switching to MBE conditions favoring lateral growth (Fig. 4.3h)). In a final growth step, the nanowire surface can be passivated,[67] by using 10 nm of AlGaAs (Fig. 4.3i)) and completed with a 10 nm GaAs cap (Fig. 4.3j)) to produce core-shell GaAs-AlGaAs nanowires connected to the silicon substrate via the inner core that extends throughout the SiO_2 interlayer. Further details about the nanowire growth can be found in section 2.2 and Ref. [32].

4.3 Growth of monolithically integrate nanowire lasers using a sacrificial nanowire technique

The depth of nanostructures fabricated by optical or electron beam lithography techniques using polymer resists as presented in the previous section is limited to the etching resistance of the soft mask. However, using the structure presented in section 4.1 to fabricate monolithically integrated nanowire lasers that operate in the technologically important telecommunication wavelength region, apertures width depth >200nm will be required to provide sufficient reflection from the bottom facet of an integrated nanowire laser. Furthermore, electron beam lithography is very inconvenient compared to e.g. nano imprint lithography which speeds up the fabrication process by several orders of magnitude which can be vital for their commercial realization. However, the polymer masks used for nano imprint lithography typically do not provide the etching resistance required to fabricate >100nm deep apertures into the SiO_2. Therefore, we developed a second nanowire laser fabrication process using a nanowire hard mask technique that allows large scale implementation of deep nano apertures without the use of polymers. In order to achieve $\sim$250nm deep holes in a SiO_2 layer on top of silicon using a nanowire hard mask, a sample of sacrificial InAs nanowires with diameters of $\sim$80nm grown by MBE on Si (111) as schematically depicted in Fig. 4.4a) was used [81][47].
After the growth of InAs nanowires, a $\sim$230-nm-thick SiO_2 was sputter-deposited onto the InAs nanowire sample, creating a very thick SiO_2 layer at the base of the nanowires as depicted in Fig. 4.4b). Figure 4.4c) depicts the subsequent wet etching step in which the sample was etched in a 90:10 diluted HF solution to remove unwanted SiO_2 from the nanowire side facets. In the next step as shown in Fig.4.4d), the sample was reloaded

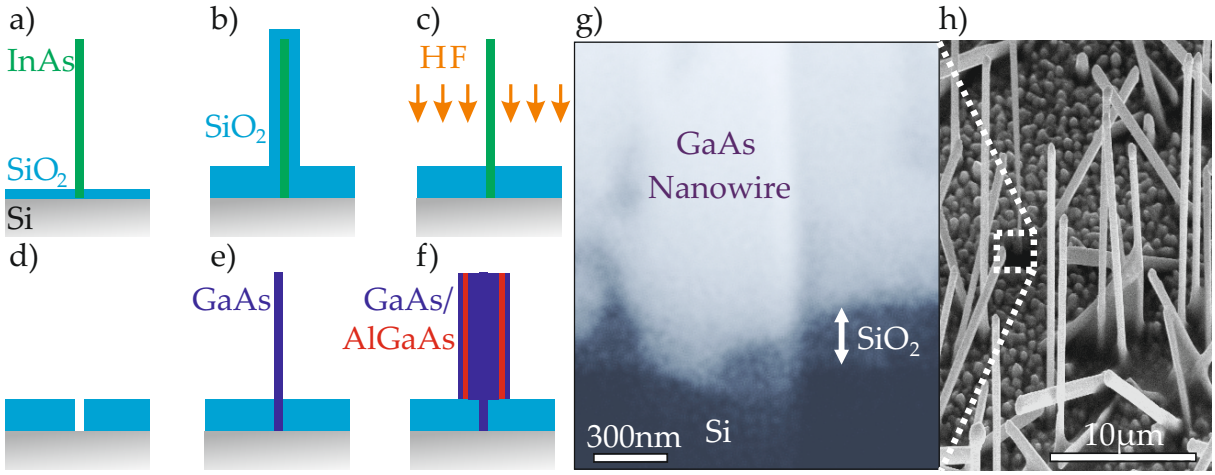

Figure 4.4. *a) Schematic illustration of a sacrificial InAs nanowire on a Si substrate that is covered with a thin SiO_2 layer. b) The InAs nanowire and the substrate is covered with a ∼200 nm thick SiO_2 layer which afterwards c) is removed from the nanowire side facets using HF etching. d) After annealing the InAs nanowires in the MBE chamber, thin nano apertures are formed inside the SiO_2 layer. e) Growth of the GaAs core inside the nano aperture. f) Radial growth of the GaAs-AlGaAs-GaAs nanowire shell. g) Cross-sectional SEM image of the foot of a single GaAs nanowire prepared by focused ion beam milling of the nanowire base of a single wire (left, scale bar 300nm) from h) an ensemble of epitaxially grown nanowires on Si. The nanowire core is clearly connected to the silicon substrate by the thin GaAs core while the main part of the nanowire shell grows above the 250-nm thick SiO_2 interlayer.*

into the MBE system and heated up to 700°C to induce thermal decomposition and complete desorption of the InAs nanowires, leaving behind the desired deep holes in the SiO_2 inter-layer.

The consecutive GaAs nanowire core growth is schematically depicted in Fig. 4.4e) and was performed at 610°C with an As flux of 0.013nm/s and a Ga flux of 0.025nm/s. After 3.5 hours of growth this resulted in ∼14μm long and ∼80nm thick GaAs nanowires, with a vertical growth yield of less than 10%. In the final steps shown in Fig. 4.4f), the temperature was reduced to 450°C and the As flux was increased to 0.19nm/s for GaAs overgrowth of the nanowires up to a diameter of 470nm (blue) which provides waveguiding inside the nanowire region above the SiO_2 inter-layer (see section 4.4.1). Subsequently, an Al flux of 0.057nm/s was supplied to perform ∼10nm-thick AlGaAs shell (red) growth and to passivate non radiative recombination centers at the nanowire surface [67]. The growth is finalized by a 10nm GaAs shell protection layer (blue) to prevent oxidation of the nanowires.

A typical SEM image recorded from a single nanowire grown using this procedure is presented in Fig. 4.4h) showing the ∼14 μm long nanowires with a total diameter of 470±10nm. Moreover, high resolution SEM images recorded from the foot of a single

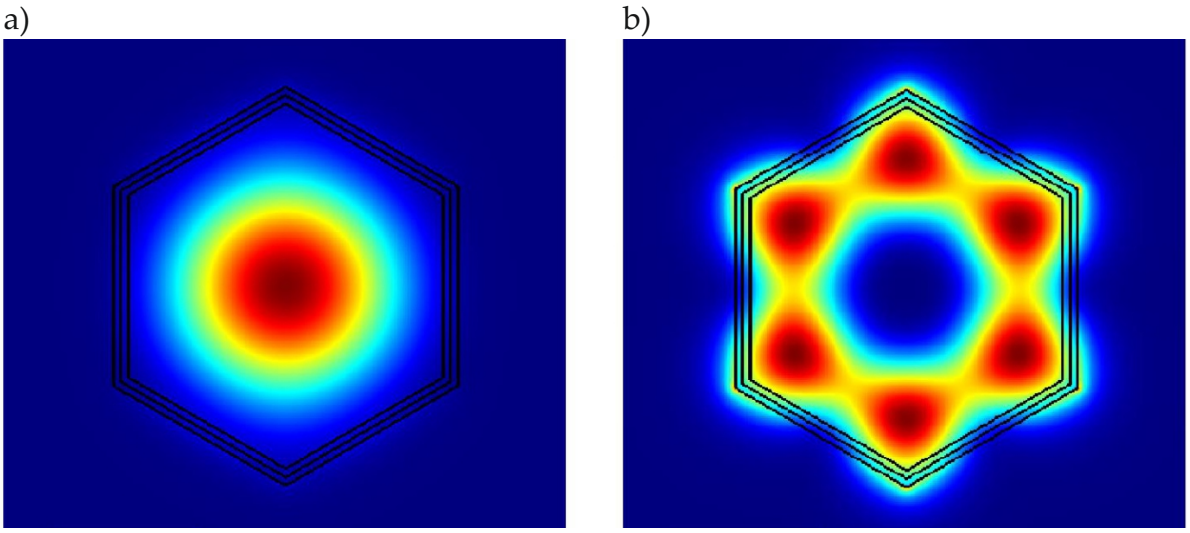

Figure 4.5. *FDTD simulations of a hexagonal GaAs/AlGaAs/GaAs core-shell structure with total diameter of 470nm. The color represents the normalized light Intensity distribution at the nanowire cross section. a) Simulation of the HE_{11} mode. b) Simulation of the HE_{31} mode.*

nanowire that has been exposed by focused ion beam milling (Fig. 4.4g)) confirm that the nanowire core extends through the SiO_2 inter-layer into the Si substrate, as depicted on Fig. 4.1.

4.4 Calculations of the carrier and photon dynamics of nanowire lasers subject to femtosecond pulses

Using the obtained gain function and the parameters of the FDTD simulations, the coupled differential equation 2.6 can be solved for the nanowire laser on silicon. The FDTD analysis of the hexagonal GaAs-AlGaAs core shell nanowires provides two dimensional intensity profiles of various optical modes that correspond to individual solutions of the Helmholtz equations for the given material system. The intensity profiles for the fundamental HE_{11} and HE_{31} modes are presented in Fig. 4.5. The simulations clearly show that both modes strongly overlap with the nanowire gain medium which leads to the high confinement factors Γ presented in Table 4.1.
However, the calculated reflectivities at the nanowire end facets presented in Table 4.1, show that for a diameter of 470nm, the reflectivity of the HE_{31} mode is much higher than for the HE_{11} mode. This strongly reduces the threshold gain and makes HE_{31} mode

Mode	n_{group}	Γ	R_{air}	$R_{SiO_2/Si}$	L	g_{th}
HE_{11}	3.84	1.04	0.45	0.24	20.8μm	516/cm
HE_{31}	4.99	1.26	0.95	0.80	16.1μm	66.5/cm

Table 4.1. *Parameters for the rate equation analysis obtained from FDTD simulations of a nanowire with a diameter of 470nm.*

lasing more preferable. As discussed earlier, the threshold can be calculated using:

$$g_{th} = \frac{1}{2\Gamma L} ln\left(\frac{1}{R_{air} \times R_{SiO_2/Si}}\right), \tag{4.1}$$

where g_{th} denotes the threshold gain, Γ denotes the mode confinement factor, L denotes the nanowire length, R_{air} denotes the reflectivity at the nanowire-air interface and $R_{(siO_2/si)}$ denotes the reflectivity at the nanowire-SiO_2/Si interface [5]. The formula neglects waveguide losses as they play no significant role at the nanowire length scales of a few μm.
The calculated threshold gain serves as an important parameter for the rate equation model presented in the next section. Corresponding values of the threshold gain are given in Table 4.1 for the HE_{11} and HE_{31} modes calculated for a nanowire diameter of 470nm. The mode that provides the lowest threshold gain can be selected by adjusting the nanowire diameter such that optical modes are cut-off or supported according to the desired application [62]. For instance, sufficient reflectivities of $\sim$40% and single mode lasing can be achieved from the HE_{11} mode presented in Fig. 4.5a) using nanowires with diameters < 300 nm, which provides excellent coupling to single mode optical fibers for optical communication applications.
The calculated refractive group index n_{group} for different modes in the nanowire together with the experimentally observed separation of the lasing modes (7.8$\pm$0.1 meV) provides information about the length of the investigated nanowires using equation 2.4. The length of the nanowire calculated for the HE_{11} and the HE_{31} mode are presented in Table 4.1 and are in well agreement with the expected typical nanowire length of $\sim$ 14 μm measured by electron beam microscopy.

Most parameters other than those obtained from the FDTD simulations are taken either from the literatur or from experiments. The spontaneous emission lifetime is set to the intrinsic minimum of GaAs which is τ_{spon}=0.7ns [120]. This is supported by direct measurements of the lifetime of similar GaAs/AlGaAs/GaAs core shell nanowires as transferred to a glass substrate as presented in section 2.6, yielding a lifetime of τ_c=0.68ns. The lifetime of non-radiative recombination in GaAs/AlGaAs nanowires at room-temperature was modeled in Ref. [31] as τ_{NR}=0.48ns, assuming that non-radiative recombinations dominate the carrier relaxation lifetime τ_c and τ_c=$\tau_N R$ [31]. We chose

E_k	τ_{spon}	τ_{SRH}	τ_{exc}	C
23eV	0.7ns	0.69ns	455fs	$1\times10^{-}30cm^6$ / s

Table 4.2. *Parameters used for the rate equation model.*

Varshni Bandgap E_g [eV]	1.508-(5.405 $\times$ $10^{-4}\times$ T^2) / (T+204)
T	20K
m_e	0.067 m_0
m_h	0.22 m_0
N	$1 \times 10^{17}/cm^3$
τ_{eh}	130fs

Table 4.3. *Parameters used in equation 2.10. The table contains the fundamental temperature dependence of the band gap Eg, the electron and hole masses $m_{(e/h)}$ and the carrier density n. The effective hole mass of mh = 0.22m0 lies well within the typical parameters for GaAs which strongly depend on respective crystal directions. Typical literature values range from 0.08 (light hole, <111>, perpendicular) to 0.78 (heavy hole, <111>, perpendicular). However, the influence of hole masses on the calculated beta factor and the theoretical linewidth are small. The actual lattice temperature T used in the quasi-thermal carrier distribution functions, and electron-hole pair formation time τ_{eh} are determined from the fit to the experiment shown in Fig. 2.7.*

the non-radiative lifetime from Shockley-Reed-Hall recombinations τ_{SRH}=0.69ns, close to the measured value τ_c=0.68ns at ∼10K. The value for the Auger-recombination constant C is taken from literature [121]. The refractive index n_{refr} of the gain material and the threshold gain g_{th} are taken from the FDTD simulations for the HE_{31} nanowire mode, see the previous section and Table 4.1. E_k is the Kane Energy for GaAs taken from the literature [122] and is presented together with constants used for the rate equation model in Table 4.2.

As the spontaneous emission peaks at ∼1.51 eV, Fig. 2.8 clearly shows that a carrier concentration of $\sim3\times10^{16}$ is needed to reach transparency at this particular photon energy. The lasing threshold of 66.5/cm calculated for the HE_{31} mode as given in Table 4.1 should be reached for carrier concentrations of $\sim5\times10^{16}/cm^3$.

The parameters obtained from the FDTD simulations can now be used for further calculations that provide insights into the photon and carrier dynamics of nanowire lasers under optical excitation. The spontaneous emission coupling factor β is used as fit parameter to determine the fraction of the total spontaneous emission that is coupled into the laser mode, and the jump from below to above threshold in the input/output

curve, as presented in this chapter in section 4.5. The differential equation 2.6 was calculated using an ordinary differential equation solver (ODE15s) algorithm provided by the MATLAB software, as presented in chapter 2. The results for the time dependent photon density and time dependent charge density inside the nanowire laser are shown in Fig. 4.6. The calculations are presented for three different pump powers ranging from the spontaneous emission regime (black curves) to excitation above the lasing threshold (red curve) and far in the lasing regime (blue curve).
The results clearly show that for excitation below the lasing threshold, the photon and carrier dynamics take place on timescales of $\sim$ 1ns, reflecting the spontaneous emission and non radiative decay channels of the laser system. Above threshold however, the carrier concentrations are rapidly converted to a high photon density by stimulated emission. Interestingly, the temporal dynamics become faster if the excitation power is increased. Therefore, the duration of the nanowire pulse strongly decreases with increasing excitation power and reduces the temporal emission down to $\sim$3 ps for P/P_{th} $\sim$4.

The photon density as a function of time $S(t)$ obtained from the differential equations can be Fourier transformed into the frequency domain $S(\omega)$ to obtain the theoretical spectral intensity of the nanowire emission. The theoretical spectra and their peak intensities as a function of excitation power can now be evaluated and compared to experimental data.

4.5 Optical characterization of nanowire lasers on silicon

We characterized the lasing performance of our nanowires using low temperature confocal spectroscopy. Figure 4.7 illustrates the experimental setup used for the photoluminescence measurements and measurements of the second order correlation function of nanowire lasers in a top-excitation side-detection geometry. The measurements were performed in a He-flow cryostat using a pulsed Ti:Sa laser emitting at $\sim$780nm that delivered 455fs duration pulses onto the sample at a repetition frequency of 82MHz. The excitation laser path passes a shortpass filter to block residual laser emission at the detection wavelength and is guided through a beamsplitter to separate the excitation- (green) from the detection path (red). After the beamsplitter, a fraction of the excitation beam is collected by a powermeter as a reference for the excitation power. The actual excitation beam is guided to a 0.55NA Objective (top-objective) that optically excites the nanowire along a direction parallel to the sample surface (see the inset in Fig. 4.9). The emission is detected in an orthogonal geometry along parallel to the sample surface using a second NA=0.5 objective outside the cryostat (see the inset in Fig. 4.9). The excitation laser was defocused onto the nanowire side facet in order to obtain the strongest emission in the lasing regime in order to obtain homogeneous gain throughout the nanowire. The excitation spot size used here is estimated to be $\sim 9 \pm 2 \mu$m. The detection signal is focused onto a single mode optical fiber which guides the collected light to the

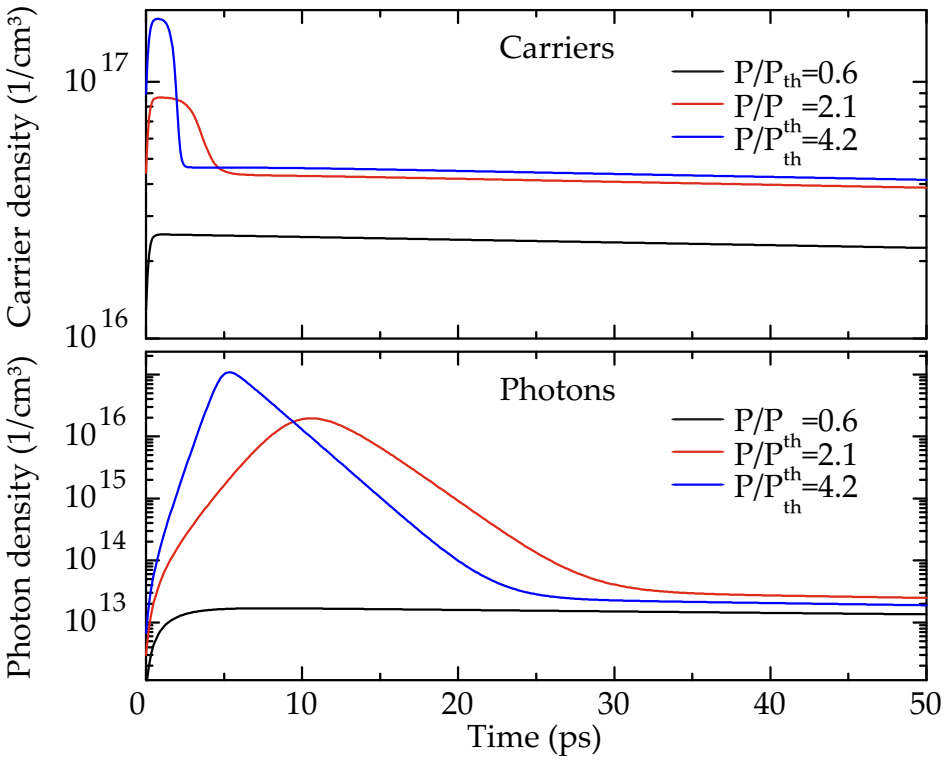

Figure 4.6. *The image on the top shows the calculated carrier density in the nanowire laser as a function of time for three different excitation powers below (black line) and above threshold (red and blue line). The image on the bottom shows the calculated photon density in the nanowire laser as a function of time for three different excitation powers below (black line) and above threshold (red and blue line).*

spectrometer. After passing the optical grating in the spectrometer, the diffracted signal can either be focused on a CCD camera or guided to a Hanburry-Brown-Twiss (HBT) setup via a flipable mirror and the spectrometer side exit. The HBT setup consists of a beamsplitter that separates the signal beam into two path, two single photon avalanche detectors (SPAD) that detect the light from the two paths and an electrical readout of the detectors. The sample can be illuminated by a white light source and imaged by a CCD camera. The white light path and the imaging camera path are separated by another beamsplitter. The nanowire luminescence can be directly recorded by the imaging camera using a longpass filter in front of the imaging camera which suppresses the excitation laser.

Figure 4.8 a) presents an optical microscope image of nanowires close to the sample edge recorded using the same geometry as used to excite nanowires in the optical setup. Figure 4.8 b) shows nanowire luminescence recorded from the imaging system of the optical setup using a longpass filter in front of the imaging camera to suppress the excitation laser. The luminesce from the top- and bottom-facets of the nanowire is clear evidence for waveguiding and light recirculation inside the nanowire on silicon. The

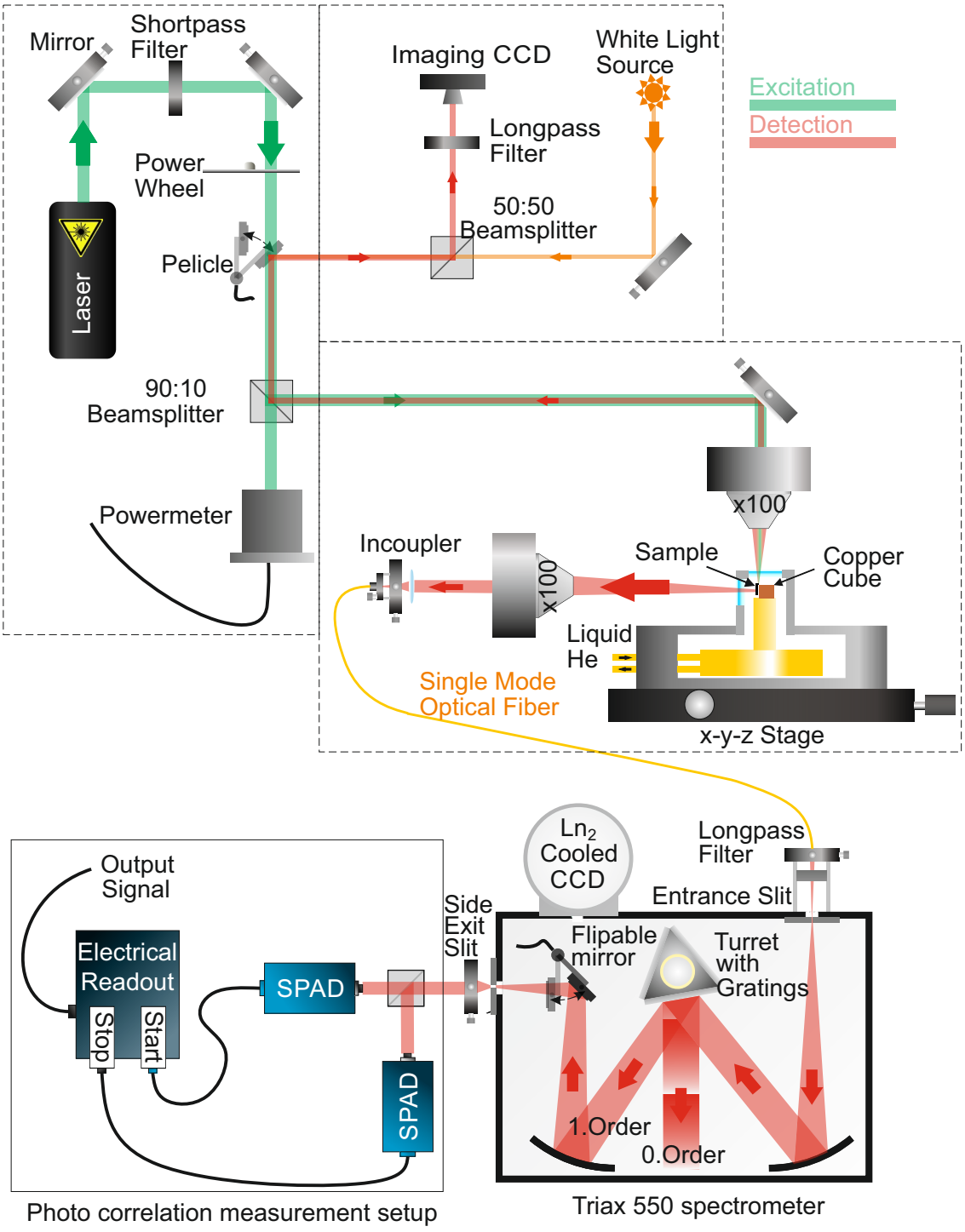

Figure 4.7. *Schematic illustration of the optical Setup used for photoluminescence measurements of a nanowire laser on Si in a top-excitation side- detection geometry. The optical setup includes two single photon detectors used for Hanburry-Brown-Twiss (HBT) measurements of the second order autocorrelation function of the nanowire.*

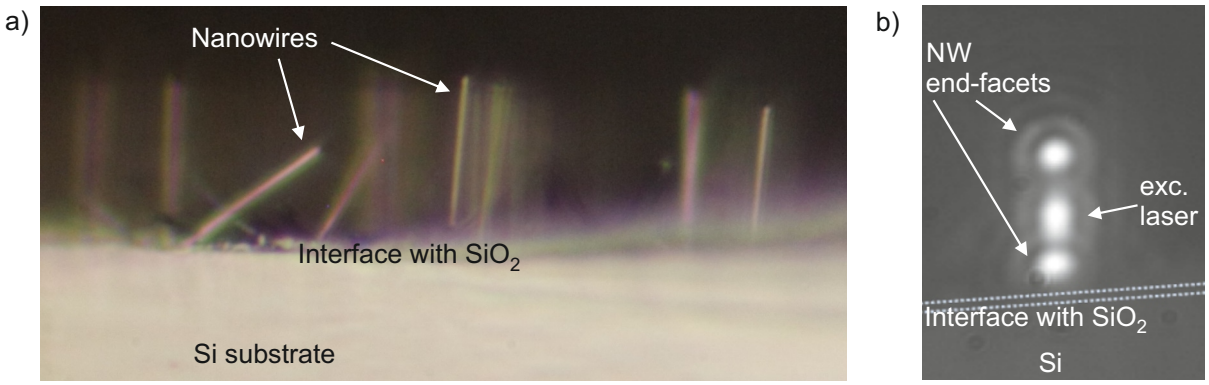

Figure 4.8. *a) Optical microscope image of typical GaAs/AlGaAs nanowires on silicon grown by the sacrificial-wire technique presented in section 4.3. Typical nanowire lengths are ∼ 14 µm. b) Image of the luminescence of an optically pumped nanowire on silicon recorded using the imaging camera in combination with a longpass filter to block the excitation laser. The nanowire length L=16.1µm was calculated using equation 2.4, the calculated refractive group index of the HE_31 mode (n_{group}=4.99) and the spacing of the Fabry-Perot modes presented in the photoluminescence spectra in Fig. 4.9.*

luminescence from the center of the nanowire was used to estimate the excitation spot size including the carrier diffusion in the nanowire of $\sim 9 \pm 2 \mu$m by referencing it to the nanowire length L. The unordered distribution and large number of nanowires on the sample as shown in Fig. 4.8 rendered a re-identification after the optical experiments of the nanowire laser presented in 4.8 b) impossible. The nanowire length L=16.1μm was calculated using equation 2.4, the calculated refractive group index of the HE_31 mode (n_{group}=4.99) and the spacing of the Fabry-Perot modes presented in the photoluminescence spectra in Fig. 4.9. Figure 4.9 shows emission spectra obtained from the single nanowire presented in 4.8 b). The measurements were performed at 10 K with continuous wave equivalent excitation powers (P) ranging from 600μW (black curve) to 3.7mW (red curve). At low excitation levels the broad spontaneous emission spectrum is modulated by the Fabry-Prot (FP) longitudinal modes of low order waveguide modes supported by the nanowire cavity (see section 4.4.1) [32][123].
With increasing excitation levels, a strong peak emerges from one of the FP modes at 1.505eV accompanied by a sudden reduction of the linewidth to 0.3meV, as shown by the green data points in Fig. 4.9. After the excitation level reaches a threshold of P_{th}=873$\pm$87μW ($\equiv$11$\pm$1 pJ / pulse), the output intensity increases nonlinearly and the spectrally broad spontaneous emission background saturates.
Finally, for excitation levels beyond $\sim 2 \times P/P_{th}$ the output increases close to linearly with the pump power (see section 2.4). The observation of the broad amplified spontaneous emission (ASE) transition region is characteristic for lasers with a large spontaneous emission coupling [124][32], as discussed in chapter 2. Finally, for the highest excitation level exceeding $2.5 \times P/P_{th}$, a second lasing peak reaches threshold and emerges at

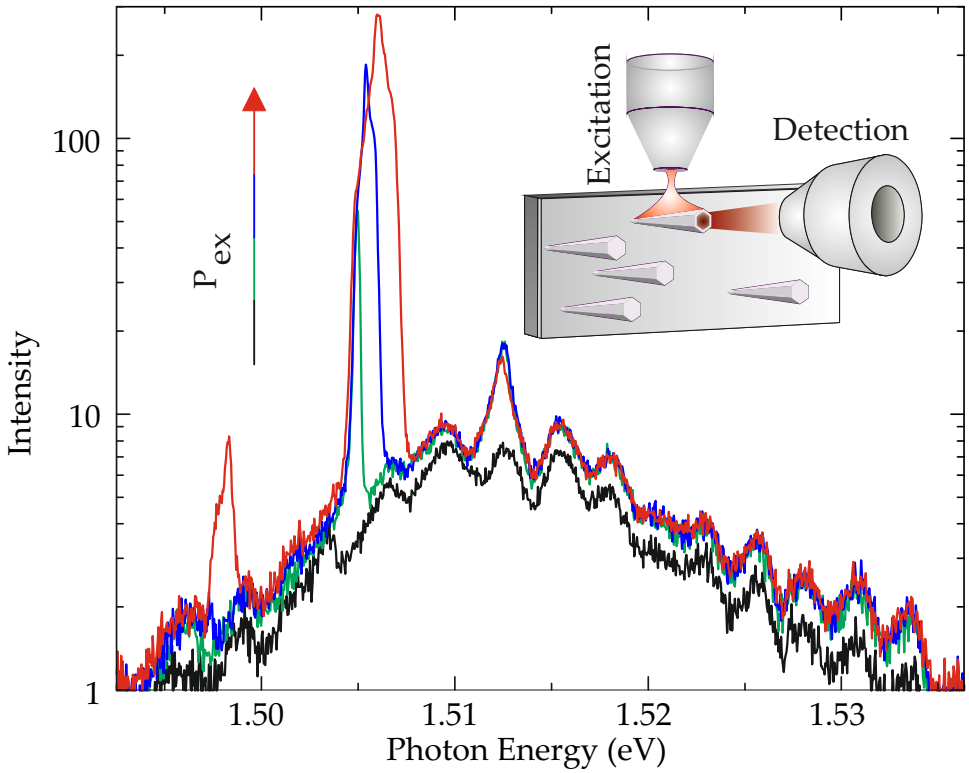

Figure 4.9. *Typical emission spectra recorded from an optically pumped GaAs nanowire laser on silicon excited from the side and detected perpendicular to the sample surface at 10 K. Data is shown for excitation levels of P/P_{th}=0.7 (black), P/P_{th}=1.5 (green), P/P_{th}=2.5 (blue) and P/P_{th}=4.2 (red), respectively. The inset depicts schematically the measurement geometry.*

1.498 eV as shown in Fig. 4.9.
The increase of the nanowire laser peak is accompanied by a blue shift of the peak position that we attribute to an increase of the accessible gain for higher excitation powers which can also lead to deviations from a perfectly linear slope of the input-output curve in the lasing regime. We emphasize that the spontaneous emission clamping observed for the nanowire lasers subject to fs-pulsed excitation must be distinguished from the gain clamping that occurs in continuous wave lasers as presented in chapter 3. Although the spontaneous emission saturates at high excitation powers, the blueshift of the lasing peak provides evidence for the absence of gain clamping. This can be explained by the ultrafast dynamics of the nanowire laser subject to fs-pulsed excitation as described in detail in section 5. In section 5, we demonstrate that between the nanowire excitation and the nanowire pulse emission (t_on), the lasing state can be almost fully occupied before depopulation by stimulated emission starts. During t_{on}, the gain does not clamp as the carrier population of the lasing state can increase with increasing excitation power until the nanowire laser pulse is emitted. Consequently, higher energy states can be populated (see chapter 5 Fig. 5.6), leading to accessible gain at higher energy lasing

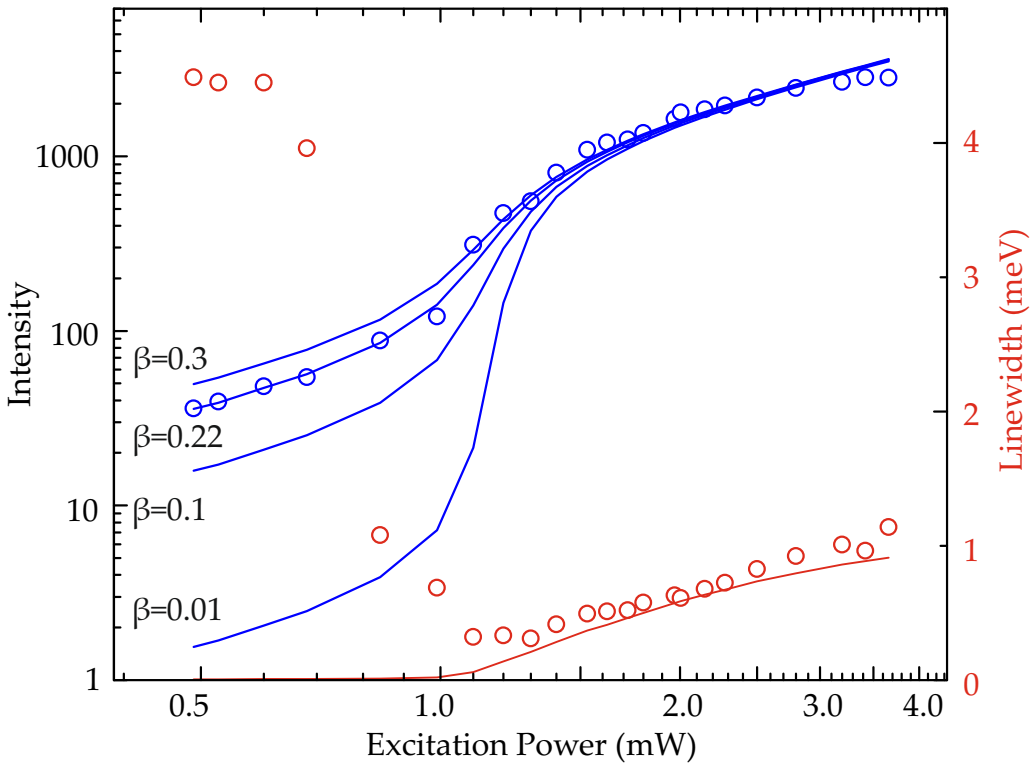

Figure 4.10. *Nanowire laser peak intensity (blue points) and corresponding linewidth (red points) as a function of excitation power together with simulated S-shaped input-output curves for different β-factors (blue curves) and the theoretical linewidth (red curve).*

states. The broad FP-modes (FWHM=4meV) corresponding to the low Q cavity (Q=375 for loaded case, Q=519 for unloaded case of HE_{11} mode) provide the coupling of blue shifted emission to the nanowire cavity. This finally causes a blue shift of the peak energy (Fig. 4.9) of the nanowire laser as observed in previous work [125][72]. In contrast, after the nanowire laser pulse has ceased (t_{pulse} ∼10ps), the carrier population clamps around transparency (see chapter 5 Fig. 5.6). As the spontaneous emission lifetime in the GaAs/AlGaAs nanowires is ∼1ns (as described in chapter 2 Fig. 2.14), spontaneous emission takes place predominantly after the clamping of the lasing state occupation to inversion and, therefore, saturates at high excitation powers.

Further analysis of the input-output characteristics recorded from the nanowire presented in Fig. 4.8 b) facilitates determination of the spontaneous emission coupling efficiency (β-factor). The blue data points in Fig. 4.10 show the emitted intensity versus the excitation power exhibiting a weak threshold at 873±87μW. To analyze this data we use a rate equation model to simulate the photon and carrier dynamics for different excitation powers (see section 4.4.2 and Fig. 4.12b)). Key quantities are the gain function and modal reflectivity of the cavity mode as obtained from literature data and FDTD calculations (see section 4.4). Typical fits to the measured input-output curve are presented in Fig.

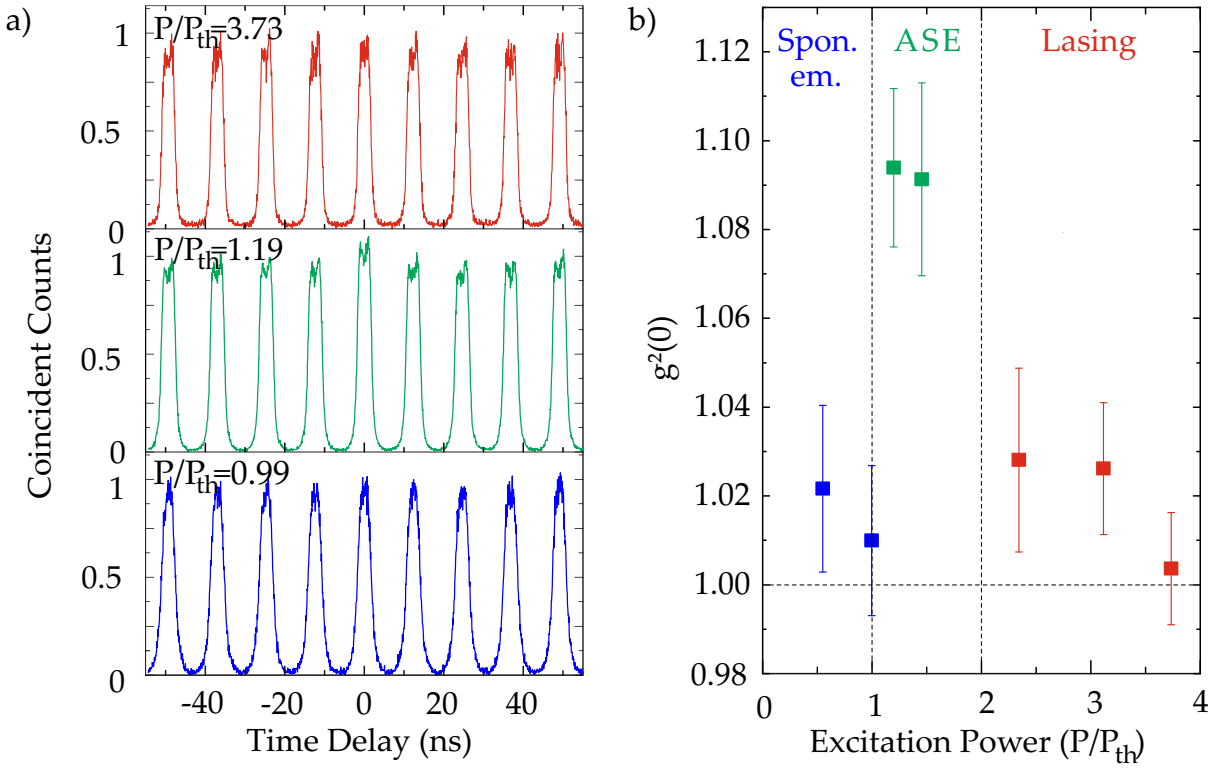

Figure 4.11. *HBT measurements of a nanowire laser for different excitation powers ranging from spontaneous emission (blue) to ASE (green) and lasing (red). (a) Normalised coincidence counts as a function of time delay for three different excitation powers. (b) Normalised second-order photon correlation function at zero time delay as a function of the excitation power.*

4.10 for β-factors ranging from 0.01 to 0.3 (blue curves). The best fit to the experimental data is obtained using β=0.22 demonstrating that a remarkably large fraction of the emitted radiation couples to the lasing mode. The β-factor is several orders of magnitude larger than for conventional DFB lasers [55], one order of magnitude higher than the spontaneous emission factor found for helical modes in nanopillar lasers (17) and comparable to photonic crystal nanocavity and micropillar lasers [126][58][127]. We ascribe the high β factor to the scarcity of optical modes available close to the gain maximum [31][88].

4.6 Power dependence of the quantum statistics of photons from nanowire lasers on silicon

The picture of the transition from spontaneous emission, to ASE and finally lasing operation can be further confirmed by measurements of the second order correlation function

$g^{(2)}$ (0) as a function of excitation level, as seen in Fig. 4.11. Here, as described in the previous section, we employed standard HBT measurements using two single photon detectors with a time resolution of >250ps. For excitation powers in the spontaneous emission regime, the recorded photoluminescence stems from the radiative recombination of many (several hundred) different excitons in the nanowire presented in Fig. 4.8 b)). The phase of each of the emitters exhibits jumps and discontinuities and also the number of emitters fluctuates with time, leading to intensity fluctuations at timescales in the order of the coherence time τ_c [128]. Therefore, light from such a source can be described as chaotic due to the randomness of the emission processes at the macroscopic level [128]. The time dependent intensity of such a source on a detector I(t) can be written as: $I(t)=\langle I\rangle + \Delta I(t)$, where $\Delta I(t)$ denotes the time dependent intensity fluctuations [128]. Using a 50:50 beamsplitter providing equal intensities on both detectors, the output of the HBT measurement is proportional to: $\langle \Delta I(t)\rangle \Delta I(t+\tau_{12})$, with τ_{12} being the time delay between detector D1 and detector D2 [128]. Although $\langle \Delta\, I(t)\rangle=0$ by definition, the output of the HBT setup at $\tau_{12}=0$ is $\langle \Delta\, I(t)^2>0$, and therefore, non-zero in the case of chaotic light [128]. In contrast, in the case of a perfectly stable and coherent laser source, the intensity fluctuations $\Delta I(t)$ should reduce to zero $\Delta I(t)=0$, resulting in a zero output of the HBT measurement $\langle \Delta I(t)^2=0$. This results can be quantified by the second order correlation function

$$g^{(2)}(\tau_{12}) = \frac{\langle I(t)I(t+\tau)\rangle}{\langle I(t)\rangle\langle I(t+\tau)\rangle} \tag{4.2}$$

, evaluated at zero time delay $\tau_{12}=0$ [128]. Therefore, in the spontaneous emission regime of the nanowire laser, photon bunching with $g^{(2)}$ (0)=2 is expected at zero time delay, reflecting the thermal nature of the emitted light. At high excitation, the coherent lasing regime is characterized by $g^{(2)}(0)=1$ and an increase in the coherence time of the emission [129]. However, both regimes are typically difficult to access experimentally due to the limited time resolution of the photo-detectors.

In our measurements, in the spontaneous-emission regime, $\bar{g}^{(2)}$ (0)-values close to 1 are observed (blue data points in Fig. 4.11b), since the coherence time of the emission is much shorter than the time resolution of the detection, and fluctuations due to photon bunching on shorter time scales are averaged out [126]. For intermediate excitation powers in the ASE regime, we observe an increase in coherence time (green data points), which is an indicator for approaching the threshold and typically accompanied by an increasingly Poissonian character of the emission [129]. Finally, when the excitation power exceeds $2P_{th}$, $\bar{g}^{(2)}(0)$ takes on values close to unity again indicating a clear transition to lasing. As we will further show below in Fig. 4.12, this regime is also characterized by a significant decrease in the pulse length of the emission. Since the coherence length cannot exceed the pulse length of the emission, i.e. below 10ps, the measurement does not allow distinguishing between an averaging effect due to the limited resolution of the detector, and the signature of coherent emission. This is in contrast to experiments that show the same behavior, but are performed under continuous wave excitation [126][58]: There, the coherence length in the lasing regime becomes larger than the

detector resolution and is not limited by the emission time, and $g^{(2)}$ (0) can be fully resolved. Nevertheless, the decrease of the duration of the nanowire emission as well as the change of the photon statistics are both clear signatures of the transition to lasing operation. From this, we conclude that the decrease of the measured $\bar{g}^{(2)}(0)$ values above P/P_{th}=1 indeed reflects the transition from thermal to coherent emission and thus proves lasing behavior.

4.7 Ultrafast pulse emission and homogeneous linewidth broadening from nanowire lasers on Si

The pulsed excitation scheme coupled with the rate equation model described in section 4.4.2 facilitates analysis of the dynamical performance of the high-β nanowire-laser. The investigated nanowire is presented in Fig. 4.8 b). Experimentally, the linewidth of the nanowire laser emission is found to increase towards high excitation levels above P/P_{th}=1.5 as can be seen in Fig. 4.12c) (red curve and data points). Both the input-output curve (blue curve - Fig. 4.10) and linewidth of the laser peak above threshold (red curve - Fig. 4.10 are in excellent agreement with the predictions of the simulations presented in section 4.5.

We identify the increase of the linewidth as arising from faster stimulated emission dynamics in the strong excitation regime as supported by the results of the rate equation model presented in Fig. 4.6. Hereby, the higher excitation power reduces the pulse width of the nanowire laser leading to an increase of the emission linewidth [130].

The Fourier Transform of the time dependent photon density as presented in Fig. 4.12a) provides the theoretical spectral emission profile of the nanowire laser calculated from the rate equation model presented in section 2.3. The theoretical data in the frequency space can then be directly compared to the experimental spectra of the nanowire lasers. Assuming Fourier limited pulse emission of the nanowire laser, the linewidth broadening as a function of the excitation level should be given by the time-bandwidth product according to $\Delta\lambda=\frac{K\times\lambda^2}{c\tau}$, where λ is the central wavelength, c is the speed of light, K is a constant prefactor that depends on the excitation pulse form (K of a Gaussian pulse shape = 0.44) and $\Delta\lambda$ represents the nanowire laser linewidth. We determined K of the nanowire lasers by Fourier transforming the temporal form of the photon density as shown in an example for an excitation power of P/P_{th}=4.2 in Fig. 4.12. Relating the obtained FWHM of the spectral signal to the FWHM of the temporal emission profile we can directly determine the K-factor to be K=0.69$\pm$0.04, which represents a characteristic value for the nanowire laser pulse shape.

Furthermore, the time bandwidth product can now be used to determine the temporal nanowire laser pulse width τ from the measured spectral linewidth $\Delta\lambda$. The result for the experimental (red data points) and theoretical (blue curve) temporal nanowire laser pulse width as a function of excitation power is shown in Fig. 4.12b). Here, again, the pulse width determined from the nanowire laser linewidth is in excellent quantitative

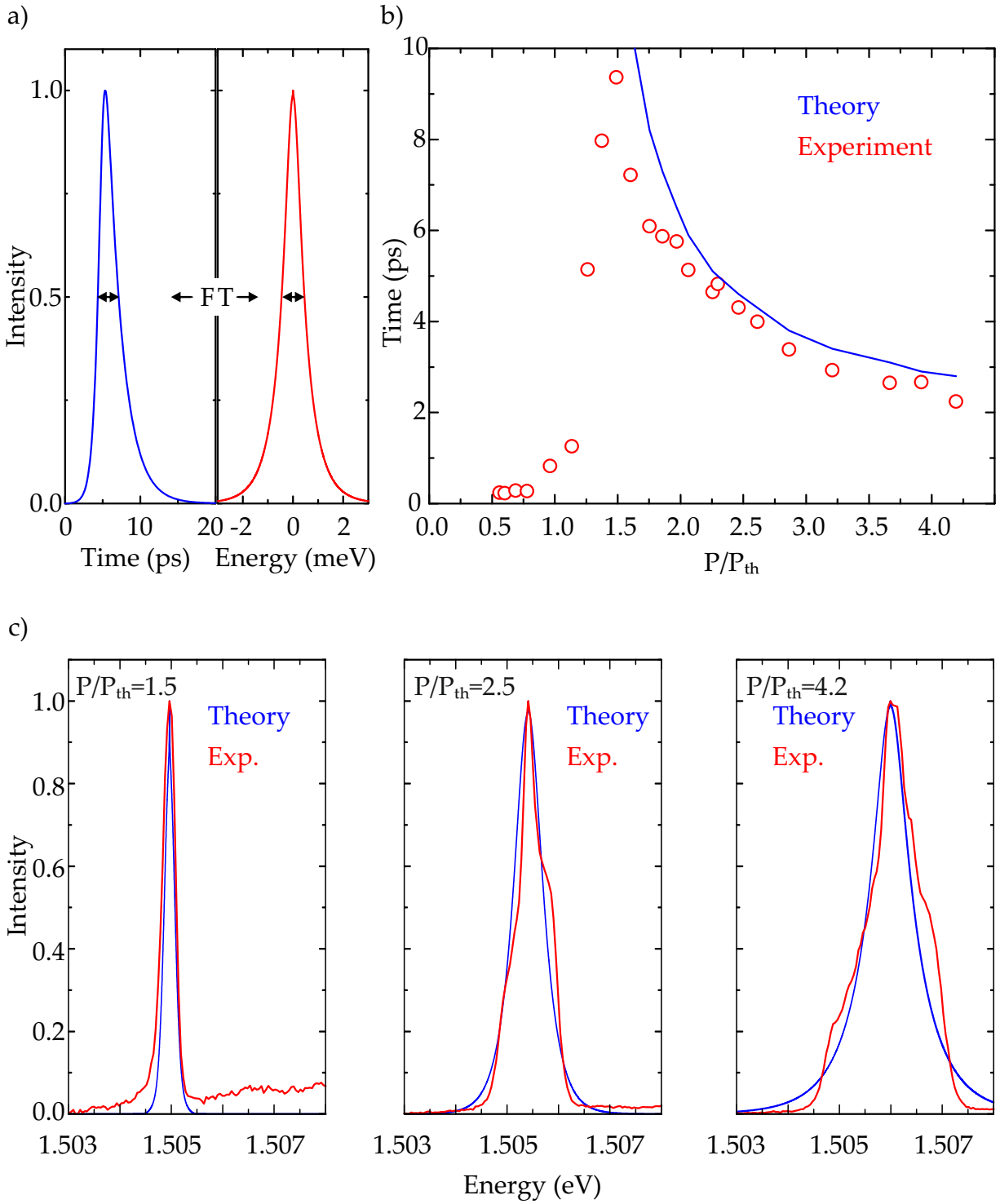

Figure 4.12. *a) Normalized temporal (left image) and spectral (right image) emission of the nanowire laser for an excitation of P/P_{th}=4.2. The spectral emission (right image) is obtained from the Fourier transform of the temporal emission calculated from the rate equation model (left image). b) Measured pulse width determined from the nanowire laser linewidth (red data points) as a function of excitation power together with the theoretical nanowire laser pulse width calculated from the rate equation model (red). c) nanowire laser spectra for 3 different excitation powers measured in the experiment (red curves) and calculated from the FT of the rate equation model (blue curves).*

agreement with the theoretical predictions and reduces with increasing excitation power above threshold.
The raw data of the measured time integrated nanowire laser spectra are shown by the black spectra in Fig. 4.12c) together with the calculated emission spectra (colored curves). The excellent agreement of the theoretical and experimental spectra strongly indicates that the linewidth broadening is close to the Fourier limit [130]. Interestingly, the experimental nanowire laser spectra exhibit small oscillations that slightly deviate from the theoretical data. As will be explained in the following chapter, this oscillations can be attributed to the spectral signatures of coherent Rabi oscillations inside the nanowire during pulse emission.
Remarkably, the shortest pulse emitted by the nanowire laser is predicted by our simulations to be $\sim$3ps in good accord with the measured value of 2.5$\pm$0.2ps for an excitation level of P/P_{th}= 4.2. Note, such ultrafast dynamics close to the Fourier limit have previously been also observed in other nanowire systems [66]. The ultrafast emission behavior can be attributed to the low-Q of the nanowire resonator (Q as low as Q$\sim$400 for the loaded case and Q$\sim$500 for the unloaded case for e.g. the HE_{11} mode) and the small cavity size that leads to an ultrafast decay of the photon population inside the nanowire cavity within a few picoseconds. Thus, the monolithic integrated nanowire laser demonstrated is shown to be capable of pulsed emission down to 2.5$\pm$0.2ps corresponding potential repetition rates in excess of $\sim$250GHz.

4.8 Summary

In summary, we demonstrated a GaAs-AlGaAs high-β nanowire laser monolithically integrated on silicon emitting in the near infra-red. Using low temperature confocal spectroscopy, lasing was confirmed via the observation of a characteristic s-shaped input-output curve accompanied by a strong linewidth reduction.
Further confirmation of the transition from spontaneous emission to lasing operation is obtained by measuring the quantum statistics of the nanowire emission exhibits a clear reduction of the measured second order correlation function ($g^{(2)}(0)$) with increasing excitation powers in the lasing regime.
A low threshold pump power of only 11$\pm$1 pJ / pulse was obtained and a remarkably high spontaneous emission coupling factor of β=22% was determined. By comparing the measured input-output characteristics and laser linewidth with a coupled rate equation analysis we obtained evidence for ultrafast pulse emission down to 2.5 ps.
The methods and approaches used in our experiments open the way towards highly efficient coherent on-chip light sources on silicon. Furthermore, since the nanowire-lasers are in direct contact to the substrate, radially doped nanowire hetero-structures in combination with the dielectric reflection layer could be used to fabricate electrically driven nanowire lasers operating on silicon.

5

Long-term mutual phase locking of picosecond pulse pairs generated by a semiconductor nanowire laser

The previous chapters presented continuous wave lasing and pulsed operation of nanowire lasers as well as their monolithic integration onto silicon. However, besides conventional pulsed and continuous wave emission, an exciting new technology has recently entered photonics research and industry. Although the combination of long-term phase stability and ultrashort pulse emission might seem contradictory, coherent pulse trains can now be realized by virtue of mode locked laser systems [131]. This technology also enabled the generation and phase stabilization of frequency combs which was awarded with the Nobel prize for Theodor Hänsch, Roy J. Glauber and John L. Hall in 2005.

Today, high-performance lasers that emit phase coherent pulse-trains have become an invaluable work horse in photonics research and industry. Their ability to pass on phase information between subsequent laser pulses enables unique temporal and spectral emission characteristics that constitutes the basis of various fields such as precision metrology [132] and spectroscopy [131][133][134][135].

The consequent drive towards the miniaturization of mode locked lasers systems could hold the promise to realize nanoscale frequency comb sources and ultrafast multichannel transmitters for on-chip and fiber communication or coherent optical control of quantum systems directly on a microchip [135]. However, the complexity and diversity of material compositions needed to fabricate mode-locked lasers has, to date, prevented their realization at the nano-scale [44].

In contrast, non-linear resonators can be downsized to a few tens of micrometers and have been shown to emit octave spanning frequency combs that cover the entire spectral range from the visible to the infrared [136][137]. However, the resonator material does typically not provide optical gain, making external laser sources and their integration on microchips essential for fully on-chip solutions.

In these respects, semiconductor nanowires are of particular interest since they represent the ultimate limit of downscaling for photonic lasers with dielectric resonators [42]. By virtue of their unique one-dimensional geometry nanowire-lasers provide ultra-high modal gain, support low-loss guided modes and facilitate low threshold lasing tunable

across the UV, visible and near infra-red spectra regions [138][31][32][115]. Recently, optically pumped nanowire lasers have been demonstrated at room temperature and they can now be site-selectively integrated onto silicon substrates [39][35]. While the fundamental carrier relaxation and gain dynamics of nanowire-lasers have been very recently explored [138][66], demonstrating the capability of nanowire lasers for ultrafast pulse emission even below the diffraction limit [66], the coherent dynamics have hitherto received comparatively little attention.
In this chapter we demonstrate that GaAs-AlGaAs core-shell nanowire lasers transmit coherent phase information among subsequently emitted laser pulses. Two-pulse interference that emerges within the homogeneously broadened nanowire laser line recorded in time integrated measurements show that the optical phase is preserved over timescales that are $\geq$10 longer than the emitted pulse duration. In particular, the nanowires emit coherent pairs of ultrafast pulses with durations <2ps temporally separated by >30ps when subject to 250fs pulsed excitation. This mutual coherence between two nanowire laser pulses leads to the generation of Ramsey Combs within the homogeneously broadened nanowire laser line that exhibits fringe separations, and consequently, pulse repetition rates >200GHz.
Theoretical calculations obtained from a Bloch equation model are in good agreement with experimental data. The results clearly reveal how light matter interaction in the nanowire laser constitutes a novel mechanism for optical information storage and frequency comb generation at ultrafast timescales at the nano scale. The mutual phase locking is shown to be linked to coherent dynamics that occur in the post-lasing regime when the system remains close to transparency over timescales approaching the spontaneous emission lifetime.

5.1 Ultrafast pump-probe spectroscopy of nanowire lasers

To study the ultrafast emission and coherence properties of the nanowire lasers, we performed time resolved pump-probe spectroscopy with non-resonant excitation. Figure 5.1 shows a schematic illustration of the ultrafast-pump probe spectroscopy setup. A first excitation pulse (blue) from a mode-locked Ti:Sa laser is split into two individual pulses at beamsplitter BS1 which continue to travel in perpendicular directions. The length of one of the optical path is adjusted using a delay stage with a precision of <1μm. Afterwards, a second beamsplitter BS2 guides the two pulses to a mutual optical path and towards the sample. Thus, the time delay $\Delta\tau$ between the two pulses can be precisely adjusted by the delay stage and is given by the optical path difference Δx between the two pulses according to $\Delta\tau$=Δx/c. Both pulses pass a third beam splitter which separates the excitation (blue line) from the detection path (red line). Finally, an optical microscope objective focuses the excitation pulses onto a single nanowire.
The structures investigated are GaAs-AlGaAs core-shell nanowires grown using solid-source molecular beam epitaxy on silicon substrates [32]. After growth, individual nanowires were mechanically removed from the growth substrate and dispersed onto

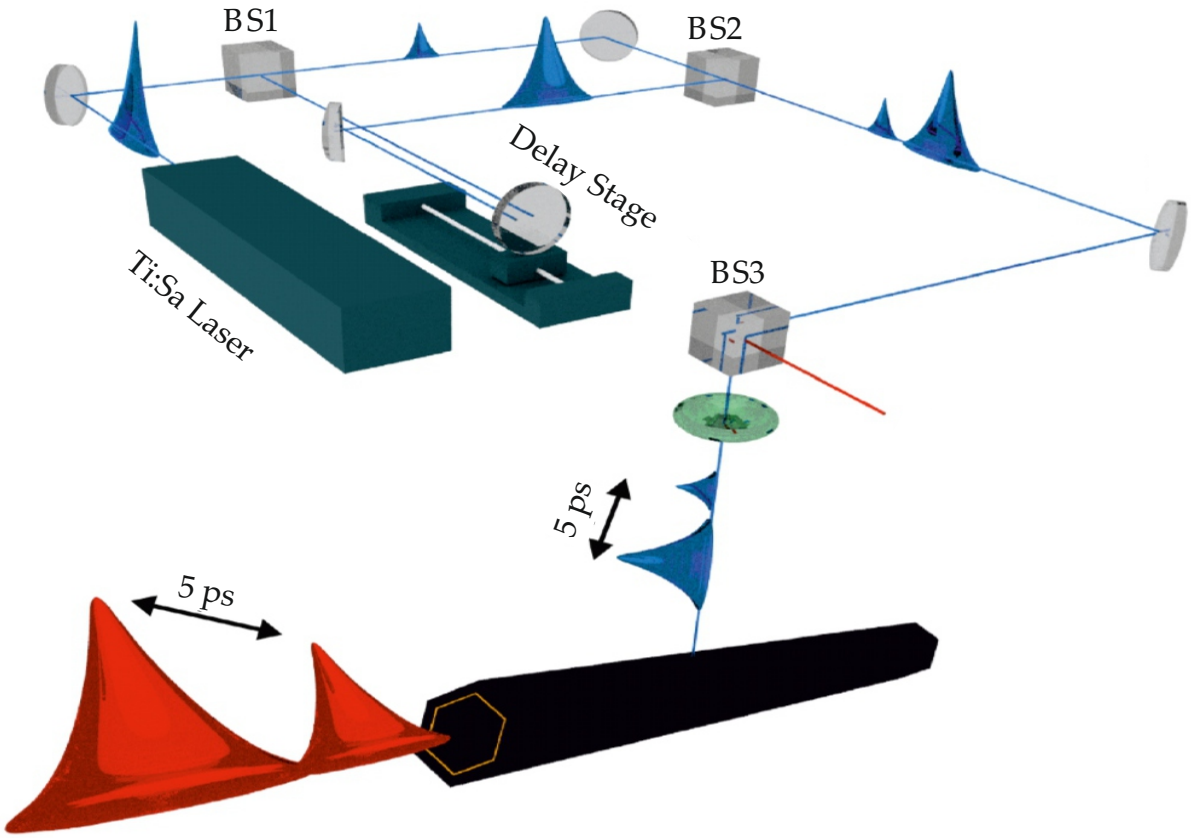

Figure 5.1. *Schematic illustration of an ultrafast pump-probe spectroscopy setup.*

glass whereupon the lasing behavior of individual nanowires could be explored when subject to optical pumping [31][32]. Hereby, the nanowire-lasers were excited at low temperature (20K) using ∼250fs duration laser pulses at a repetition frequency of 80MHz tuned to selectively excite the active GaAs-core region of the nanowire non-resonantly at $\hbar\omega_{exc}$=1.59eV [32]. The temporal separation between pump and probe was precisely tunable over the range $\Delta t = \pm 100$ ps using an optical delay line that provides a relative precision better than ∼10 fs and the experimental observable was the time integrated emission spectrum averaged over $\geq 10^6$ pump-probe excitation pulse pairs.

5.2 Nanowire laser characterization under single pulse excitation

In order to experimentally determine the lasing threshold of the studied nanowire lasers and characterize their optical properties, we first perform single pulse excitation

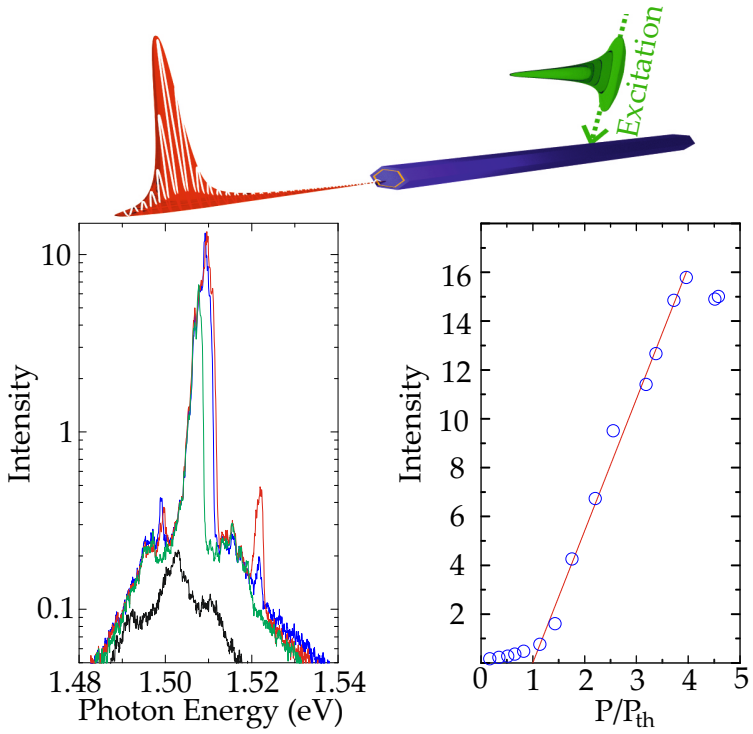

Figure 5.2. *Nanowire-laser output for single pulse excitation with a non-resonant pump pulse as depicted schematically at the top of the figure. The spectra in the leftmost panel shows selected spectra recorded with P/P_{th}=0.6 (black curve), P/P_{th}=1.9 (green curve), P/P_{th}=4.7 (blue curve) and P/P_{th}=5.3 (red curve). The rightmost panel shows the characteristic Input-Output curve obtained from the nanowire-laser together with the linear fit (red curve) used to determine the lasing threshold.*

and power dependent photoluminscence spectroscopy of the nanowires. Figure 5.2 shows selected spectra of the optical response of a nanowire laser subject to either only what will be used as the pump pulse (red) or only the probe pulse (black, green and blue) for different excitation powers while the probe path or the pump path is blocked, respectively. The excitation powers are normalised to the nanowire laser threshold pump level (P_{th}) and are, thereby, presented in units of P/P_{th} throughout this chapter. The probe pulse power is adjusted such that the response of the nanowire subject to only the probe pulse is either in the lasing regime (blue, P_{th}=4.7), the amplified spontaneous emission (ASE) regime (green, P_{th}=1.9) or the spontaneous emission (SE) regime (black, P_{probe}=0.6) while the pump pulse remains in the lasing regime (red) during our experiments ($3<P_{pump}<5.5$). The three regimes and the laser threshold are determined as depicted by the red line in the characteristic Input-Output curve in 5.2b), by interpolating the data points with increasing intensity after the distinct kink down to the x-axis. Typically, a threshold pulse energy of P_{th} $\sim$9 pJ per pulse is required to achieve lasing operation of the nanowires.

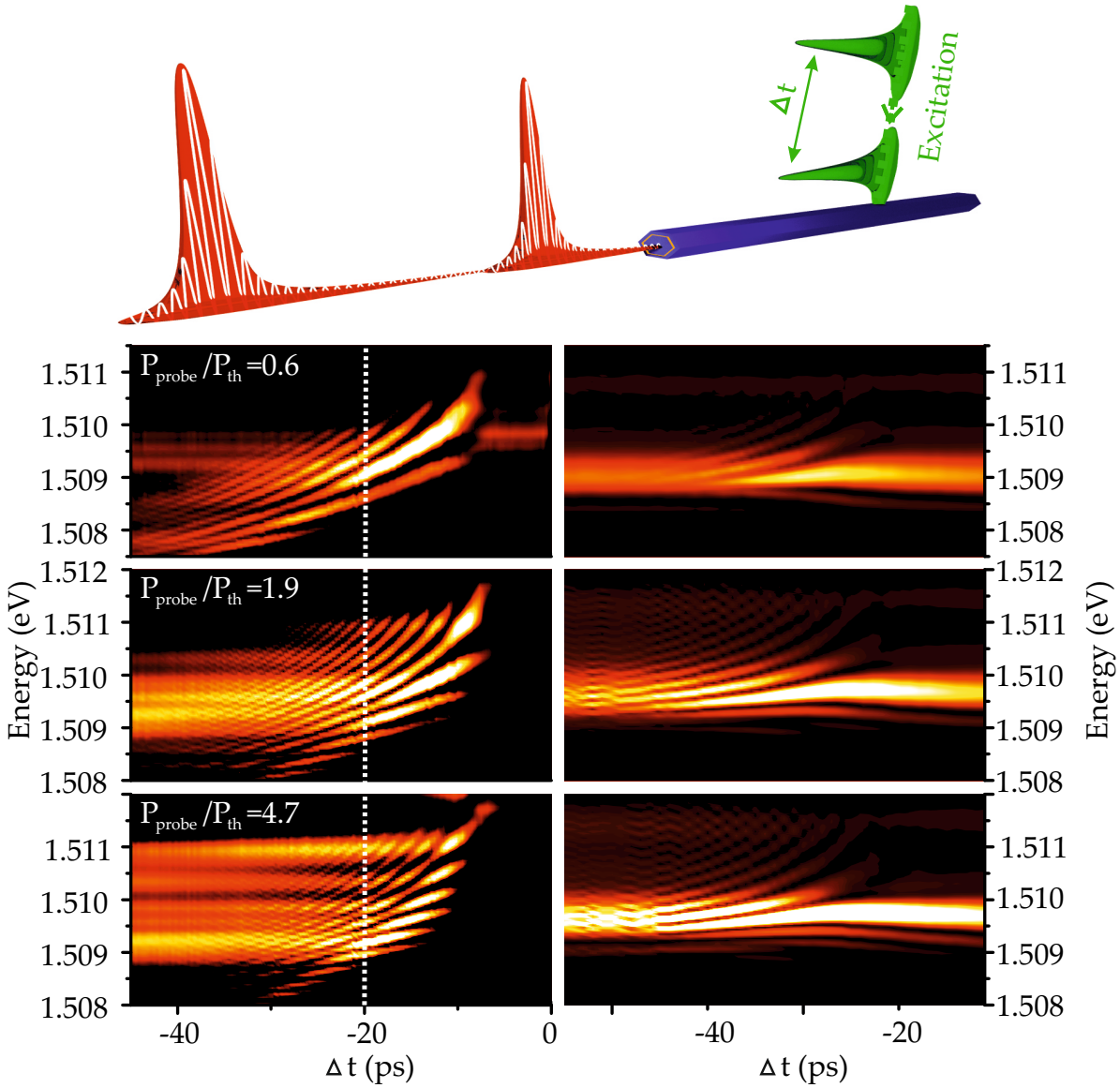

Figure 5.3. *Nanowire Laser response under double pulse excitation: The illustration on the top schematically depicts the double pulse excitation - nanowire Laser emission scheme. The left column depicts experimental spectra of the nanowire Laser response as a function of Δt whereas the right column depicts the corresponding theoretical results. The three rows depict situations for three different probe pulses with an intensity in the SE regime (top row), ASE regime (center row) and lasing regime (bottom row).*

5.3 Spectral nanowire laser response under double pulse excitation

After the optical properties of the nanowire laser under single pulse excitation are characterized, we unblock both excitation paths (pump and probe) and measure the spectral nanowire laser response for different time delays between pump and probe. The leftmost panels of Fig. 5.3 show typical pump-probe data recorded as a function of the time delay between pump and probe (Δt) for P_{pump} close to $\sim 3\times$ P_{th} and three different values of P_{probe}; below threshold (upper panel), close to threshold (middle panel) and above threshold (lower panel). Pronounced interference fringes are observed in the time-integrated spectra recorded for all three combinations of P_{pump} and P_{probe} and persist even for $\Delta t \geq 40$ps.

Two-pulse interference was recently reported for GaN, CdS and ZnO nanowire-lasers in operation regimes corresponding to the direct temporal overlap between the emitted laser pulses [66][138]. In contrast, in Fig. 5.3 we note that interference is still observed in the time integrated spectrum over timescales more than one order of magnitude longer than the duration of the emitted laser pulses themselves. This surprising observation clearly indicates that coherence is preserved in the nanowire-laser over long timescales after lasing has ceased. In order to provide a conclusive explanation of the ultrafast coherent light matter interactions in nanowire lasers, we compare spectra recorded from subsequent nanowire laser pulses with simulations of the coherent charge and photon dynamics in the GaAs nanowires subject to double pulse excitation. The model presented in this section was developed by Prof. Kathy Luedge (TU Berlin). The model is adapted from the well-known Bloch equations for lasers [139] [140] with an additional equation describing the carrier density in the reservoir N_2 and the respective incoherent scattering processes from the reservoir to the lasing state [141]. We emphasize that phase coherence is not expected to be transferred from the excitation source to the nanowire laser output, since the relaxation from the excited reservoir states at $\hbar\omega\_em$=1.59eV to the lasing state at $\hbar\omega_{em}$=1.51eV is incoherent. The system of equations that are solved read:

$$\frac{dp}{dt} = -i\Delta\omega p - \frac{p}{T_p} - iE\frac{\mu_0}{2\hbar}(2\rho_1 - 1) \tag{5.1}$$

$$\frac{dE}{dt} = -ig_m p - \kappa E + D\xi \tag{5.2}$$

$$\frac{d\rho_1}{dt} = R(\rho_0 - \rho_1) - \frac{\rho_1}{T_1} + Im(pE \times \frac{\mu_0}{\hbar}) \tag{5.3}$$

$$\frac{dN_2}{dt} = J - R(\rho_0 - \rho_1) - \frac{N_2}{T_2} \tag{5.4}$$

Here, the complex electric field amplitude E is described in the rotating frame of the optical frequency of $\hbar\omega \sim 1.51$eV (according to the experimental data), p is the polarization and ρ_1 the occupation probability of the electrons inside the lasing transition.

The number of carriers excited within this lasing level is given by $\rho_1 \times N^e$ with the total carrier density N^e that can be accommodated by the lasing state of the nanowire. The dominating timescales are the photon lifetime $\tau_{ph}=(2\kappa)^{-1}$=1ps, the polarization lifetime T_p=5ps, and the electron lifetimes of reservoir and lasing level, T_2 and T_1, respectively. Within the reservoir we assume fast phonon scattering T_2=10ps while within the lasing level the electrons are lost via spontaneous emission, i.e., T_1=0.6ns. The relaxation between the two electronic levels is implemented via a relaxation rate approximation, with a relaxation rate of R^{-1}=2.5ps to reach a quasi-equilibrium occupation of ρ_0 (given by a Fermi distribution). The spontaneous emission factor (β) was chosen to be β=0.01. For the numerical integration the noise is implemented as a stochastic Gaussian white noise source ξ with noise strength

$$D = \sqrt{\frac{\beta\rho_1 N^e}{T_1}\frac{\omega}{2\epsilon_{bg}\epsilon_0}} = \sqrt{\frac{\beta\rho_1}{T_1}g_m\frac{\hbar}{\mu_0}} \tag{5.5}$$

[142][141]. The parameter g_m is the coupling constant that determines the gain of the light matter interaction. It depends on the density of available electrons N^e and on the dipole moment μ_0=0.16 e nm of the transition. The carriers are injected into the reservoir with a pulsed pump intensity

$$J = J_{pump}e^{-\left(\frac{t-t_0}{\Delta_P}\right)^2} + J_{probe}e^{-\left(\frac{t-t_1}{\Delta_P}\right)^2} \tag{5.6}$$

at times t_0 and t_1 with a pump-pulse-width of Δ_P=100fs according to the experimental setup. The value chosen for g_m yields a rate equation gain (modal gain) of 280 cm^-1 for a detuning of $\Delta\omega$=1THz. To produce the data presented in section 5.4, carriers are first injected into a reservoir and subsequently relax to the optically active level. The input parameters for gain and lifetimes (photons, electrons) where chosen according to experimental details: For example, we chose a photon lifetime τ_p=1ps, a lifetime of electrons within the lasing level T_1=0.6ns, an electron lifetime inside the reservoir T_2=10ps and a relaxation rate between reservoir and lasing level of R^-1=2.5ps. The polarization lifetime of T_p=5ps was adjusted to reproduce the experimental results. Thereby, T_p strongly influences the coherent light matter interactions in the nanowire and longer/shorter T_p lead to more/less visible Rabi-oscillations, respectively.
The rightmost panel of Fig. 5.3 shows selected results of our numerical simulations. The best quantitative agreement with our experimental observations was obtained for a photon lifetime in the resonator of ∼1ps, obtained from the measured Q-factor of the resonator modes, carrier lifetimes in the reservoir of ∼10ps and a spontaneous emission lifetime of the lasing state equal to ∼0.6ns. We note that the simulation reproduces most of the principle features observed in the experiment, including the two-pulse interference and the time dependent redshift caused by a small detuning between lasing transition and cavity mode, estimated to be 1.7meV as presented in section 5.2.
The good agreement between experiment and simulations confirm the interpretation of

the observed features presented in Fig. 5.3 as being due to 2-pulse interference in the time integrated spectral response of the studied nanowire-lasers.
To check that the observed fringes do indeed arise from the interference between two successively emitted laser pulses, the fringe separation in the frequency domain Δf is plotted in Fig. 5.4b) as a function of Δt. We note that the fringe separation Δf clearly decreases inversely with increasing Δt, indicative of the interference between the two emitted nanowire laser pulses generated by the pump and the probe pulses. Fig. 5.4a) demonstrates the systematic reduction of the fringe separation with increasing Δt from Δf=150GHz at 10ps (green curve) over Δf=60GHz (red curve) to Δf=40GHz (blue curve) for the case of the probe pulse in the ASE regime. We emphasize that the resolution of the spectrometer used in our experiments of ∼30GHz is very close to what is observed for the minimum fringe separation and the observation of the interference fringes up to 40ps can be considered as a lower limit for the mutual coherence of the nanowire laser pulses.
This Ramsey interference represents the most simple form of a frequency comb in which the fringe separation $\Delta f=1/\Delta\tau$ reflects the inverse of the coherent pulsed nanowire-emission in the time domain $\Delta\tau$ [137][132]. Therefore, $\Delta f=1/\Delta\tau$ represents the repetition rate of the emitted nanowire-laser pulses that are excited by the two excitation pulses that were temporally delayed by Δt.
We emphasize that no phase coherence is expected to be transferred from the excitation to the nanowire laser output, as the relaxation from the excited reservoir state in the conduction band ($\hbar\omega_{exc}$=1.59eV) down to the lasing state ($\hbar\omega_{exc}$=1.51eV) over ∼80meV is expected to completely randomize the phase of the exciton formation.
The measured relationships between $\Delta\tau$,Δf and Δt are plotted in Fig. 5.4b) for a situation with the probe pulse in the ASE regime. Clearly, $\Delta\tau$ is directly proportional to Δt confirming that the observed fringes originate from Ramsey interference in the nanowire laser output as expected. Remarkably, extremely high repetition rates Δf >200GHz are found, corresponding to ultrashort pulse durations of t_{pulse}<5ps.

5.4 Time domain analysis of coherent pulse pairs emitted by the nanowire

The observed pump-probe dynamics can be mapped from the spectral to the temporal domain by computing the Fourier Transformation (FT) of the spectra presented in Fig. 5.3. The results of this procedure are presented in Fig. 5.5 (left panels) together with the corresponding numerical simulations (right panels). The figure compares data recorded for a situation with P_{pump} in the lasing regime and $P_{probe} < P_{th}$ in the spontaneous emission (SE) regime, labelled by L-SE (Fig. 5.5a)), and a situation where both P_{pump} and P_{probe} are in the lasing regime labelled L-L (Fig. 5.5b)). The colour plots reveal that two, temporally distinct nanowire-laser pulses are always generated, provided that P_{pump} is chosen to be above threshold (e.g. $P_{pump}/P_{th}> 2$) and the pump pulse arrives

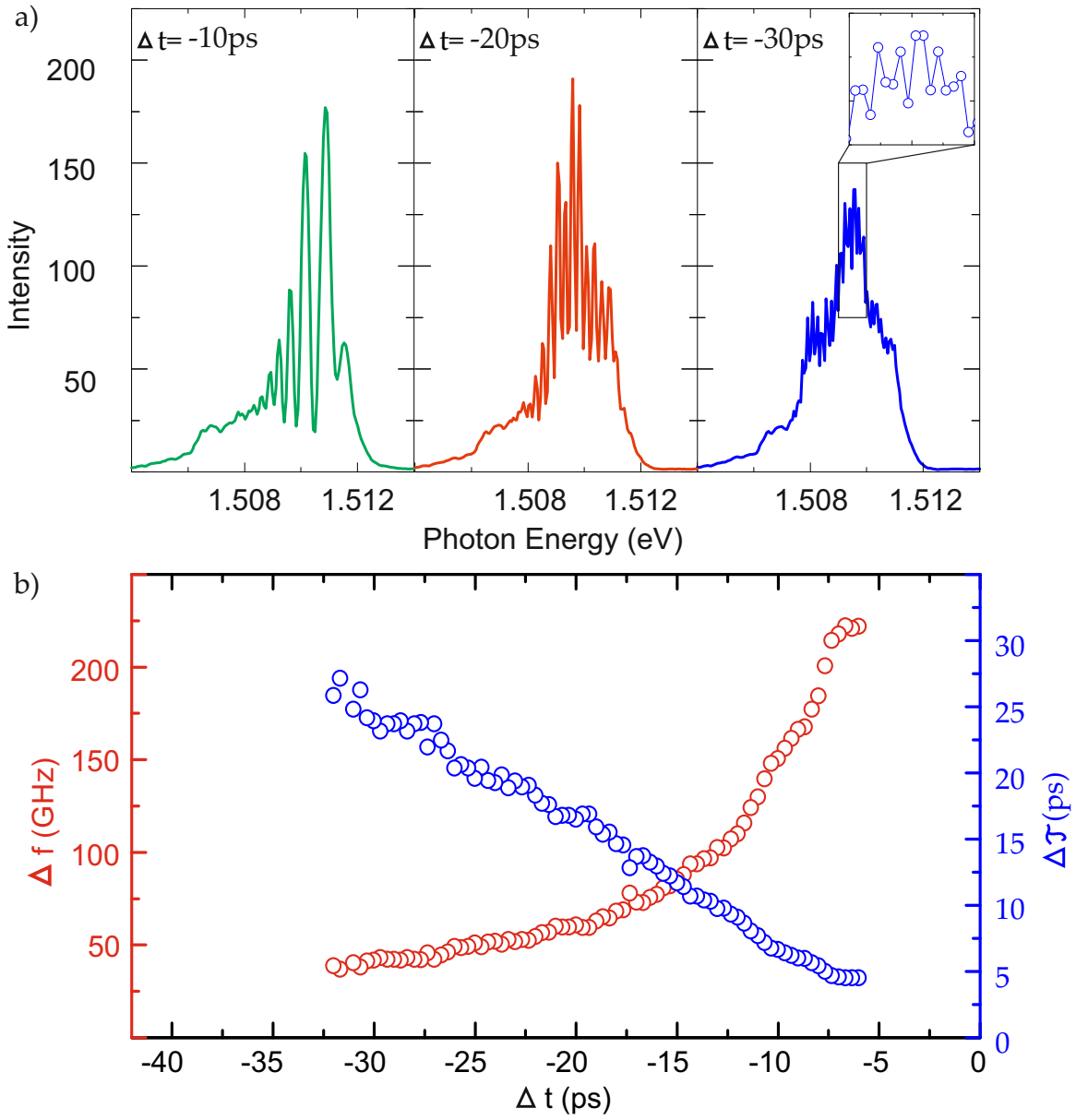

Figure 5.4. *Fringe spacing versus pump-probe delay: (a) Selected spectra recorded from the nanowire-laser subject to a pump pulse in the lasing regime and a probe pulse in the ASE regime for Δt=-10ps (green), Δt=-20ps (red) and Δt=-30ps (blue). The inset shows a zoom in of the spectrum illustrating that modulation is still observed and that the spacing is close to the resolution limit. (b) Repetition rate (red data points) and nanowire laser pulse separation (blue data points) as a function of Δt. The data points are measured from the separation of the interference fringes in the nanowire laser spectra (red data points) and their inverse (blue data points) subject to a pump pulse in the lasing regime and a probe pulse in the ASE regime (example spectra shown in a).*

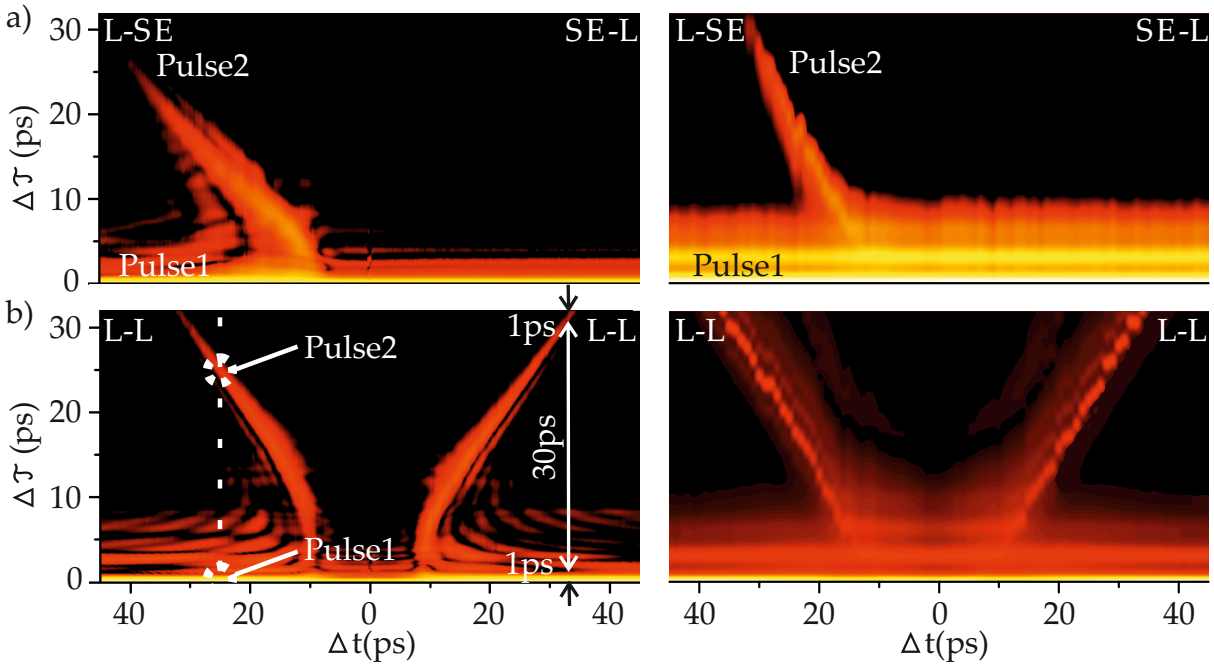

Figure 5.5. *Experimental data (left panels) and theoretical calculations (right panels) of the time dependent emission of the nanowire Laser as a function of Δt. (a) shows the situation with the pump pulse in the lasing regime and the second (probe) pulse in the SE regime. (b) depicts a situation with both, pump and probe pulse, being in the lasing regime (L-L).*

first to create gain in the nanowire. For situations when the weaker probe pulse arrives before the stronger pump then only one laser pulse is observed (Δt>0 - Fig. 5.5a)). We note that in the L-SE configuration, the interference observed in the time integrated spectrum is indicative that the residual gain in the nanowire is sufficient for the weak probe pulse to re-establish lasing and that the two pulses are mutually phase coherent despite exhibiting no temporal overlap at the detector.

When both excitation pulses are in the lasing regime (L-L - Fig. 5.5b)) a clear symmetry is observed around the point of coincidence (Δt=0ps) as two pronounced coherent nanowire laser pulses well separated by a delay >30ps are observed for positive and negative Δt, labelled pulse-1 and pulse-2 on Fig. 5.5. The duration of the first nanowire laser pulse represented by the white line at the bottom of the panels is measured to be t_{pulse}=0.9±0.1ps whereas the second pulse from the probe excitation has a duration ranging from t_{pulse}=3.7ps (Δt=15ps) to 1.6ps (Δt=30ps). Therefore, the analysis in the time domain is in excellent agreement with the results obtained from the analysis of the two-pulse interference in the frequency domain where similar pulse durations of t_{pulse}<5ps corresponding to a ∼200GHz fringe separation are expected.

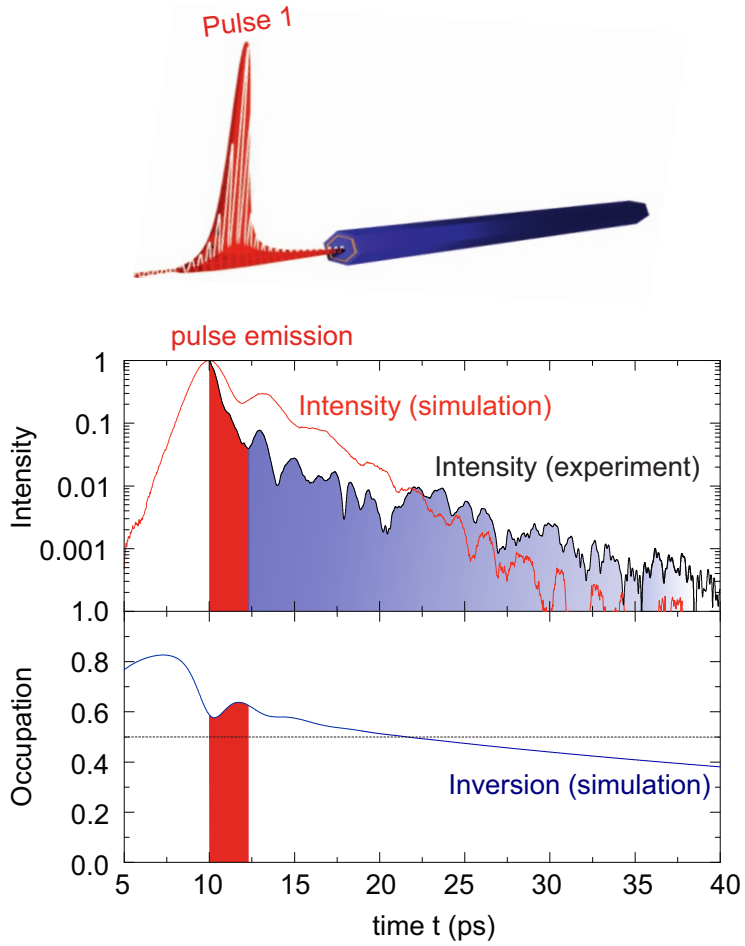

Figure 5.6. *Coherent Rabi oscillations from a single NW laser pulse as schematically depicted at the top of the figure: Time dependence of the emitted intensity obtained by Fourier transforming the optical spectra of the NW laser after only the pump pulse with P/P_th=4 was injected (upper panel, red line: simulations, black line: experimental data) and the computed occupation of the lasing state (blue line, lower panel) as a function of time. The red regions mark the initial short pulse emission during the first Rabi oscillation.*

5.5 Coherent light matter interactions and phase information transfer in the post-lasing regime

In order to give a full explanation of how the mutual phase coherence between two subsequent nanowire laser pulses is established, we now turn the attention to the weak periodic oscillation clearly seen in the L-L data presented in Fig. 5.5. These periodic oscillations are attributed to Rabi oscillations that occur during the pulse emission and in the few picoseconds after lasing has ceased.
This can be seen in Fig. 5.6 that shows the computed occupation of the lasing state

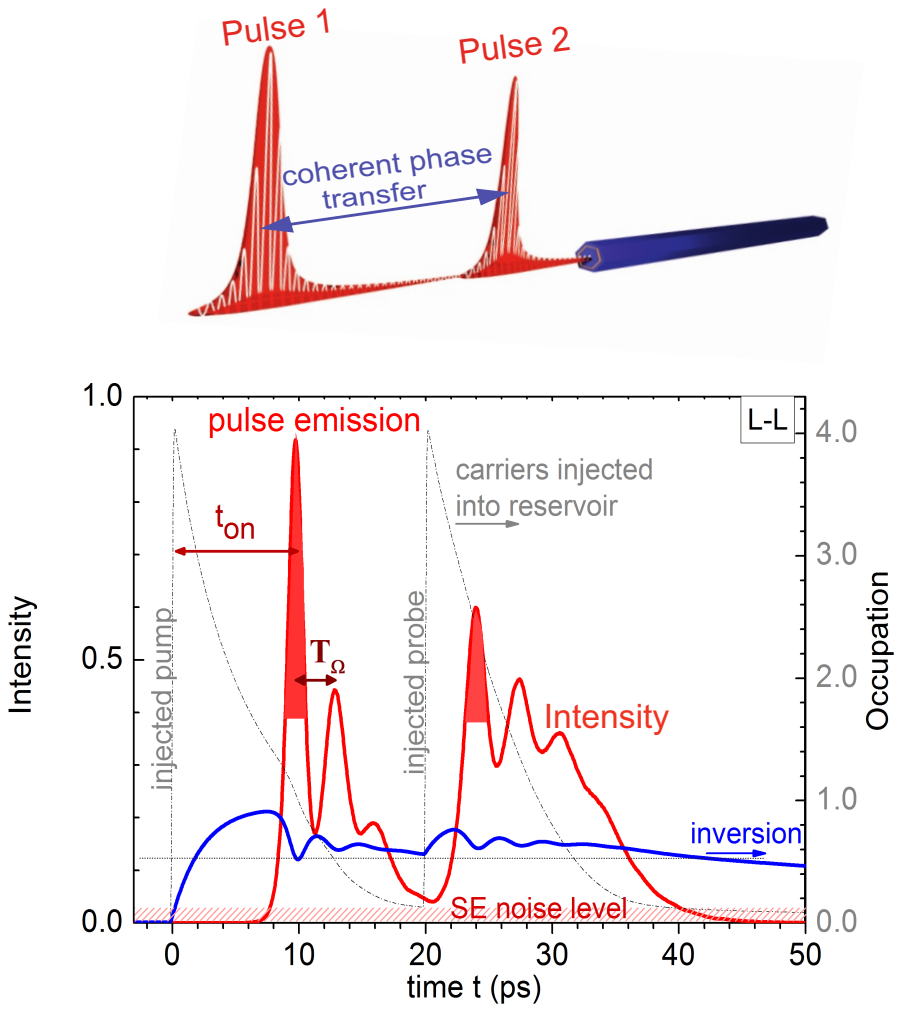

Figure 5.7. *Coherent phase information transfer between two subsequent NW laser pulses as schematically depicted at the top of the figure: directly simulated time-dependent emission (red line) of the NW after a pump and probe pulse in the lasing regime (L-L) separated by Δt=20ps were injected (thin dotted line). Blue line shows the inversion of the laser level and the hatched region depicts the spontaneous emission noise level. The green curves depict theoretical calculations and the black curve is obtained by dFT of a NW laser peak subject to an excitation pulse with P/P_th=4. The red regions mark the initial short pulse emission during the first Rabi oscillation (T_Ω marks the Rabi oscillation period and t_on the time needed to reach inversion after the pump probe arrived).*

as a function of time (blue line, lower panel) together with the theoretical (red line) and experimental (black line) temporal evolution of the photon field in the nanowire-laser (upper panel). The results show that the lasing state is almost fully inverted (occupation>0.8) before the emission of a nanowire laser pulse, marked by the red region on the figure. The initial nanowire laser pulse is formed by Rabi oscillations (blue region) enabled by a persistent occupation close to transparency ($\sim$0.5) extending over timescales towards the spontaneous emission lifetime. Therefore, the initial nanowire laser pulse (red regions) can be considered to be the first beat of a strongly damped Rabi oscillation that prevails for several tens of picoseconds.
As shown in Fig. 5.7, this phase information can be transferred to a subsequent nanowire laser pulse, if the second pulse is excited within a time window of $\sim$30ps. The grey curves depict the excitation laser and the red curves show the emission of the nanowire laser subject to two excitation pulses separated by 20ps. The calculations show that the time delay between the excitation pulse and the nanowire laser response t_{on} $\sim$10ps is in excellent agreement with the experiments presented in section 5.3. The occupation of the lasing state as depicted by the blue line shows that the Rabi oscillations do not undergo the inversion until the second pulse arrives. We continue to provide a consistent explanation of the phase information transfer between subsequent nanowire laser pulses. As depicted on Fig. 5.6, after the initial nanowire laser pulse emission the population of the lasing state remains very close to transparency ($\sim$0.5) since stimulated emission and absorption processes occur over similar timescales. As such, the comparatively slow spontaneous emission depopulates the lasing state over much longer timescales ($\sim$1ns) and the nanowire gain medium remains close to transparency for several tens of ps. Consequently, after emission of the first pulse the residual coherence is preserved in the coupled electron-photon system within the quasi transparent nanowire medium as continuous absorption and stimulated emission is accompanied by collective Rabi oscillations. Hereby, the spontaneously generated phase of the first pulse emitted remains stored within the nanowire laser over timescales such for which the intensity remains larger than the noise level. If the nanowire-laser is subject to a second excitation pulse, relatively little power is needed to lift the population above the lasing threshold and the subsequently emitted pulse recovers the phase of the first pulse.

5.6 Summary

In summary, we have demonstrated how coherent phase information can be transferred between two subsequently emitted nanowire laser pulses by virtue of coherent Rabi oscillations that occur during the post-lasing transparency regime.
The consequent observation of interference fringes reveals the potential for high repetition rates >200GHz whilst preserving mutual coherence between the emitted laser pulses.
The discrete Fourier transform of the spectra obtained from ultrafast pump probe experiments exhibits coherent information storage >30ps and pulse durations <2ps. The

ultrafast pulse emission of the nanowire lasers is followed by strongly damped Rabi oscillations that result from the coherent light matter interactions in the nanowire cavity. The experimental results are in good quantitative agreement with theoretical predictions from a microscopically motivated semiconductor Bloch equation model with a realistic noise source that calculates the phase of the photon field and the polarisation of the lasing state population in the nanowire. The theoretical model is capable of fully describing the coherent phase information transfer between two subsequent nanowire laser pulses and the generation of Ramsey combs found in the experiments.
The results present a novel mechanism for optical information storage and frequency comb generation at ultrafast timescales at the nanoscale.

6 Outlook

6.1 Nanowire lasers with quantum confined gain material

Major current goals in the device performance of nanowire lasers focus on reducing the threshold power, achieving tunability of the gain, control of the emission wavelength and modulation bandwidth, as well as improved temperature stability [42]. Addressing these important metrics has recently fueled substantial activities along two distinct pathways that utilize both extrinsic and intrinsic approaches to enhance nanowire laser performance:

Extrinsically, the exploitation of enhanced light-matter interactions in sub-wavelength plasmonic nanowire resonators [143][144] allows for strong mode confinement and ultralow threshold lasing. Intrinsically, the implementation of quantum confined structures as active gain media, such as quantum wells (QWs), quantum wires (QWRs), or quantum dots (QDs), provides a tried and tested route to enhance gain and improve temperature stability, while lowering their threshold due to their modified electronic density of states (DOS) [145]. Figure 6.1 shows the calculated gain of a 0D (Box), a 1D (wire), a 2D (film) and a 3D (Bulk) $Ga_{0.47}In_{0.53}As/InP$ electron gas system. The results clearly show that the maximum gain strongly increases with decreasing dimensionality of the electron gas system although the carrier concentration used for the gain calculation is kept constant at $n=3\times10^{18}/cm^3$. Therefore, replacing the a bulk gain material by a low dimensional electron gas system can decrease the lasing threshold by more than one order of magnitude. The gain properties of low dimensional electron gas systems can be adjusted by carefully designing the dimensions of the quantum system which further allows to tailor the gain properties of a laser device.

The size confinement properties of such low-dimensional systems also provide even greater flexibility to tune the emission wavelength. In this respect, nanowire lasers with quantum confined gain media have been recently reported using GaN nanowires with embedded InGaN/GaN multiple quantum wells (MQWs) [147], as well as GaAs nanowires containing arrays of axial InGaAs QDs [148]. Besides the latter report, the implementation of quantum heterostructures into nanowire lasers emitting in the near-IR spectral range has remained very scarce despite the great success of nanowire lasers with bulk-like gain media [53] [54] [55] [56] [31] [32].

One focus area of the ongoing research will be the growth and lasing operation of GaAs-AlGaAs core-multishell nanowires containing coaxial single and multiple GaAs

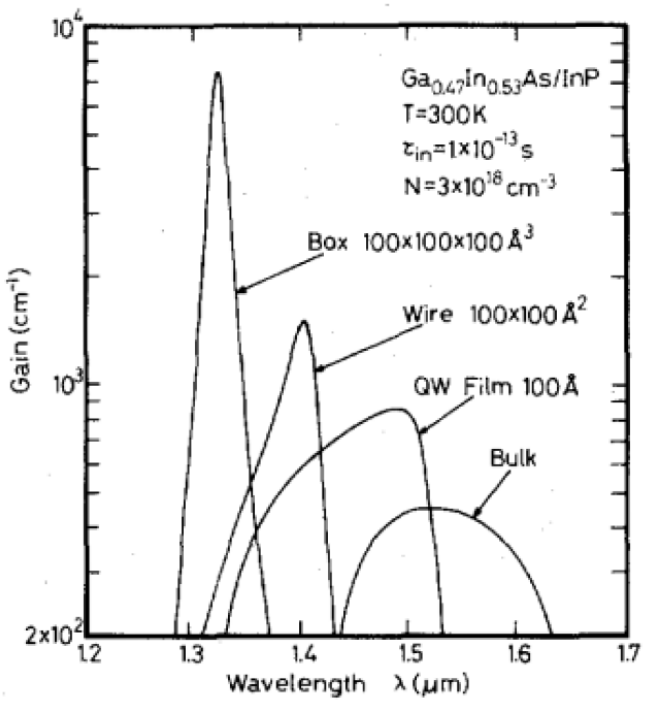

Figure 6.1. *Gain of four different $Ga_{0.47}In_{0.53}As/InP$ electron gas systems as a function of wavelength. The curve labeled as Ḃulkśhows the gain of a 3 dimensional electron gas, the curve labeled with 2́D Filmśhows the gain of a 2 dimensional electron gas in a 10nm thick quantum well, the curve labeled with Ẃireśhows the gain of a 1 dimensional electron gas in a 10nm×10nm thick quantum wire and the curve labeled with Ḃoxśhows the gain of a 0 dimensional electron gas in a 10nm×10nm×10nm quantum dot. The curves are calculated for 300K, a carrier density of $n=3\times10^18/cm^3$ and an intraband relaxation time of $\tau_{in}=1\times10^{-13}$. The figure is taken from [146].*

QWs. Figure 6.2 shows a schematic image (left) together with a cross sectional TEM image (right) of a GaAs-AlGaAs MQW nanowire. Very recently, Stettner et al. unambiguously showed that the QWs act as gain media with the emission wavelength directly associated to the QW, while the nanowire acts as optical cavity providing a threshold for lasing [115]. S-shape lasing characteristics accompanied by linewidth narrowing unambiguously demonstrated lasing operation from multi- and from single- quantum well nanowire lasers at low temperatures. Hereby, the lasing threshold is reduced by a factor that directly scales with the number of embedded QWs, confirming the beneficial effect of the modified density of states. Furthermore, the results show that the gain of complex NW heterostructures can be directly tailored during growth. Ultimately, lasing from a multi-quantum well nanowire is also observed for all temperatures from 19K up to room-temperature, substantiating the large potential of III-V semiconductor NWs with embedded low-dimensional systems for future laser applications [115].

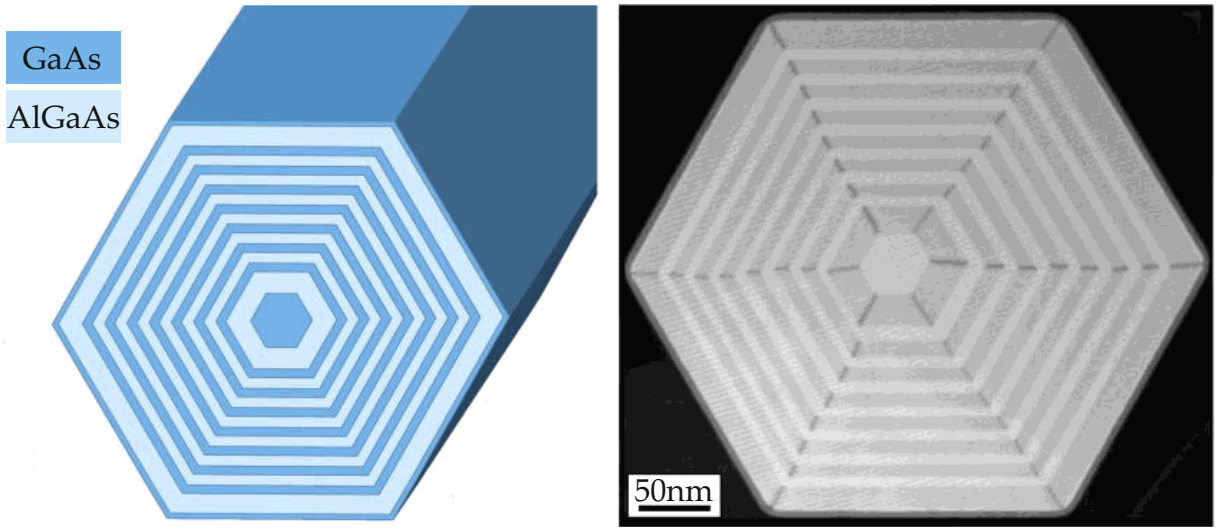

Figure 6.2. *Schematic illustration of the coaxial GaAs-AlGaAs MQW nanowire heterostructure, consisting of 7 periods of 8-nm/10-nm GaAs QWs/AlGaAs barriers (left image) and a cross sectional HAADF-STEM image of the same structure, clearly revealing the Z-contrast between GaAs (bright) and AlGaAs (dark) regions (right image). Both images are depicted from [115].*

6.2 Electrically driven nanowire lasers on microchips

In order to realize the promising perspective of future all-optical signal processing and data communication on and between microchips, novel concepts for integrated electro-optical interconnects are urgently needed. Fig. 6.3a) presents a nanowire laser structure that offers ideal prerequisites for electrically driven lasing operation directly on Si[39]. Exploiting the large nanowire surface to volume ratio, a radial p-n junction could extend the depletion region of a nanowire diode along the entire nanowire axes and, therefore, strongly enhance the spatial overlap of the optical mode with the nanowire gain medium. A enhanced distribution of the gain along the nanowire could be achieved by doping gradient in the nanowire core which enables to spread the electrically injected radiative recombinations across the nanowire.
The nanowire could be embedded in a dielectric surrounding to mechanically stabilize the nanowire and to form a platform for the electrical top contact. The electrical contact layer could be e.g. either a thin metallic layer (Au,Cu,Ti) that enables sufficient transmission or a transparent conducting material such as indium tin oxide (ITO). Using the dielectric reflection layer described in the main section 4.1, the nanowire has an excellent contact to the doped growth substrate which could form a global back contact. The two top and base contacts can be used to drive the lateral nanowire diode while the reflection layer and the nanowire top facet provide optical feedback for the lasing operation of the device. In the proposed geometry[39], the base reflection layer simultaneously provides

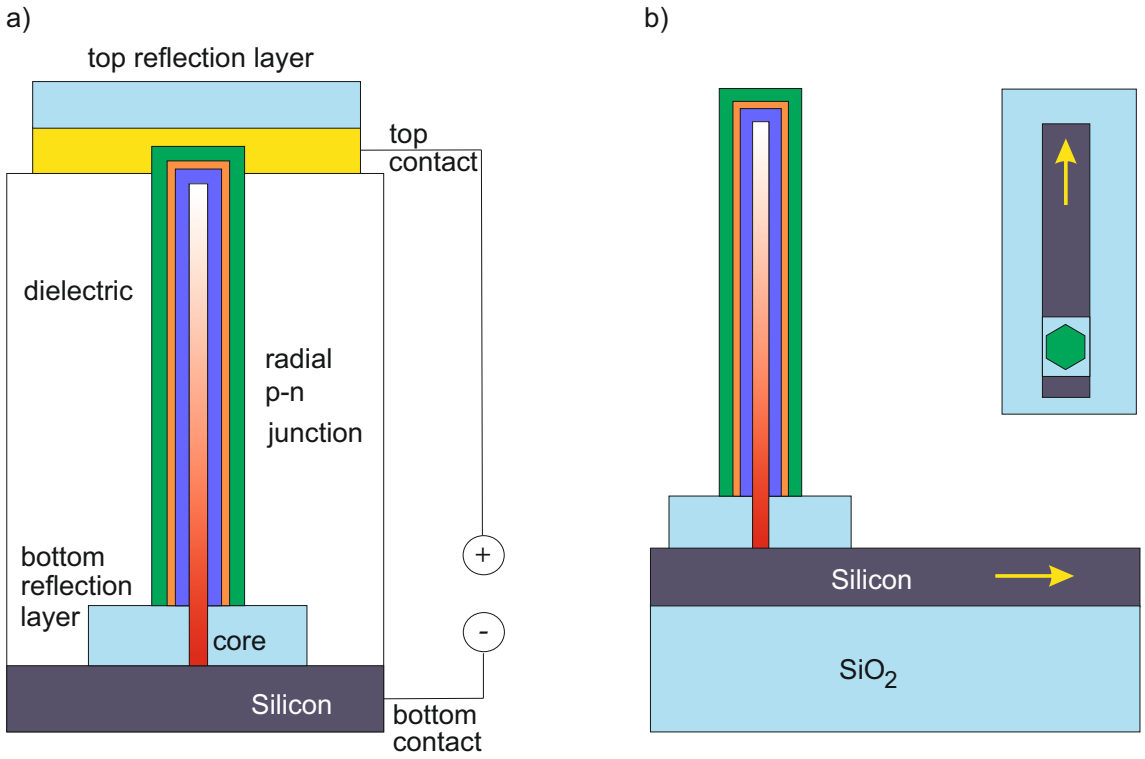

Figure 6.3. *a) Schematic illustration of a electrically driven nanowire laser on Si. The nanowire core (red) is connected to the Si (grey) whereas the the nanowire shell extends only on top of a dielectric reflection layer (light blue, bottom). The core-shell structure forms a radial p-n junction that can be contacted via the silicon substrate and a top contact (gold). The reflectivity of the nanowire top facet can be enhanced by adding another reflection layer (light blue, top) on top of the nanowire. The nanowire may be embedded in a polymer to improve the mechanical stability of the device. b) nanowire laser as presented on a) coupled to a Si waveguide (grey) fabricated from a SiO_2-Si-SiO_2 wafer.*

optical feedback and acts as isolation layer between the back contact and the nanowire shell. Further reductions of the nanowire laser threshold and, therefore, the energy consumption of the device could be achieved by replacing the simple dielectric base reflection layer by a Distributed Bragg Reflector (DBR) or a high contrast grating.

Optical data communication and the implementation of photonic networks using nanowire lasers however requires the coupling of the nanowire emission to optical waveguides[39]. Figure 6.3b) depicts a geometry that allows the coupling of a nanowire laser to an in-plane optical waveguides on a photonic microchip. The waveguides are formed by a high refractive index growth substrate (Si, grey) sandwiched between a low index substrate (SiO_2, blue). The low index substrate on the top of the waveguide acts as

base reflection layer for the nanowire laser whereas the low index substrate underneath supports total internal reflection for the light propagation inside the Si waveguide.
As the nanowire laser is typically grown vertically on the growth substrate, and thus, perpendicular to the optical waveguide underneath, the coupling of fundamental guided modes from the nanowire laser to the waveguides would be typically low. However, already second, third and fourth order waveguide modes inside the nanowire have a strong helical character and therefore, a significant in plane wave vector component [35]. The steep angle of incidence of this type of modes results in high reflectivities at the base reflection layer which reduces the threshold and causes preferential emission into in-plane waveguides.

6.3 Optical computing using nanowire lasers

This section demonstrates how nanowire lasers can be used to perform logic operations directly using light at the nano scale[39]. The fundamental electronic building blocks used in today's computer devices could potentially be replaced by such photonic devices which could dramatically increase computational power and could lead to a strong reduction of the energy consumption of digital devices. Figure 6.4a) shows the top view of a nanowire laser (green hexagon) that is coupled to a optical waveguide interferometer. If the two arms of the interferometer have exactly the same length, both light paths interfere constructively at the output and the signal is 1. However, if the light in one arm of the interferometer is shifted by a phase shift of π, destructive interference will vanish the output and the signal is 0. This can be controlled by an optical gate (red) which could consist of a non-linear medium that can be either switched all-optically or electrically. This nanowire laser transistors could then be used to perform fundamental logic operations such as NOR and NAND gates as depicted in Fig. 6.4b) and c), respectively. With these two fundamental devices, all logic operations could potentially be assembled from nanowire lasers coupled to optical waveguide interferometers. Figure 6.4b) shows the inverse of a logic or operation (only 1 when both gates, G1 and G2, are 0) and Fig. 6.4c) shows the invers of a logic and (only 0 when bot gates, G1 and G2, are 1). These, and all other logic operations could potentially be assembled by a series of parallel or serial circuits of the presented nanowire laser transistor device.

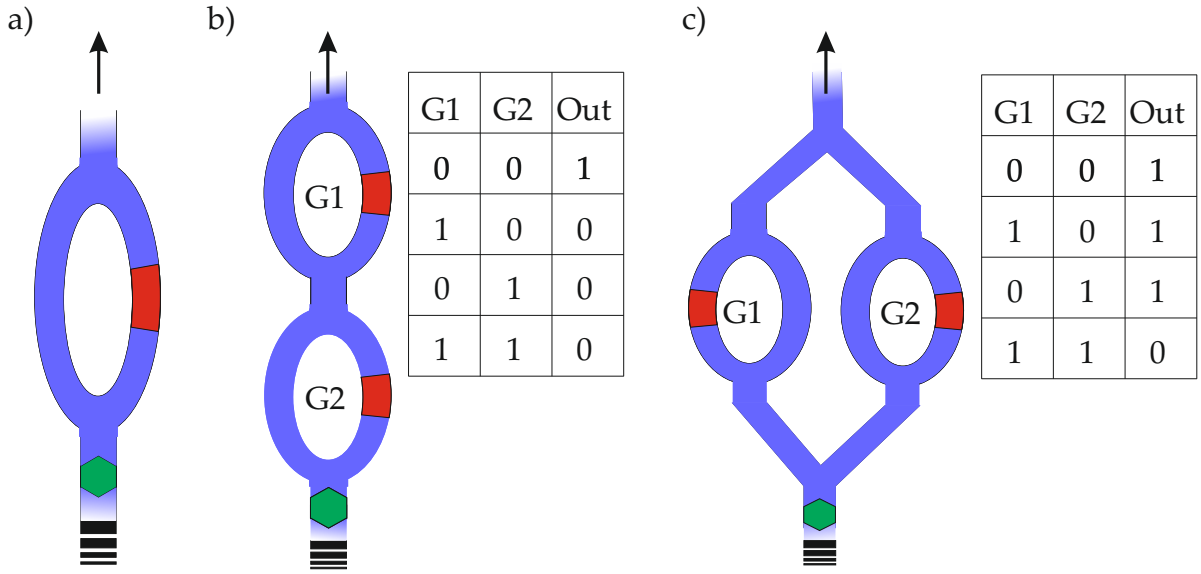

G1	G2	Out
0	0	1
1	0	0
0	1	0
1	1	0

G1	G2	Out
0	0	1
1	0	1
0	1	1
1	1	0

Figure 6.4. *a) Nanowire laser (green) coupled to a waveguide interferometer (blue) forming an optical transistor that can be optically or electrically controlled by a gate (red). b) NAND gate consisting of two coupled nanowire laser transistors. c) NOR gate consisting of two coupled nanowire laser transistors.*

Postface

"The real danger is not that computers will begin to think like men, but that men will begin to think like computers."
- Sydney Harris (Journalist)

One hundred years after Albert Einstein postulated the fundamental principles of stimulated emission [1], lasers have become the most powerful transmitters of information today [2]. The impact of digital technology on modern society makes according to 85% of a previous survey sample from different nations, the world a better place [149]. The majority of the 12000 people asked for the survey are convinced that modern technology accelerates social activism, improves bargains, boosts innovation and enhances productivity. However, the survey also clearly demonstrates that a persistent concern about privacy increases worldwide. According to the majority of the people asked in 11 of the 12 countries, the new technology has had negative impact on their privacy [149]. Consequently, a big technological and political challenge arises that has not less to task than to harmonize the huge advantages of digital technology with the human right of privacy. The human need for security and the convenience of digital information technology however often accepts surveillance and heteronomy before the respect of human rights on short term. This carries the risk to irretrievably dispense privacy as one of the most powerful columns of the free mind by far too easy [150]. However, optical communication could pave the way for quantum communication protocols (e. g. BB84 [20]) capable to fully exploit the wonderful technologies of our modern life whilst maintaining civil rights and liberties.

List of publications

1. Mayer, B. et al. *Lasing from individual GaAs/AlGaAs core shell nanowires up to room temperature.* Nature Communications **4**, (2013).

2. Mayer, B. et al. *Monolithically Integrated High-β Nanowire Lasers on Silicon.* Nano Letters **16**, 152-156 (2016).

3. Mayer, B. et al. *Continuous wave lasing from individual GaAs-AlGaAs core-shell nanowires.* Appl. Phys. Lett. **108**, 071107 (2016).

4. Mayer, B. et al. *Long-term mutual phase locking of picosecond pulse pairs generated by a semiconductor nanowire laser.* arXiv:1603.02169 (2016).

5. Mayer, B., Finley, J. J., Koblmueller, G., Klicpera, J., Abstreiter, G. *Nanowire Laser Structure and Fabrication Method* EU Patentanmeldung **15 185 311.6**, (2015).

6. Koblmueller, G., Mayer, B., Finley, J. J., Abstreiter, G. *A Method for Fabricating a Nanostructure* EU Patentanmeldung **15 185 295.1**, (2015).

7. Stettner, T. et al. *Coaxial GaAs-AlGaAs core-multishell nanowire lasers with epitaxial gain control.* Appl. Phys. Lett. **108**, 011108 (2016).

8. Koblmueller, G., Mayer, B. & Finley, J. J. *GaAs-AlGaAs Core-Shell Nanowire Lasers on Silicon.* accepted for publication in: Semiconductor Science and Technology, SST-102075, (2016).

Appendix

The Appendix presents the main parts of the program code used for the Rate equation analysis of Chapter 3.

6.1 Gain function

```
function y = gain(hw,T,me,mh,n,tao)
%set constants
% echarge=-1.6021766*10.^-19;
% xpi=3.14159265;
% mnull=9.109383*10.^-31;
% cs=2.99792*10^8;
% epsilonz=8.854*10.^-12;
% hplanck=6.62607*10.^-34;
% nrefr=3.65;
%
% prefout=((echarge.^2)*pi)./(*mnull*nrefr*cs*epsilonz*(hplanck.^2));
% prefout

me=me*9.11*10.^-31;
mh=mh*9.11*10.^-31;
hw=toJ(hw);

%Bandgap
Eg=1.508-(5.405*10.^-4)*((T.^2)./(T+204));
Eg=toJ(Eg);

Ep=toJ(23);
pref=0.069374*10.^60;

step=0.0005;

for ii=1:101

   steps(ii)=step*(ii-1);
end
```

```
energies=integralE(Eg+toJ(steps),hw,Eg,T,me,mh,n,tao);
q=trapz(steps,energies);

q=toJ(q);

y=pref*((2*(1./(1./me+1./mh)))^(3/2))*(Ep./hw)*q;
end

function y = integralE(x,hw,Eg,T,me,mh,n,tao)



   y=(sqrt(x-Eg)).*(fc(Ekc(mh,me,x,Eg),uc(n,me),T)-(1-fv(Ekv(mh,me,x,Eg),uv(n,mh),T)))
.*lfct(x,hw,tao);
end

%Fermi distribution in conduction band
function y = fc(x,uc,T)
y = 1./(exp((x-uc)./((1.38*10.^-23)*T))+1);
end

%Fermi distribution in valence band
function y = fv(x,uv,T)
y = 1./(exp((x-uv)./((1.38*10.^-23)*T))+1);
end

%Calculate the quasi fermi levels for a certain carrier density
function y = Ekc(mh,me,E,Eg)
y = (mh./(me+mh))*(E-Eg);
end

function y = Ekv(mh,me,E,Eg)
y = (me./(me+mh))*(E-Eg);
end

function y = uc(n,me)
y = (((n*1000000).^(2./3))/(2*me))*1.064*10.^-67;
end

function y = uv(n,mh)
y = (((n*1000000).^(2./3))/(2*mh))*1.064*10.^-67;
end
```

```
%Transition broadening function
function y = lfct(x,hw,tao)
y=(3.02*10.^33)*tao*sech((x-hw)*tao./(1.05*10^-34));
end
```

6.2 Photoluminescence calculations

```
function y = plotpl()
%get measured spectra:

fileID = fopen('wavelength.txt','r');
formatSpec = '%f';
A = fscanf(fileID,formatSpec);
wavelength = vec2mat(A,1);
fclose(fileID);

hw=1239.842./wavelength;

fileID = fopen('sponem.txt','r');
formatSpec = '%f';
B = fscanf(fileID,formatSpec);
int = vec2mat(B,1);
fclose(fileID);

for vv=10:10
for qq=1:10
for tt=1:14

parfor ii = 1:1340
sponfit(ii) = 0.0040410*pl(1239.842./A(ii),(2+2*tt),0.067,0.22,1*(10.^16),
(0.06+qq*0.01)*(10.^-12),vv);
end

sponmat = vec2mat(sponfit,1);

len=size(hw);
outarray=zeros(1,len(1));
outarray=vertcat(outarray,hw.');
outarray=vertcat(outarray,sponmat.');
outarray=vertcat(outarray,int.');
```

```
end
end
end

plot(hw, sponmat, hw, int );
legend( 'Location', 'NorthWest' );
hold on;
y=1;
end

function y = pl(hwa,T,me,mh,n,tao,varshni)

me=me*9.11*10.^-31;
mh=mh*9.11*10.^-31;
hwa=toJ(hwa);
%Bandgap by Varshni:
Eg=(1.504+varshni*0.0005)-(5.405*10.^-4)*((T.^2)./(T+204));
Eg=toJ(Eg);
pref=1*10.^35;

q=0;
step=0.001;
for ii=1:150

qnow=step*integralE(Eg+toJ(ii*step),hwa,Eg,T,me,mh,n,tao)*(1./toJ(1.5));
q=q+qnow;
end
q=toJ(q);

y=pref*hwa.*q;
end

function y = integralE(x,hw,Eg,T,me,mh,n,tao)
y=hw*sqrt(x-Eg).*(fc(Ekc(mh,me,x,Eg),uc(n,me),T)
.*(1-(1-fv(Ekv(mh,me,x,Eg),uv(n,mh),T)))).*lfct(x,hw,tao);
end

%Fermi distribution in conduction band
function y = fc(x,uc,T)
y = 1./(exp((x-uc)./((1.38*10.^-23)*T))+1);
end
```

```
%Fermi distribution in valence band
function y = fv(x,uv,T)
y = 1./(exp((x-uv)./((1.38*10.^-23)*T))+1);
end

%Calculate the quasi fermi levels for a certain carrier density
function y = Ekc(mh,me,E,Eg)
y = (mh./(me+mh))*(E-Eg);
end

function y = Ekv(mh,me,E,Eg)
y = (me./(me+mh))*(E-Eg);
end

function y = uc(n,me)
y = (((n*1000000).^(2./3))/(2*me))*1.064*10.^-67;
end

function y = uv(n,mh)

y = (((n*1000000).^(2./3))/(2*mh))*1.064*10.^-67; end

%Transition broadening function
function y = lfct(xc,hwc,tao)
y=(3.02*10.^33)*tao*sech((xc-1*hwc)*tao./(1.05*10^-34));
end
```

6.3 Rate equation model

```
function y = plotbeta()

fileID = fopen('ex_power.txt','r');
formatSpec = '%f';
A = fscanf(fileID,formatSpec);
expower = vec2mat(A,1);

fclose(fileID);

expower = expower./873;

dlmwrite('expower',expower);
```

```
fileID = fopen('pl_intensity.txt','r');
formatSpec = '%f';
B = fscanf(fileID,formatSpec);
int = vec2mat(B,1);
fclose(fileID);

peakenergy = [1.50309; 1.50333; 1.50349; 1.50388; 1.50448; 1.50463; 1.50486; 1.50494;...
1.50497; 1.50508; 1.50517; 1.50517; 1.50519; 1.50525; 1.50536; 1.50539;...
1.50541; 1.50545; 1.50559; 1.50569; 1.50587;1.50592; 1.50605];

int=int./100;

odeoptions = odeset ('MaxStep', 1e-13,'InitialStep',1e-13);

totalint=zeros([1,31000]);
totalint2=zeros([1,31000]);
PEAK=zeros([1,31000]);
Nsamples=zeros([1,31000]);
allfourierspec=zeros([1,31000]);
allphotons=zeros([1,31000]);
allcarriers=zeros([1,31000]);
pulsedelay=5;

timesteps=linspace(0,3e-9,30000);
for intvar = 5:5

powerarray=expower*(0.5+intvar*0.1)*10.^-11;

for betavar = 6:6

parfor dd=1:23

[T,Y] = ode15s(@(t,y) solvebeta(t,y,powerarray(dd),(0.22+0*betavar*0.01)
,pulsedelay,peakenergy(dd)),timesteps,[0 0],odeoptions);

st=size(T);
stime=size(timesteps);

totalint(dd)=0;
totalint2(dd)=0;
Int=zeros([1,st]);
Int2=zeros([1,st]);
```

```
totalint2(dd)=trapz(timesteps(1,:),Y(:,2).^2);
totalint2(dd)=real(totalint2(dd));

[fft_fwhm,fft_sum,fft_peak]=own_fft(timesteps,Y(:,2),totalint2(dd),dd);

parzeval=sqrt((totalint2(dd))./(fft_sum));
parzeval

FWHM(dd)=fft_fwhm;

AA(dd)=fft_peak;

FWHMphotons(dd)=get_fwhm(T,Y(:,2));

T2=T.';
T2(end:31000)=0;
carriers=Y(:,1).';
carriers(end:31000)=0;
photons=Y(:,2).';
photons(end:31000)=0;

allphotons=vertcat(allphotons,T2);
allphotons=vertcat(allphotons,photons);
allcarriers=vertcat(allcarriers,T2);
allcarriers=vertcat(allcarriers,carriers);
end
end
end
end
```

```
function dy = solvebeta(t,y,power,betax,timedelay,photonenergy)

dy = zeros(2,1); % a column vector for the ODE solutions

beta=betax;

gth=66.5; %HE31
```

```
%Excitation pulse width
dtpulse=455*10^-15;
%Excitation power:
pave=power;
%Photon energy at the measured lasing peak
hw=toJ(photonenergy);
%Shockley-Read-Hall Non Radiatiove recombination
A=(1./(0.69*10.^-9));
%Spont. em. lifetime
taosp=700*10.^-12;
%Auger recombinations
C=7*10.^-30;
%group velocity calculated by numeric simulations
vg=(2.98*10.^8)./4.99;

%confinement factor
gamma=1.255;

%Not needed constants. Input/Output curve is fitted to measurements
%by a prefactor...
rep=80000000;
V=2*(180.^2)*3.1416*13000*10.^-27;
fcore=1;
oabs=5*10.^-12;
Aspot=25*10.^-12;
gcavity=0;
Nth=0;
Ns=0;
g0=0;

%This are the two rate equations. y(1) is the carrier density. y(2) is
%the photon density:

dy(1) = (P(dtpulse,pave,rep,t,timedelay).*frac(fcore,oabs,Aspot)./(hw*V))-(A*y(1))-
(y(1)./taosp)-(C*y(1).^3)-vg*100*gain(photonenergy,20,0.067,0.22,y(1),(0.13*10.^-12))*y(2);
dy(2) = gamma*vg*100*(gain(photonenergy,20,0.067,0.22,y(1),(0.13*10.^-12))
-gth)*y(2)+gamma*beta*(y(1)./taosp);
end

%Excitation pulse. Can also be used to make a pulse sequence
function y = P(dtpulse,pave,rep,x,timediff)
```

```
pulse_sequence = 0;
for pp=1:1

pulse_sequence = pulse_sequence+(8./8)*((pave./(rep*dtpulse))
*sech(1.76*(x-(1*(pp-1)*timediff*1*10.^-12)-0.1*10.^-9)./dtpulse).^2);

end

y=pulse_sequence;

end
%Not needed prefactor calculation

function y = frac(fcore,oabs,Aspot)
y=fcore*oabs./Aspot;
end
```

6.4 Fourier transformation

```
function [y1,y2,y3] = own_fft(xtime,pulseint,normalization,sweepcount)

[ypeak,xpeak]=max(pulseint);
xphase=xtime(xpeak);
xphase=xphase+0*10.^-12;

N=size(xtime);
df=1./(3*10^-9);

J=0.95*(1./3)*15000;

fr=zeros([1,250000]);
fourierarray=zeros([1,250000]);

for jj=1:J+1

fr(jj)=(jj-1-J./2)*df;

fouriersum=0;
for ii=1:N(2)
fouriersum=fouriersum + (1e-13)*pulseint(ii)*exp((((-fr(jj)*2*pi*1i))*(xtime(ii)-xphase)));
end
```

```
fourierarray(jj)=(abs(fouriersum));
end

xsum=trapz(fr,fourierarray.^2);

figure('Name','fourier');
plot(fr*4.135668*10.^-15,fourierarray);

[yfft,xfft]=max(fourierarray);

y1=get_fwhm(fr*4.135668*10.^-15,fourierarray);
y2=xsum;
y3=yfft;
end
```

Acknowledgement

Jon Finley,
I want to thank you for being a true mentor for me. Thank you so much for all the things that I learned from you, for inspiring me and for supporting me to become a researcher. I also thank you for bringing together so many special and crazy people at E24 and creating the atmosphere that I so much enjoyed to work in.

Gregor Koblmüller,
vielen vielen Dank für die Doktorrandenstelle und die riesige Unterstützung die ich von dir bekommen habe. Danke für deine große Expertise, für die Motivation die Patente zu schreiben, für die Pressetermine, für die so wichtige Idee mit den "sacrificial wires", für den Review Artikel und für die Empfehlungsschreiben die du unter schwierigsten Bedingungen für mich angefertigt hast. Danke, dass du an mich geglaubt hast und es mir ermöglicht hast ein Forscher zu werden.

Daniel Rudolph,
Dansky - voll laser wie der abgeht! Tausend Dank für deine großartige Doktorarbeit, die meine Arbeit erst ermöglicht hat. Danke für deine Unterstützung, die genialen Städtetrips und die hammer Zeit.

Joscha Schnell,
danke für die tolle Zeit, das fantastische Konzert, deine Lebensfreude und deine Freundschaft.

Lisa Janker,
danke für dein großes Forscherherz, deine Energie, die großartige Zeit und deine Freundschaft.

Sabrina Sterzl,
danke für die philosophischen Gespräche und deine tolle und unermüdliche Arbeit im Labor.

Tobi Kostenbader,
TK, ich weiß nicht ob du es weißt, aber du hast mich extrem motiviert in der Forschung zu bleiben. Danke für deine tolle Bachelorarbeit und deine Herzlichkeit.

Laura,
danke für deine unerschöpfliche Liebe und dass du bei mir bist. Du bist die wundervollste Freundin die man sich vorstellen kann und ich liebe dich sehr.

Mama,
Danke, dass du mit deiner Liebe zur Natur, zu Blumerl und Käferl, deiner Faszination für die Wissenschaft und deinem unerschütterlichen Idealismus mein Wertesystem geprägt hast. Danke, dass du immer für mich da bist und dass es mich gibt.

Steffi,
Danke für all die Geborgenheit, die Sicherheit und den Rückhalt den du mir gibst und dass du bedingungslos immer für mich da bist. Danke, dass du eine so wundervolle Familie gegründet hast in der ich mich zu Hause fühle. Ich hab dich furchtbar lieb.

Mäx,
du bist mit Sicherheit einer der klügsten Menschen die ich je getroffen habe und je treffen werde. Dass dein Charakter dann auch noch von enormer Empathie, höchsten moralischen Wertvorstellungen und einer tiefen freundschaftlichen Loyalität geprägt ist, ist für mich ein riesen Glücksfall. Dein Rat, deine aktive Hilfe und deine Freundschaft haben mir extrem geholfen diese Doktorarbeit zu bewältigen. Vielen Dank!

Jan-Phillip,
Danke für deinen unermüdlichen Zuspruch die Doktorarbeit abzuschließen und die wundervolle Freundschaft. Danke für deinen Blick auf die Welt, deine Fähigkeit die Dinge hinter den Dingen zu erkennen und sie mit mir zu teilen.

Bibliography

[1] Einstein, A. *Zur Theorie der Strahlung.* Mitteilungen der Physikalischen Gesellschaft Zürich. Nr. **18**, (1916).

[2] van Uden, R., G., H., et al. *Ultra-high-density spatial division multiplexing with a few-mode multicore fibre.* Nature Photonics **8**, (2014).

[3] Hayashi, I., Panish, M. B., Foy, P. W. and Sumski, S. *Junction lasers which operate continuously at room temperature.* Appl. Phys. Lett. **17**, p. 109 (1970).

[4] http://europa.eu/rapid/press-release_MEMO-10-200_de.htm.

[5] Siegmann, A., E. *Lasers.* University Science Books, p. 2-4 (1986).

[6] DeCusatis, C. *Handbook of Fiber Optic Data Communication: A Practical Guide to Optical Networking.* Academic Press, p. 101 (2011).

[7] Coldren, L., A., Corzine, S., W., Mašanović, M., L. *Diode Lasers and Photonic Integrated Circuits.* Wiley, p. 25 (2012).

[8] Szweda, R. *Diode Laser Materials and Devices - A Worldwide Market and Technology Overview to 2005* Elsevier (2001).

[9] Carroll, J., E., Whiteaway, J., Plumb, D. *Distributed Feedback Semiconductor Lasers.* IET, (1998).

[10] Yang, G., M., MacDougal, M. H., Dapkus, P. D. *Ultralow threshold current vertical cavity surface emitting lasers obtained with slective oxidation.* Electron. Lett. **31**, p. 886 (1995).

[11] Krier, A. *Mid-infrared Semiconductor Optoelectronics.* Springer, p. 271, p. 160 (2007).

[12] IBM *Optical Interconnects at IBM.* $http://www.zurich.ibm.com/sys/io_{l}inks/interconnects.html$. (2013).

[13] www.photonics.de *Forecast: VCSEL Market to Grow to $2.1B by 2018.* $http://www.photonics.com/Article.aspx?AID = 56571$ (2014).

[14] Richardson, D. J., Fini, J. M. & Nelson, L. E. *Space-division multiplexing in optical fibres.* Nature Photonics **7**, 354-362 (2013).

[15] Kash, J. A. et al. *Optical interconnects in exascale supercomputers* 2010 IEEE Photinic Society's 23rd Annual Meeting, 483-484 (2010).

[16] IBM *Silicon Integrated Nanophotonics.* $http://researcher.watson.ibm.com/researcher/view_{g}roup.php?id = 2757$. (2012).

[17] Sun, C. et al. *Single-chip microprocessor that communicates directly using light.* Nature **528**, 534-538 (2015).

[18] Magen, N., Kolodny, A., Weiser, U. and Shamir, N. *Interconnect power dissipation in a microprocessor.* SLIP 04 Proceedings of the 2004 international workshop on System level interconnect prediction, New York, 2004.

[19] Aghari, M. and Krishnamoorthy, A. V., *Silicon Photonics - Energy-efficient communication.* Nature Photonics **5**, p. 268, 2011.

[20] Bennett, C. H. and Brassard, G. *Quantum cryptography: Public key distribution and coin tossing.* Proceedings of IEEE International Conference on Computers, Systems

and Signal Processing **175**, p. 8 (1984).
[21] Liang, D., Bowers, J. E. *Recent progress in lasers on Si.* Nature Photonics **4**, p. 511 - 517 (2010).
[22] Li, T., Mastro, M., Dadgar, A. *III-V Compound Semiconductors.* CRC Press (2011).
[23] Chen, S. et al. *Electrically pumped continuous-wave III-V quantum dot lasers on silicon.* Nature Photonics **10**, 307-311 (2016).
[24] Liu, J. et al. *Tensile-strained, n-type Ge as a gain medium for monolithic laser integration on Si.* Opt. Express **15**, p. 11272 - 11277 (2007).
[25] Wirth, S. et al. *Lasing in direct-bandgap GeSn alloy grown on Si.* Nature Photonics **9**, p. 88 - 92 (2015).
[26] Rong, H. et al. *Low-threshold continuous-wave Raman silicon laser.* Nature Photonics **1**, p. 232 - 237 (2007).
[27] Groenert, M. E. et al. *Monolithic integration of room-temperature cw GaAs/AlGaAs lasers on Si substrates via relaxed graded GeSi buff er layers.* J. Appl. Phys. **93**, p. 362 - 367 (2003).
[28] Cerutti, L., Rodriguez, J. B., Tournie, E. textitGaSb-based laser, monolithically grown on silicon substrate, emitting at 1.55 um at room temperature. IEEE Photon. Tech. Lett. **22**, p. 553 - 555 (2010).
[29] Liu, J., Sun, X., Camacho-Aguilera, R., Kimerling, L. C., Michel, J. *Ge-on-Si laser operating at room temperature.* Opt. Lett. **35**, p. 679 - 681 (2010).
[30] Diehl, R. *High-Power Diode Lasers: Fundamentals, Technology, Applications.* Springer (2003).
[31] Saxena, D. et al. *Optically pumped room-temperature GaAs nanowire lasers.* Nature Photonics **7**, 963-968 (2013).
[32] Mayer, B. et al. *Lasing from individual GaAs/AlGaAs core shell nanowires up to room temperature.* Nature Communications **4**, (2013).
[33] Nakamura, S. et al. *Room-temperature continuous-wave operation of InGaN multi-quantum-well structure laser diodes.* Appl. Phys. Lett. **69**, p. 4056 (1996);.
[34] Malik, R. J. *III-V semiconductor materials and devices.* Elsevier Science Publishers B. V., p. 410 (2003).
[35] Chen, R. et al. *Nanolasers grown on Si.* Nature Photonics **5**, p. 170 - 175 (2011).
[36] Mayer, B. et al. *Monolithically Integrated High-β Nanowire Lasers on Silicon.* Nano Letters **16**, 152-156 (2016).
[37] Mayer, B. et al. *Continuous wave lasing from individual GaAs-AlGaAs core-shell nanowires.* Appl. Phys. Lett. **108**, 071107 (2016).
[38] Mayer, B. et al. *Long-term mutual phase locking of picosecond pulse pairs generated by a semiconductor nanowire laser.* arXiv:1603.02169 (2016).
[39] Mayer, B. et al. *Nanowire Laser Structure and Fabrication Method* EU Patentanmeldung **15 185 311.6**, (2015).
[40] Mayer, B. et al. *A Method for Fabricating a Nanostructure* EU Patentanmeldung **15 185 295.1**, (2015).
[41] Mayer, B. et al. *GaAs-AlGaAs Core-Shell Nanowire Lasers on Silicon.* accepted for

publication in: Semiconductor Science and Technology, SST-102075, (2016).
[42] Yan, R., Gargas, D. & Yang, P. *Nanowire Photonics.* Nature Photonics **3**, 569-576 (2009).
[43] Gudiksen, M. S., Lauhon, L. J., Wang, J., Smith, D. C. & Lieber, C. M. *Growth of nanowire superlattice structures for nanoscale photonics and electronics.* Nature **415**, 617-620 (2002).
[44] Hill, M. T. & Gather, M. C. *Advances in small lasers.* Nature Photonics textbf8, 908-918 (2014).
[45] Benson, O. *Assembly of hybrid photonic architectures from nanophotonic constituents.* Nature textbf480, 193-199 (2011).
[46] Glas, F. *Critical dimensions for the plastic relaxation of strained axial heterostructures in free-standing Nanowires.* Phys. Rev. B textbf74, 121302-1 - 121302-4 (2006).
[47] Treu, J. et al. *Enhanced Luminescence Properties of InAs-InAsP Core-Shell Nanowires.* Nano Lett. textbf13, 6070-6077 (2013).
[48] Holm, J. V., Jrgensen, H. I., Krogstrup, P., Nygrd, J., Liu, H. & Aagese, M. *Surface-passivated GaAsP single-nanowire solar cells exceeding 10% efficiency grown on silicon.* Nature Comm. **4**, (2013).
[49] Liu, X. et al. *All-printable band-edge modulated ZnO nanowire photodetectors with ultra-high detectivity.* Nature Comm. **5**, DOI: 10.1038/ncomms5007 (2014).
[50] No, Y. S. et al. *A Double-Strip Plasmonic Waveguide Coupled to an Electrically Driven Nanowire LED.* Nano Lett. **13**, 772-776 (2013).
[51] Tomioka, K., Motohisa, J., Hara, S., Hiruma, K. & Fukui, T. *GaAs/AlGaAs Core Multishell Nanowire-Based Light-Emitting Diodes on Si.* Nano Lett. **10**, 1639-1644 (2010).
[52] Duan, X., Huang, Y., Agarwal, R. & Lieber, C. M. *Single-nanowire electrically driven lasers.* Nature **421**, 241-245 (2003).
[53] Johnson, J. C. et al. *Single gallium nitride nanowire lasers.* Nature Mat. **1**, 106-110 (2002).
[54] Xiao, Y. et. al. **Single-Nanowire Single-Mode Laser.** Nano Lett. **11**, 1122-1126 (2011).
[55] Liu, X., Zhang, Q., Xiong, Q. & Sum, T. C. *Tailoring the Lasing Modes in Semiconductor Nanowire Cavities Using Intrinsic Self Absorption.* Nano Lett. **13**, 1080-1085 (2013).
[56] Wang, Z. et al. *Polytypic InP Nanolaser Monolithically Integrated on (001) Silicon.* Nano Lett. **13**, 5063-5069 (2013).
[57] Piccione, B., Cho, C.-H., van Vugt, L. K. & Agarwal, R. *All-optical activeswitching in individual semiconductor nanowires.* Nat. Nanotechnol. **7**, 640-645 (2012).
[58] Strauf, S. et al. *Quantum optics: towards efficient quantum sources.* Nature Photon. textbf4, 132-134 (2010).
[59] Friedler, I. et al. *Efficient photonic mirrors for semiconductor nanowires.* Opt. Lett. textbf33, 2635-2637 (2008).
[60] Sun, H.; et al. *Nanopillar Lasers Directly Grown on Silicon with Heterostructure Surface Passivation.* ACS Nano **8**, 6833 (2014).

[61] Maslov, A. V. & Ning, C. Z. *Reflection of guided modes in a semiconductor nanowire laser.* App. Phys. Lett. **83**, 1237-1239 (2003).
[62] Saxena, D., Mokkapati, S., Tan, H. H. & Jagadish, C. *Designing single GaAs nanowire lasers.* Conference on Optoelectronic and Microelectronic Materials & Devices 101-102 (2012).
[63] Röder, R. *Continuous Wave Nanowire Lasing* Nano Lett. **13**, 3602 (2013).
[64] Geburt, S. et al. *Low threshold room-temperature lasing of CdS nanowires.* Nanotechnology **23**, (2012).
[65] Huang, M. H. et al. *Room-temperature ultraviolet nanowire nanolasers.* Science **292**, 1897-1899 (2001).
[66] Sidiropoulos, T. P. H.; et al. *Ultrafast plasmonic nanowire lasers near the surface plasmon frequency.* Nat. Phys. **10**, 870 (2014).
[67] Rudolph, D. et al. *Spontaneous Alloy Composition Ordering in GaAs-AlGaAs Core-Shell Nanowires.* Nano Letters 13 **4**, p. 1522 - 1527 (2013).
[68] Saxena, D.; et al. *Mode profiling of Semiconductor Nanowire Lasers.* Nano Lett. **15**, 5342-5348 (2015).
[69] Ding, J. X. et al. *Lasing in ZnS nanowires grown on anodic aluminum oxidetemplates.* Appl. Phys. Lett. **85**, 2361-2363 (2004).
[70] Lu, F. et al. *Nanolasers grown on silicon-based MOSFETs.* Opt. Express **20**, 12171-12176 (2012).
[71] Chin, A. H. et al. *Near-infrared semiconductor subwavelength-wire lasers.* Appl. Phys. Lett. **88**, 163115 (2006).
[72] Hua, B., Motohisa, J., Kobayashi, Y., Hara, S. & Fukui, T. *Single GaAs/GaAsP coaxial core-shell nanowire lasers.* Nano Lett. **9**, 112-116 (2009).
[73] Ning, C. Z. *Semiconductor nanolasers.* Phys. Status Solidi B **247**, 774-788 (2010).
[74] Zimmler, M. A., Capasso, F., MuÂ¨ller, S. & Ronning, C. *Optically pumpednanowire lasers: invited review.* Semicond. Sci. Technol. **25**, 024001 (2010).
[75] Hua, B., Motohisa, J., Ding, Y., Hara, S. & Fukui, T. *Characterization of Fabry-Perot microcavity modes in GaAs nanowires fabricated by selective-area metalorganic vapor phase epitaxy.* Appl. Phys. Lett. **91**, 131112 (2007).
[76] Jiang, N. et al. *Long minority carrier lifetime in Au-catalyzed GaAs/AlxGa1-xAs core-shell nanowires.* Appl. Phys. Lett. **101**, 023111-1-4 (2012).
[77] Titova, L. V. et al. *Temperature dependence of photoluminescence from singlecore-shell GaAs-AlGaAs nanowires.* Appl. Phys. Lett. **89**, 173126 (2006).
[78] Rudolph, D. et al. *Direct observation of a non-catalytic growth regime for GaAsnanowires.* Nano Lett. **11**, 3848-3854 (2011).
[79] Zardo, I. et al. *Raman spectroscopy of wurtzite and zinc-blende GaAsnanowires: polarization dependence, selection rules, and strain effects.* Phys.Rev. B **80**, 245324 (2009).
[80] Fontcuberta i Morral, A. et al. *Prismatic quantum heterostructures synthesizedon molecular-beam epitaxy GaAs nanowires.* Small **4**, 899-903 (2008).
[81] Hertenberger, S. et al. *Growth kinetics in position-controlled and catalyst-freeInAs nanowire arrays on Si 111 grown by selective area molecular beamepitaxy.* J. Appl. Phys.

108, 114316 (2010).
[82] Demichel, O., Heiss, M., Bleuse, J., Mariette, H. & Fontcuberta i Morral, A. *Impact of surfaces on the optical properties of GaAs nanowires.* Appl. Phys.Lett. **97**, 201907-1-3 (2010).
[83] Hocevar, M. et al. *Residual strain and piezoelectric effects in passivatedGaAs/AlGaAs core-shell nanowires.* Appl. Phy. Lett. **102**, 191103 (2013).
[84] Blakemore, J. S. *Semiconducting and other major properties of gallium arsenide.* Appl. Phys. Lett. **53**, (1982).
[85] Philipp, H. R. and E. A. Taft *Optical Constants of Silicon in the Region 1 to 10 ev.* Physical Review **20**, 37-38 (1960).
[86] Malitson, I. H. *Interspecimen Comparison of the Refractive Index of Fused Silica.* JOSA **55**, 1205-1208 (1965).
[87] Chang, S.-W. and Chuang, S. L. *Fundamental Formulation for Plasmonic Nanolasers.* IEEE Journal of Quantum Electronics **45**, 1014-1023 (2009).
[88] Ning, C. Z. *Semiconductor Nanowire Lasers.* 1st edn, Vol. 86, 455-486 Elsevier Inc., 2012. , (2012).
[89] Chow, W. W. & Koch, S. W. *Semiconductor-Laser Fundamentals.* Springer , 95-96 (1999).
[90] Grilli, E., Guzzi, M., Zamboni, R. & Pavesi, L. *High-precision determination ofthe temperature dependence of the fundamental energy gap in gallium arsenide.* Phys. Rev. B **45**, 1638-1644 (1992).
[91] Spirkoska, D. et al. *Structural and optical properties of high quality zincblende/wurtzite GaAs nanowire heterostructures.* Phys. Rev. B **80**, 245325 (2009).
[92] Heiss, M. et al. *Direct correlation of crystal structure and optical properties inwurtzite/zinc-blende GaAs nanowire heterostructures.* Phys. Rev. B **83**, 045303 (2011).
[93] Jahn, U. et al. *Luminescence of GaAs nanowires consisting of wurtzite andzinc-blende segments.* Phys. Rev. B **85**, 045323 (2012).
[94] Zimmler, M. A., Bao, J., Capasso, F., MuÂ¨ller, S. & Ronning, C. *Laser action in nanowires: observation of the transition from amplified spontaneous emissionto laser oscillation.* Appl. Phy. Lett. **93**, 051101-1-3 (2008).
[95] Casperson, L. W. et al. *Threshold characteristics of multimode laser oscillators.* J. Appl. Phys. **46**, 5194 (1975).
[96] Siegmann, A. E. Lasers. University Science Books, 1986. , (1986).
[97] Henry, C. *Theory of the linewidth of semiconductor lasers.* IEEE Journal of Quantum Electronics **18**, (1982).
[98] Sun, H. et al. *Nanopillar Lasers Directly Grown on Silicon with Heterostructure Surface Passivation.* ACS Nano. **8**, (2014).
[99] Lautenschlager, P. et al. *Interband critical points of GaAs and their temperaturedependence.* Phys. Rev. B **35**, 9174-9189 (1987).
[100] Dutta, N. K., Nelson, R. J. & Barnes, P. A. *Temperature dependence of threshold and electrical characteristics of InGaAsP-InP DH lasers.* Electron Lett. **16**, 653-654 (1980).
[101] Larrue, A. et al. *Monolithic integration of III-V nanowire with photonic crystalmicrocav-*

ity for vertical light emission. Opt. Express **20**, 7758-7770 (2012).
[102] Park, H. G. et al. *A wavelength-selective photonic-crystal waveguide coupled toa nanowire light source.* Nat. Photonics **2**, 622-626 (2008).
[103] Svendsen, G. K., Weman, H. & Skaar, J. *Investigations of Bragg reflectors innanowire lasers.* J. Appl. Phys. **111**, 123102 (2012).
[104] Fang, A. W. et al. *Electrically pumped hybrid AlGaInAs-silicon evanescentlaser.* Opt. Express **14**, 9203-9210 (2006).
[105] Hertenberger, S. et al. *High composition homogeneity in In-rich InGaAsnanowire arrays on nanoimprinted SiO2/Si 111.* Appl. Phys. Lett. **101**, 043116 (2012).
[106] Chu, S. et al. *Electrically pumped waveguide lasing from ZnO nanowires.* Nat. Nanotechnol. **6**, 506-510 (2011).
[107] Mariani, G., Scofield, A. C., Hung, C. H. & Huffaker, D. L. *GaAs nanopillararraysolar cells employing in situ surface passivation.* Nat. Comm. **4**, 1497 (2013).
[108] Gao, H., Fu, A., Andrews, S. C. & Yang, P. *Cleaved-coupled nanowire lasers.* PNAS **110**, 865-869 (2013).
[109] Barrelet, C. J. *Hybrid single-nanowire photonic crystal and microresonatorstructures.* Nano Lett. **6**, 11-15 (2006).
[110] Frost, T. et al. Nano Lett. **14**, 4535 (2014).
[111] Gradecak, S., Qian, F., Li, Y., Park, H.-G. and Lieber, C. M. Appl. Phys. Lett. **87**, 173111 (2005).
[112] Gao, Q. Nano Lett. **14**, 5206 (2014).
[113] Zhang, Q. Nat. Commun. **5**, 4953 (2014).
[114] Qiu, Z. Wong, K. S., Wu, M., Lin, W. and Xu, H. Appl. Phys. Lett. **84**, 2739 (2004).
[115] Stettner, T. et al. *Coaxial GaAs-AlGaAs core-multishell nanowire lasers with epitaxial gain control.* Appl. Phys. Lett. **108**, 011108 (2016).
[116] Gao, H., Fu, A., Andrews, S. C. and Yang, P. Proc. Natl. Acad. Sci. **110**, 865 (2012).
[117] van Vugt, L. K., Zhang, B., Piccione, B., Spector, A. A. and Agarwal, R. Nano Lett. **9**, 1684 (2009).
[118] Miller, D. A. B. *Device requirements for optical interconnects to silicon chips.* Proc. IEEE **97**, 1166-1185 (2009).
[119] Martensson, T.; et al. *Epitaxial III-V nanowires on silicon.* Nano Lett. **4**, 1987-1990 (2004).
[120] Rosencher, E. and Vinter, B. *Optoelectronics.* Cambridge University Press. , 313 (2002).
[121] Strauss, U., Rühle, W. W., Köhler, K. *Auger recombination in intrinsic GaAs.* Appl. Phys. Lett. **62**, 55 (1993).
[122] Rosencher, E., Vinter, B. *Optoelectronics* Cambridge University Press , (2002).
[123] Chen, L.; Towe, E. *Coupled optoelectronic modeling and simulation of nanowire lasers.* J. Appl. Phys. **100**, 44305 (2006).
[124] Gies, C., Wiersig, J., Lorke, M., Jahnke, F. *Semiconductor model for quantum dot based microcavity lasers.* Phys. Rev. A: At., Mol., Opt. Phys. **75**, 013803 (2007).
[125] Johnson, J. C., Yan, H. Q., Yang, P. D. & Saykally, R. J. *Optical cavity effects in ZnO*

nanowire lasers and waveguides. J. Phys. Chem. B **107**, 8816-8828 (2003).
[126] Ulrich, S. M.; et al. *Photon Statistics of Semiconductor Microcavity Lasers.* Phys. Rev. Lett. **98**, 43906 (2007).
[127] Ellis, B.; et al. *Ultralow threshod electrically pumped quantum dot photonic crystal nanocavtiy laser.* Nat. Photonics **5**, 297-300 (2011).
[128] Fox, M. *Quantum Optics: An Introduction* OUP Oxford (2006).
[129] Chow, W. W.; Jahnke, F.; Gies, C. *Emission properties of nanolasers during the transition to lasing.* Light: Sci. Appl. **3**, e201 (2014).
[130] Chen, S.; et al. *Spectral dynamics of picosecond gain-switched pulses from nitride-based vertical-cavity surface-emitting lasers.* Sci. Rep. **4**, 4325 (2014).
[131] Udem, T., J. Reichert, Holzwarth, R. & Hänsch, T. W. *Accurate measurement of large optical frequency difference with a mode-locked laser.* Optics Letters **24**, 881-883 (1999).
[132] Morgenweg, J., Barmes, I. & Eikema, K. S. E. *Ramsey-comb spectroscopy with intense ultrashort laser pulses.* Nature Physics **10**, 30-33 (2014).
[133] Udem, T., Holzwarth, R. & Hänsch, T. W. *Optical frequency metrology.* Nature **416**, 233-237 (2002).
[134] Newbury, N. R. *Searching for applications with a fine-tooth comb.* Nat. Photonics **4**, 186-188 (2011).
[135] Müller, K. et al. *All optical quantum control of a spin-quantum state and ultrafast transduction into an electric current.* Scientific Reports **3**, (2013).
[136] Del'Haye, P., Schliesser, A., Arcizet, O., Wilken, T., Holzwarth, R. & Kippenberg, T. J. *Optical frequency comb generation from a monolithic microresonator.* Nature **450**, 1214-121 (2007).
[137] Kippenberg, T. J., Holzwarth, R., Diddams, S. A. *Microresontor-Based Optical Frequency Combs.* Science **332**, 555-559 (2011).
[138] Röder, R. et al. *Ultrafast Dynamics of Lasing Semiconductor Nanowires.* Nano Letters **15**, 4637-4643 (2015).
[139] Ning, C. Z. and Haken, H. *Elimination of variables in simple laser equations.* Appl. Phys. B , 55, 2, 117 ISSN 0946-2171 (1992).
[140] Haken, H. *Analogy between higher instabilities in fluids and lasers.* Phys. Lett. A A , 53, 77 (1975).
[141] Lingnau, B. *Nonlinear and Nonequilibrium Dynamics of Quantum-Dot Optoelectronic Devices.* Springer Theses, Springer International Publishing, ISBN 978-3-319-25803-4 (2015).
[142] Wilkinson, S., Lingnau, B., Korn, J., Schöll, E. and Lüdge, K. *Influence of Noise on the Signal Properties of Quantum-Dot Semiconductor Optical Amplifiers.* IEEE J. Sel. Top. Quantum Electron. , 19, 4, 1900106 (2013).
[143] Oulton, R. F. et al. *Plasmon lasers at deep subwavelength scale.* Nature **461**, 629-632 (2009).
[144] Ho, J. et al. *Low-Threshold near-Infrared GaAs-AlGaAs Core-Shell Nanowire Plasmon Laser.* ACS Photonics **2**, 165-171 (2015).
[145] Arakawa, Y. & Sakaki, H. *Multidimensional quantum well laser and temperature*

dependence of its threshold current. Appl. Phys. Lett. **40**, 939-941 (1982).
[146] Asada, M., Myamoto, Y. and Suematsu, Y. *Gain and the Threshold of Three-Dimensional Quantum-Box Lasers.* IEEE Journal of Quantum Electronics **QE-22** (1986).
[147] Qian, F. et al. *Multi-quantum-well nanowire heterostructures for wavelength-controlled lasers.* Nature Materials **7**, 701-706 (2008).
[148] Tatebayashi, J. et al. *Room-temperature lasing in a single nanowire with quantum dots.* Nature Photonics **9**, 501-505 (2015).
[149] Penn, M. *Views from Around the Globe.* http://mscorp.blob.core.windows.net/mscorpmedia/2015/01/2015DavosPollFINAL.pdf.
[150] Orwell, G. *1984*, (1949).